NASA TN D-445

TECHNICAL NOTE
D-445

INVESTIGATION OF LONGITUDINAL AND LATERAL STABILITY CHARACTERISTICS OF A SIX-PROPELLER DEFLECTED-SLIPSTREAM VTOL MODEL WITH BOUNDARY-LAYER CONTROL INCLUDING EFFECTS OF GROUND PROXIMITY

By Kalman J. Grunwald

Langley Research Center
Langley Field, Va.

NATIONAL AERONAUTICS AND SPACE ADMINISTRATION
WASHINGTON
January 1961

NATIONAL AERONAUTICS AND SPACE ADMINISTRATION

TECHNICAL NOTE D-445

INVESTIGATION OF LONGITUDINAL AND LATERAL STABILITY CHARACTERISTICS OF A SIX-PROPELLER DEFLECTED-SLIPSTREAM VTOL MODEL WITH BOUNDARY-LAYER CONTROL INCLUDING EFFECTS OF GROUND PROXIMITY

By Kalman J. Grunwald

SUMMARY

An investigation of the longitudinal and lateral stability and control and performance characteristics of a six-propeller deflected-slipstream vertical-take-off-and-landing (VTOL) model in the transition speed range was conducted in the 17-foot test section of the Langley 300-MPH 7- by 10-foot tunnel. A complete analysis of the data was not conducted. A modest amount of blowing boundary-layer control was necessary to achieve transition without wing stall.

INTRODUCTION

Although considerable research has been done on propeller-driven VTOL configurations (refs. 1 to 6), this work for the most part involved investigations of longitudinal characteristics. Relatively little lateral-stability data were available at the time the present investigation was initiated. In order to obtain comprehensive longitudinal- and lateral-stability data, a model of a six-propeller deflected-slipstream transport-type VTOL configuration was tested in the 17-foot test section of the Langley 300-MPH 7- by 10-foot tunnel. The model employed a 50-percent-chord sliding flap and a 30-percent-chord Fowler flap. Blowing boundary-layer control was used on the top surface of the fixed portion of the wing at the 40-percent-chord station.

Subsequent to the inception of the present investigation two other lateral-stability investigations on deflected-slipstream configurations have been completed (refs. 7 and 8). Because of the relatively complete analyses contained in these references, the present results are presented herein without analysis.

SYMBOLS

The force and moment coefficients used in this report are based on the dynamic pressure in the slipstream. This system is used because, when a wing is located in a propeller slipstream, large forces and moments can be produced even though the free-stream velocity decreases to zero, and in this condition coefficients based on the free-stream dynamic pressure approach infinity and therefore become meaningless. It appears appropriate, therefore, to base the coefficients on the dynamic pressure in the slipstream. The coefficients based on this dynamic pressure are indicated in the present paper by the use of the subscript s. The relations between the thrust and dynamic pressure in the slipstream have been derived in reference 2. The more familiar coefficient forms based on the free-stream dynamic pressure can be found by dividing by $\left(1 - C_{T,s}\right)$; that is, $C_L = \frac{C_{L,s}}{1 - C_{T,s}}$. The positive senses of forces, moments, and angles are indicated in figure 1. The pitching moments are presented with reference to the center of gravity located at the projection of the wing 40-percent-chord point shown in figure 2.

b wing span, 8 ft

C_L lift coefficient based on free stream, $\frac{\text{Lift}}{qS_w}$

$C_{L,s}$ lift coefficient based on slipstream, $\frac{\text{Lift}}{q_s S_w}$

$C_{l,s}$ rolling-moment coefficient, $\frac{\text{Rolling moment}}{q_s S_w b}$

$C_{m,s}$ pitching-moment coefficient, $\frac{\text{Pitching moment}}{q_s S_w c}$

$C_{n,s}$ yawing-moment coefficient, $\frac{\text{Yawing moment}}{q_s S_w b}$

$C_{p,s}$ pressure coefficient, $\frac{p - p_t}{q_s}$

$C_{T,s}$ slipstream thrust coefficient, $\frac{T}{q_s N \frac{\pi}{4} D^2}$

$C_{X,s}$ longitudinal-force coefficient, $\frac{F_X}{q_s S_w}$

$C_{Y,s}$ side-force coefficient, $\frac{\text{Side force}}{q_s S_w}$

C_μ coefficient of mass flow, $\frac{mV}{qS_w}$

c wing chord, 1 ft

c_r rear-flap chord, 0.466 ft

D propeller diameter, $1\frac{1}{2}$ ft

F resultant force, lb

F_X longitudinal force, lb

h height of center of gravity above ground (measured at $\alpha \approx 0$)

h' height of trailing edge of slotted flap above ground (measured at $\alpha \approx 0$)

i_t incidence of horizontal tail, deg

L lift, lb

M_X rolling moment, ft-lb

M_Y pitching moment, ft-lb

M_Z yawing moment, ft-lb

m mass flow, slugs/sec

N number of propellers

p local static pressure, lb/sq ft

p_t free-stream total pressure, lb/sq ft

q free-stream dynamic pressure, $\frac{1}{2}\rho V^2$, lb/sq ft

q_s slipstream dynamic pressure, $q + \frac{T}{N\frac{\pi}{4}D^2}$, lb/sq ft

S_p total propeller-disc area, 10.6 sq ft

S_w	wing area, 8 sq ft
T	total thrust, lb
V	free-stream velocity, ft/sec
x	wing-chord station measured from leading edge, in.
α	angle of attack, deg
β	angle of sideslip, deg
$\delta_{f,R}$	rear-flap (Fowler flap) deflection, deg
$\delta_{f,S}$	sliding-flap deflection, deg
ρ	mass density of air, slugs/cu ft
θ	turning angle (static tests), deg

MODEL

The primary model dimensions are presented in figure 2, and the wing-flap system is shown in figure 3. Photographs of the model and support system in the tunnel are presented as figure 4. The model wing has an NACA 4415 airfoil section (fig. 3). The wing-chord line was parallel to the fuselage center line and on the propeller thrust axis. The flap system consisted of a 50-percent-chord sliding flap and a 30-percent-chord Fowler flap.

The radius of the sliding portion of the sliding flap was only 15 percent of the wing chord (fig. 3). With this relatively small radius, it was believed that some auxiliary aid would be needed to achieve high slipstream-deflection angles. For this reason, the wing was also equipped with a blowing boundary-layer-control slot on the top surface of the fixed portion of the wing at the 40-percent-chord station of the sliding flap as shown in figure 3. Air for this boundary-layer-control slot was supplied to the model through flexible hoses.

As can be seen from figure 3, the position of the leading edge of the rear flap is considerably higher with respect to the trailing edge of the sliding flap than would normally be considered good practice with a Fowler flap. This position was used because in the early static tests with the flap leading edge 0.015c below the sliding-flap chord

line, it was found that the air sheet from the blowing boundary-layer-control slot completely missed the Fowler flap when it was set at large deflections. This resulted in very low effectiveness of the Fowler flap with regard to slipstream deflection at zero forward speeds. To avoid this condition, the flap was repositioned as shown in figure 3 to ensure that the blowing air would attach to the Fowler flap at all deflections used.

The combinations of flap deflections used in the investigation and the system used to designate the flap deflections as used on the figures and text are as follow:

Sliding-flap deflection, $\delta_{f,S}$, deg	Rear-flap deflection, $\delta_{f,R}$, deg	Designation: $\delta_{f,S}/\delta_{f,R}$
0	0	0/0
0	40	0/40
20	20	20/20
20	40	20/40
40	20	40/20
40	40	40/40
50	40	50/40
60	40	60/40
70	40	70/40

The model was constructed with a steel frame for load support and a wood covering for the desired contours. The propellers had three blades and were made of wood and glass fabric. A variable-frequency electric motor was used to drive the propellers. The motor was mounted in the fuselage and was connected to the propellers through shafting and gearing. The rotational speed of the propellers was determined by observing a stroboscopic-type indicator to which was fed the output frequency of small alternators connected to the motor shaft. The rotational direction of the propeller is shown in figure 2.

An internally mounted six-component strain-gage balance was used to measure the model forces and moments. The mass flow through the nozzle which supplies the boundary-layer-control air was measured by means of a standard sharp-edge orifice flowmeter. The total pressure of the boundary-layer-control air (which was used to calculate the exhaust velocity assuming isentropic expansion) was determined from a spanwise survey of the exhaust total-pressure distribution using a small total-pressure tube flattened to the thickness of the blowing slot.

Predrilled holes were used to set the flap deflections and the tail incidence. A T-tail was used to keep the tail out of erratic changes in downwash that reference 5 indicates would be experienced with a low horizontal tail.

The pressure distribution around the chord of the wing and flap system was measured at one spanwise station as shown in figure 2. The chordwise locations of the pressure orifices are tabulated in table I.

TESTS AND CORRECTIONS

The testing was conducted in the 17-foot test section of the Langley 300-MPH 7- by 10-foot tunnel which is described in the appendix in reference 5. A propeller blade angle of 10° was used for thrust coefficients above 0.5; for thrust coefficients below 0.5, a blade angle of 20° was employed. Propeller rotational speed of 6,000 rpm was used in conjunction with the blade angle of 10°, and 4,000 rpm with the blade angle of 20°. The total thrust produced by the propellers was determined at each thrust coefficient at zero angle of attack with the flaps retracted. The thrust of the propellers was obtained by taking the difference between the measured longitudinal force with the propellers operating and the longitudinal force with the propellers off.

The test procedure for obtaining data for steady, level flight consisted of setting the propeller rotational speed with the model at zero angle of attack and then increasing the tunnel speed until zero longitudinal force was reached. These tunnel and propeller speeds were held constant as the data were taken through the angle-of-attack range. Subsequent tests were also made at tunnel dynamic pressures above and below the tunnel speed for steady, level flight at zero angle of attack in order to provide data for the variation of the aerodynamic characteristics with thrust coefficient.

The dynamic pressure of the slipstream varied from approximately 6 to 9 lb/sq ft. A free-stream dynamic pressure of 10 lb/sq ft was used for propeller-off and propeller-windmilling tests.

The Reynolds number of the flow in the slipstream based on the wing-chord length of 1 foot varied from 0.45×10^6 to 0.55×10^6.

Corrections to free-stream velocity because of blockage and slipstream contraction were estimated and considered to be negligible. The jet-boundary corrections applied were estimated for a square test section by a method similar to that employed in reference 9. These corrections depend on the circulation about the wing; therefore, it was necessary to subtract the direct thrust contribution to lift before

applying the corrections. The following relations were used:

$$\alpha = \alpha_{measured} + 0.24C_{L,1}$$

$$C_{X,s} = (C_{X,s})_{measured} - 0.0042(C_{L,1})^2(1 - C_{T,s})$$

where $C_{L,1}$ is the increment of lift coefficient that is approximately proportional to circulation and is obtained by subtracting the direct-thrust contribution as follows:

$$C_{L,1} = \frac{C_{L,s} - C_{T,s}\frac{S_p}{S_w}\frac{F}{T}\sin(\theta + \alpha)}{1 - C_{T,s}}$$

where θ and F/T are the turning angle and thrust recovery factor at zero forward speed.

PRESENTATION OF RESULTS

The results of the investigation are presented in the following order:

DISCUSSION

The data for the present investigation are presented without analysis because references 7 and 8, which were published subsequent to the inception of this investigation, contain relatively complete analyses of lateral-stability data for similar configurations. However, the following general observations concerning the results of the present investigation are made:

Without blowing boundary-layer control, the radius of the sliding flap was too small, as was expected, and only moderate turning angles could be achieved (fig. 5). Also, the flow separated from the sliding flap in transition (without boundary-layer control) and steady-level flight ($C_{X,s} = 0$) could not be achieved without stalling (figs. 17 to 19).

Only a modest amount of blowing was needed, however, to achieve very good turning angles and thrust recovery factors (fig. 5). Also, the same modest amount of blowing was sufficient to maintain attached flow throughout the transition in steady, level flight (figs. 17 to 19).

The presence of the ground, however, caused flow separation from the flaps (figs. 28 to 31) which the blowing boundary-layer control was not able to prevent. One attempt to reduce these ground effects by doubling the mass-flow coefficient produced only a very small increase in the lift in the ground-effect region.

Langley Research Center,
National Aeronautics and Space Administration,
Langley Field, Va., May 25, 1960.

REFERENCES

1. Kuhn, Richard E., and Hayes, William C., Jr.: Wind-Tunnel Investigation of Effect of Propeller Slipstreams on Aerodynamic Characteristics of a Wing Equipped With a 50-Percent-Chord Sliding Flap and a 30-Percent-Chord Slotted Flap. NACA TN 3918, 1957.

2. Newsom, William A., Jr.: Effect of Propeller Location and Flap Deflection on the Aerodynamic Characteristics of a Wing-Propeller Combination for Angles of Attack From 0° to 80°. NACA TN 3917, 1957.

3. Kuhn, Richard E., and Draper, John W.: Investigation of Effectiveness of Large-Chord Slotted Flaps in Deflecting Propeller Slipstreams Downward for Vertical Take-Off and Low-Speed Flight. NACA TN 3364, 1955.

4. Kuhn, Richard E., and Draper, John W.: An Investigation of a Wing-Propeller Configuration Employing Large-Chord Plain Flaps and Large-Diameter Propellers for Low-Speed Flight and Vertical Take-Off. NACA TN 3307, 1954.

5. Kuhn, Richard E., and Hayes, William C., Jr.: Wind-Tunnel Investigation of Longitudinal Aerodynamic Characteristics of Three Propeller-Driven VTOL Configurations in the Transition Speed Range, Including Effects of Ground Proximity. NASA TN D-55, 1960.

6. Kuhn, Richard E., and Grunwald, Kalman J.: Longitudinal Aerodynamic Characteristics of a Four-Propeller Deflected Slipstream VTOL Model Including the Effects of Ground Proximity. NASA TN D-248, 1960.

7. Kuhn, Richard E., and Grunwald, Kalman J.: Lateral Stability and Control Characteristics of a Four-Propeller Deflected-Slipstream VTOL Model Including the Effects of Ground Proximity. NASA TN D-444, 1961.

8. James, Harry A., Wingrove, Rodney, C., Holzhauser, Curt A., and Drinkwater, Fred J., III.: Wind-Tunnel and Piloted Flight Simulator Investigation of a Deflected-Slipstream VTOL Airplane, the Ryan VZ-3RY. NASA TN D-89, 1959.

9. Gillis, Clarence L., Polhamus, Edward C., and Gray, Joseph L., Jr.: Charts for Determining Jet-Boundary Corrections for Complete Models in 7- by 10-Foot Closed Rectangular Wind Tunnels. NACA WR L-123, 1945. (Formerly NACA ARR L5G31.)

TABLE I.- CHORDWISE LOCATION OF PRESSURE ORIFICES ON WING

[Distance measured from leading edge of wing. Spanwise location is 19.5 in. from the center line of the fuselage on the left wing as shown in figure 2]

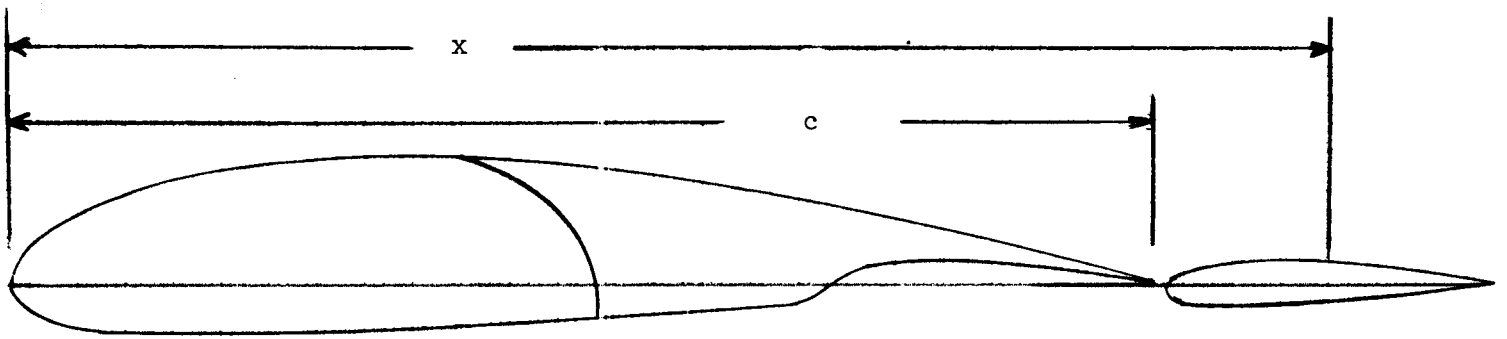

(a) Upper surface of wing

Length, x, in.	0	0.75	2.00	3.50	5.16	7.19	9.19	11.19	12.0	12.38	13.13	14.13	15.00
$\frac{x}{c}$	0	0.063	0.167	0.292	0.430	0.599	0.766	0.932	1.000	1.030	1.090	1.178	1.250

(b) Lower surface of wing

Length, x, in.	0	0.81	1.94	3.38	5.44	6.94	8.19	9.07	11.07	12.00	12.63	13.06	14.06	15.06
$\frac{x}{c}$	0	0.068	0.162	0.282	0.453	0.578	0.683	0.756	0.923	1.000	1.052	1.088	1.172	1.255

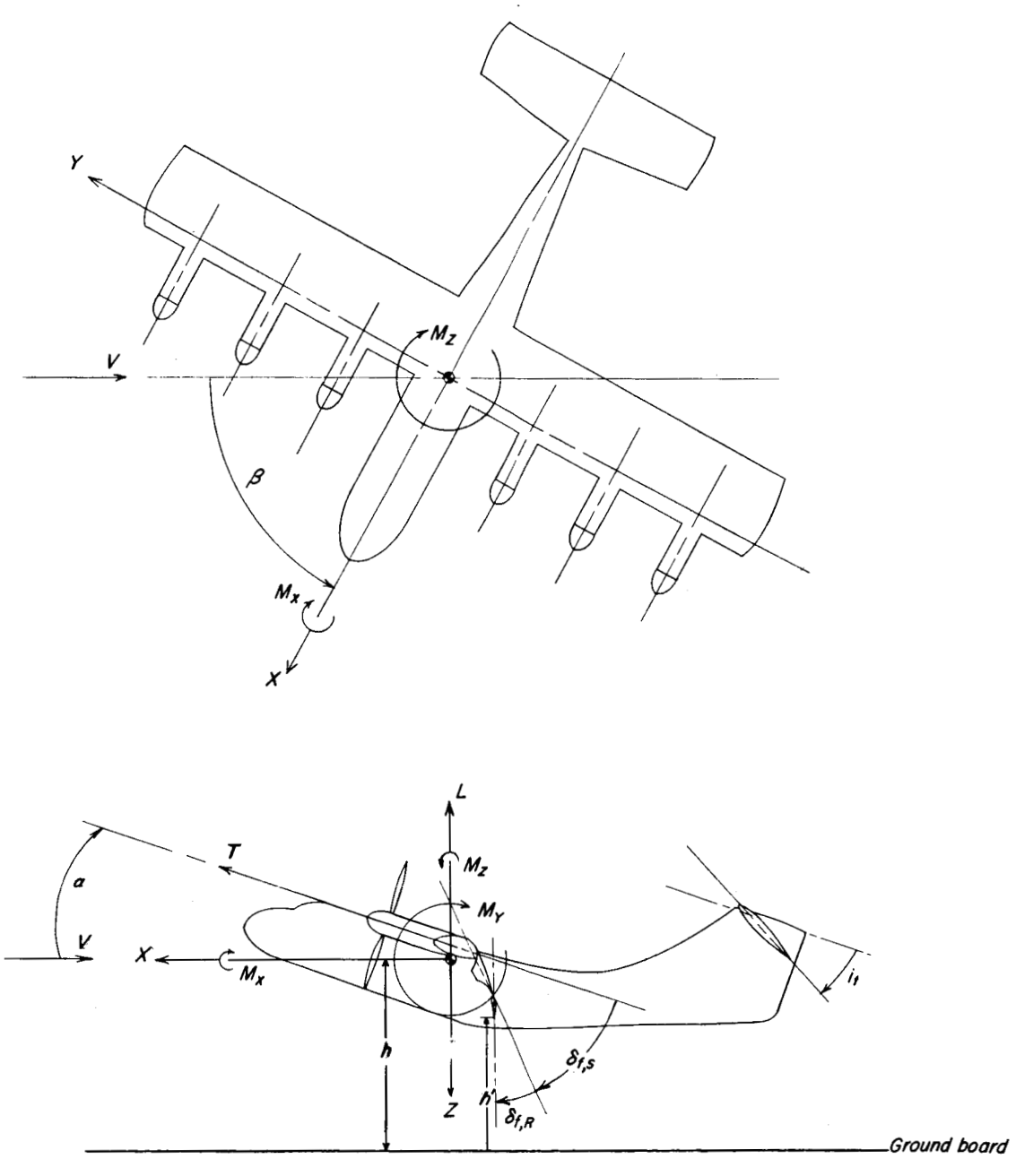

Figure 1.- Axis-system drawing showing positive sense of forces, moments, and angles.

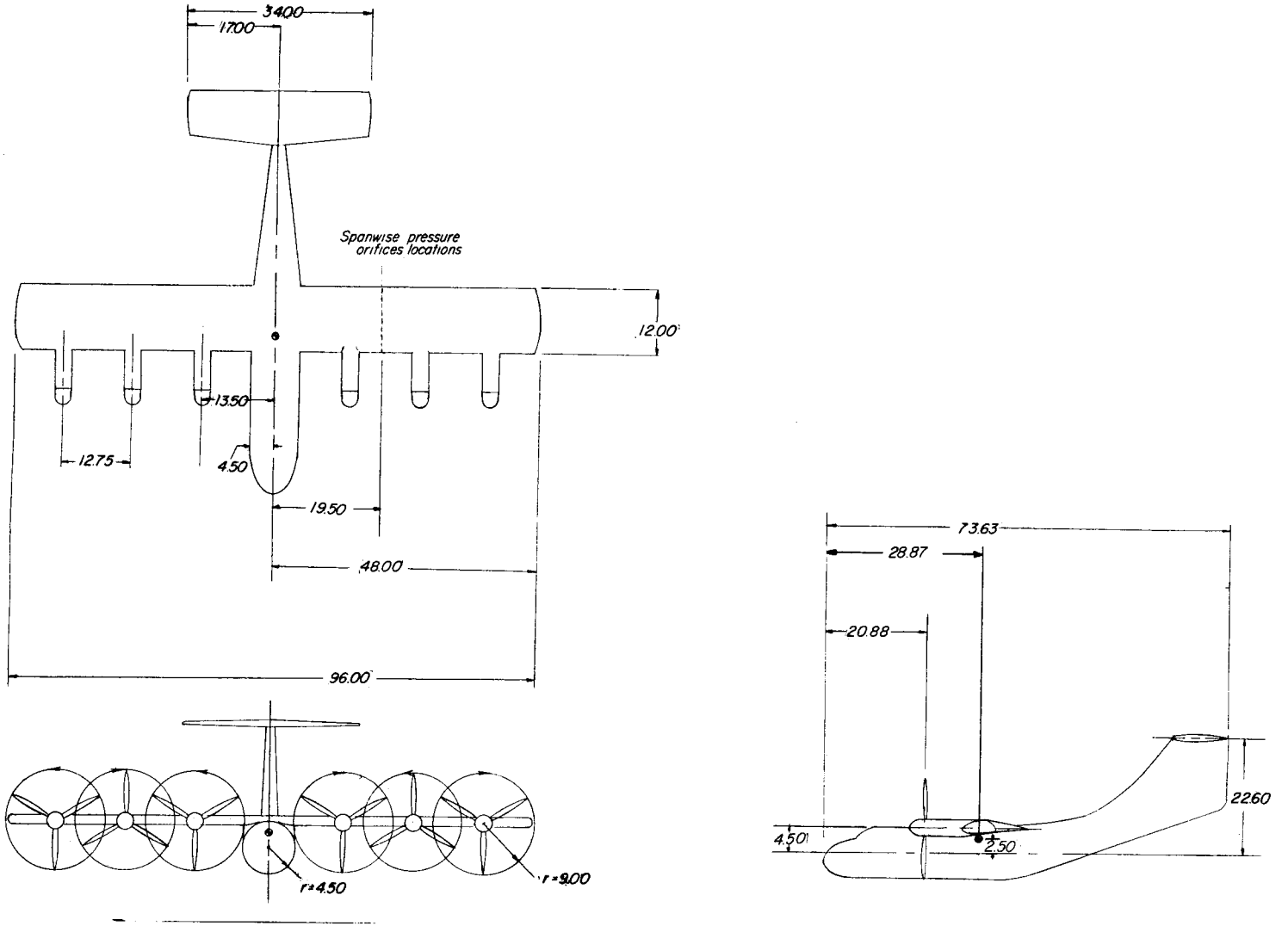

Figure 2.- Three-view drawing. All dimensions in inches.

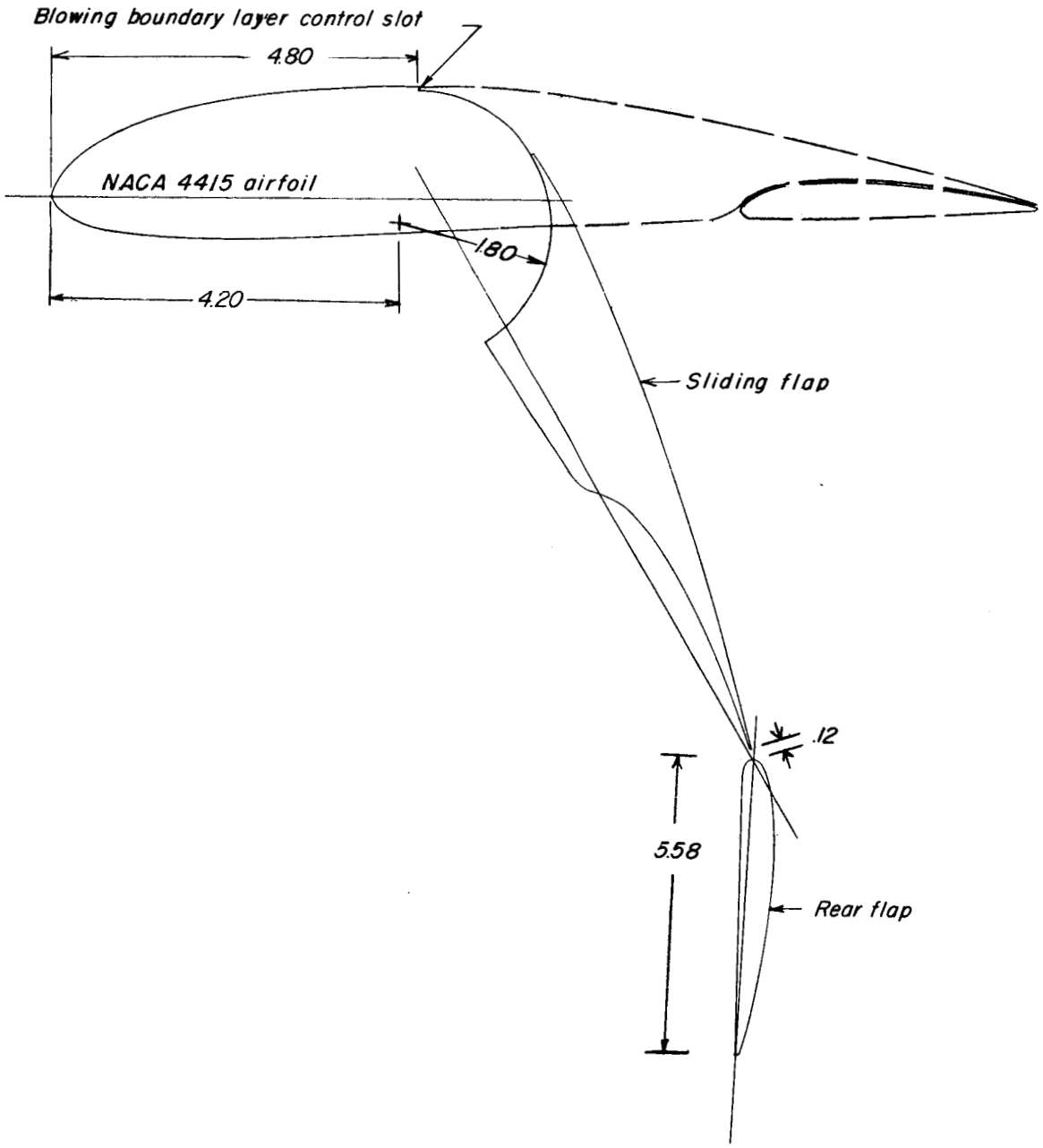

Figure 3.- Drawing of wing-flap system.

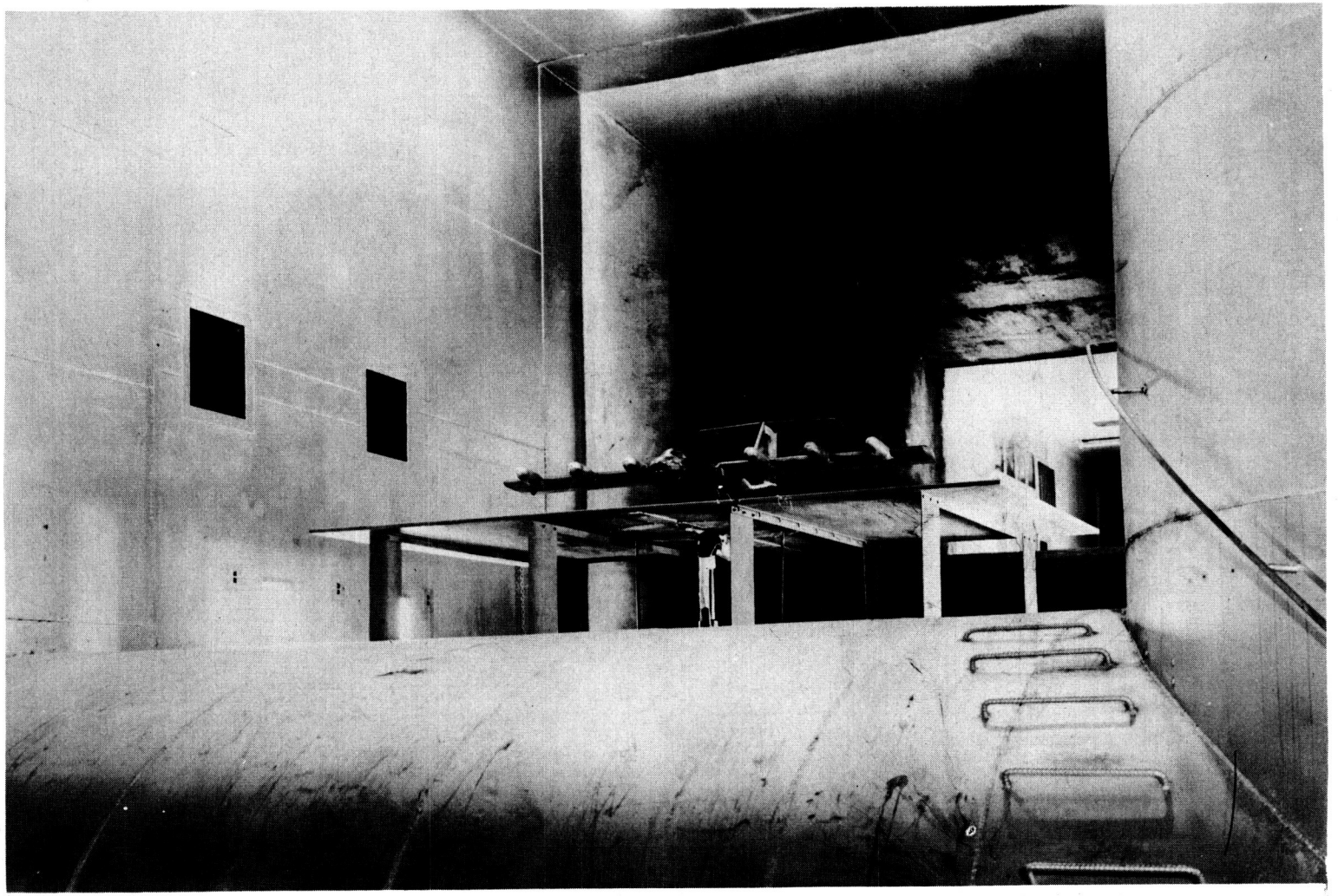

L-58-1536

Figure 4.- Photographs of model mounted in tunnel over the ground board.

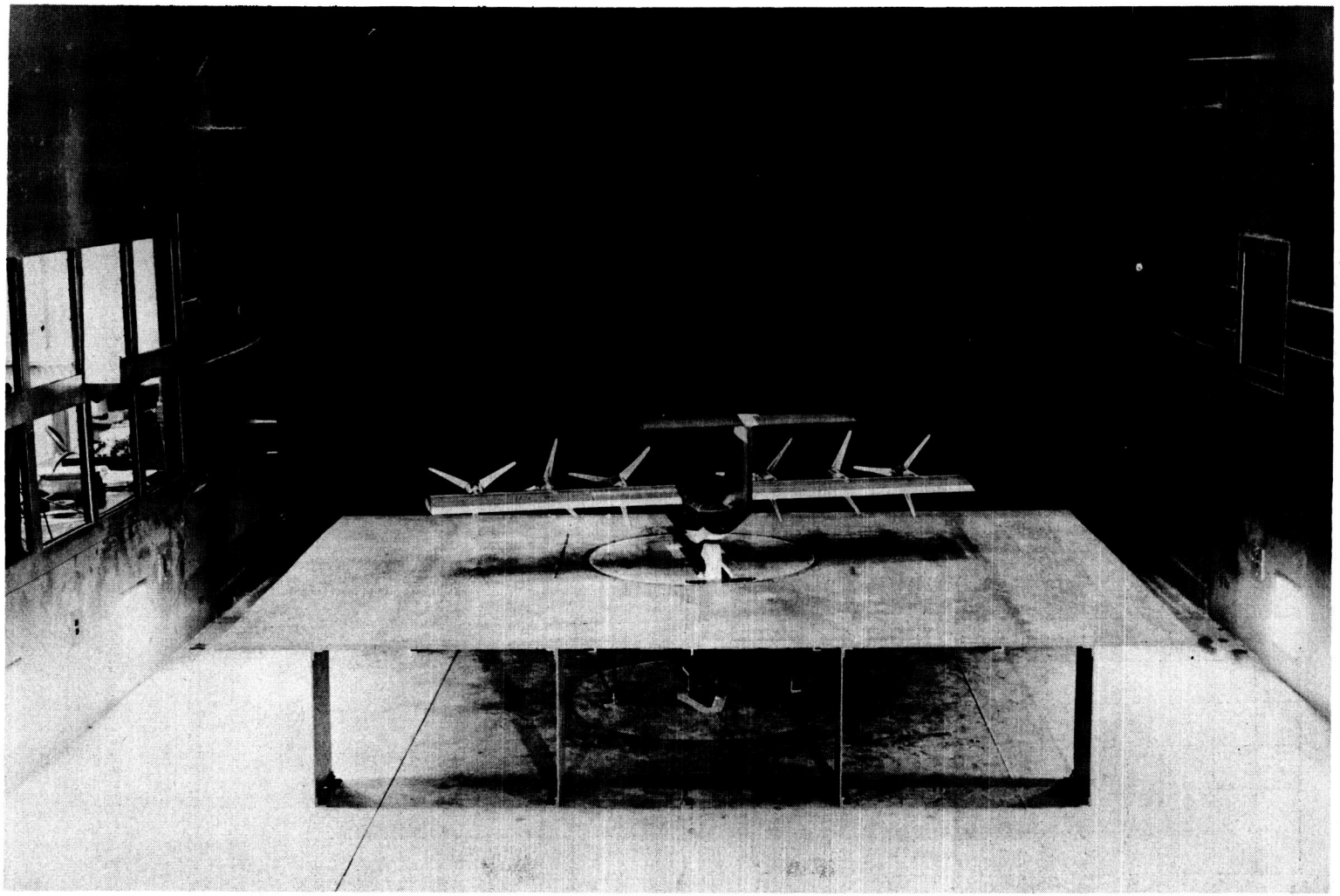

Figure 4.- Concluded. L-58-1537

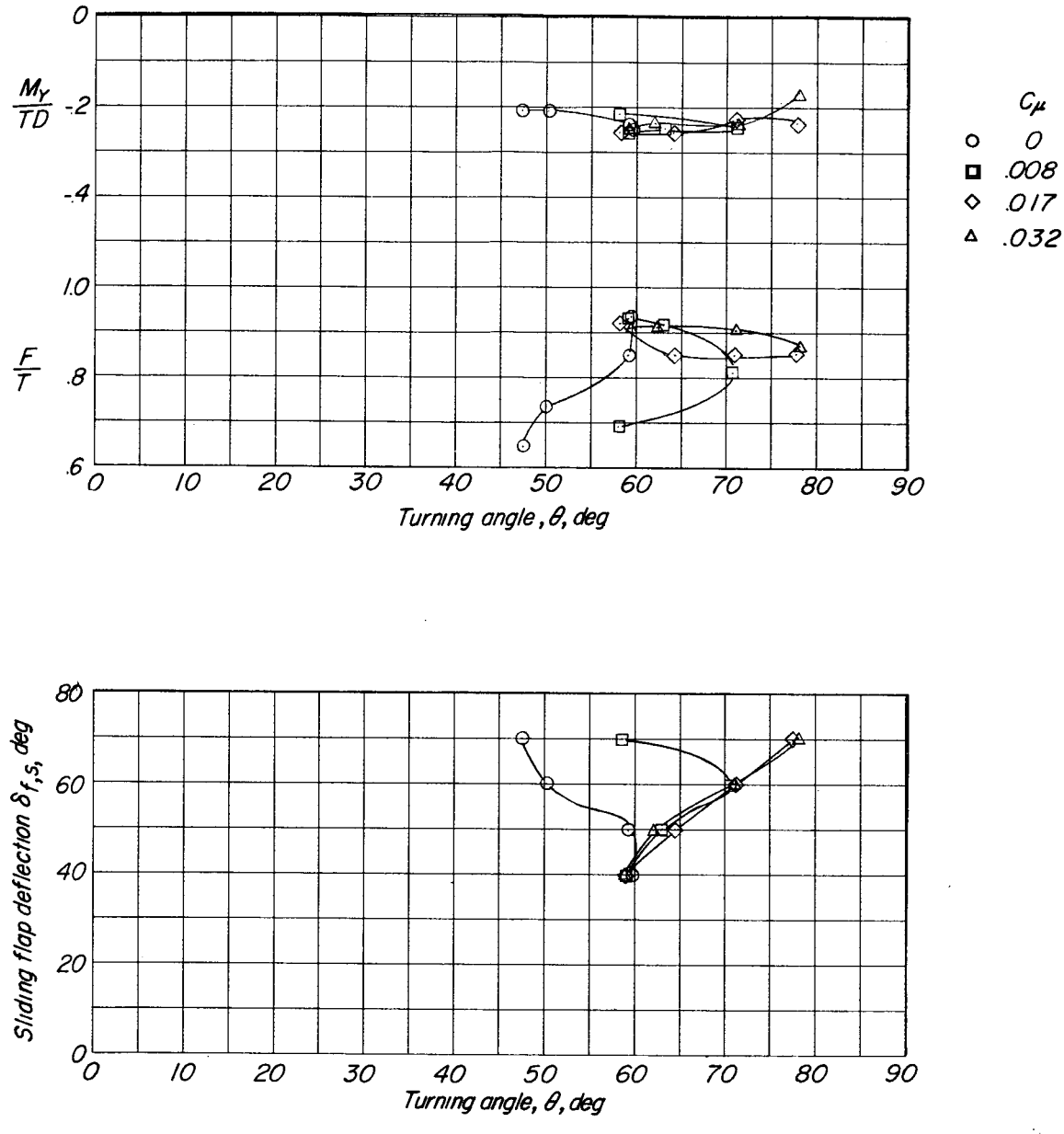

(a) Nondimensional static pitching moment, thrust recovery factor, and sliding-flap deflection.

Figure 5.- Slipstream-deflection characteristics for static conditions.

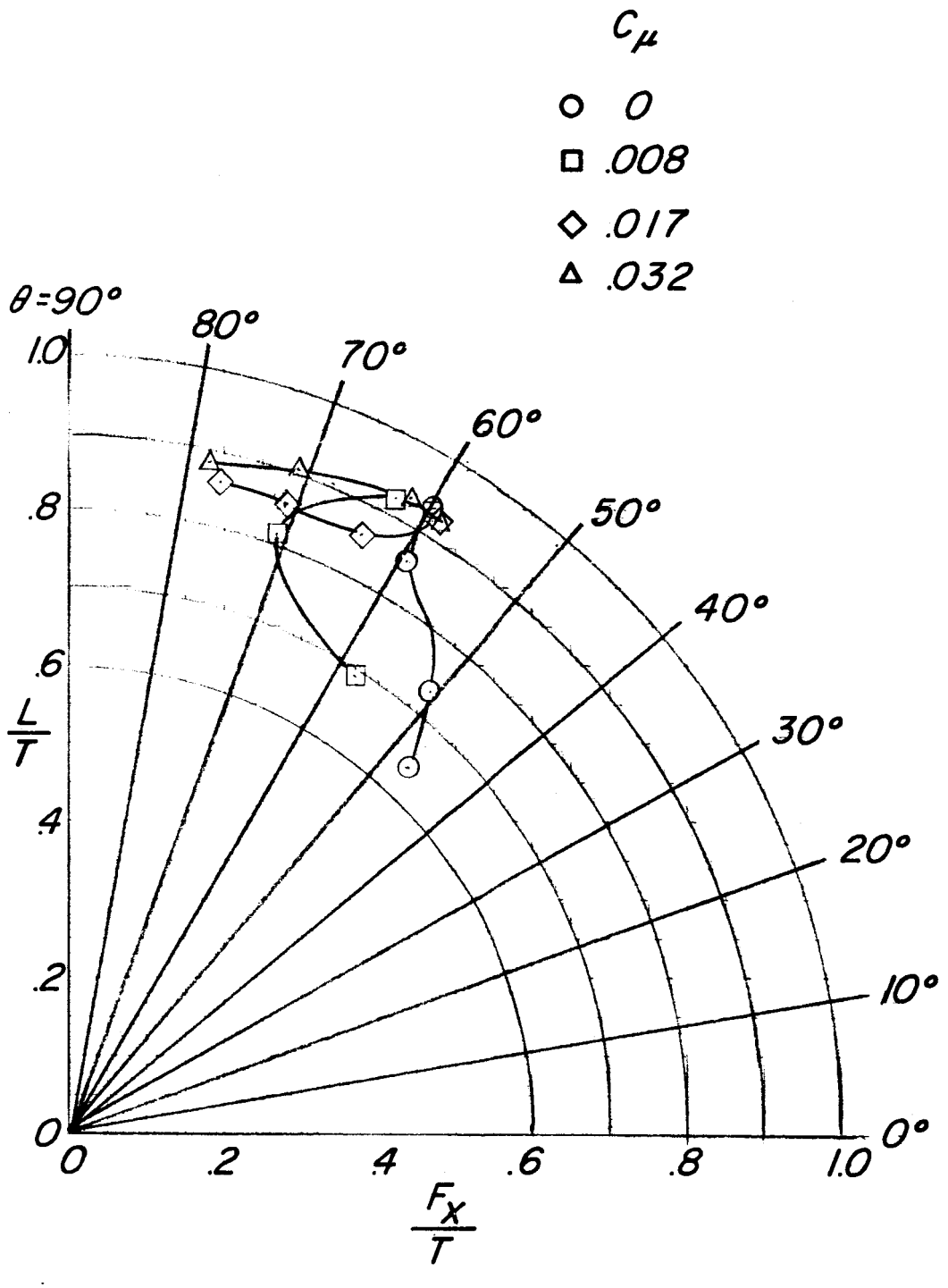

(b) Turning-effectiveness summary.

Figure 5.- Concluded.

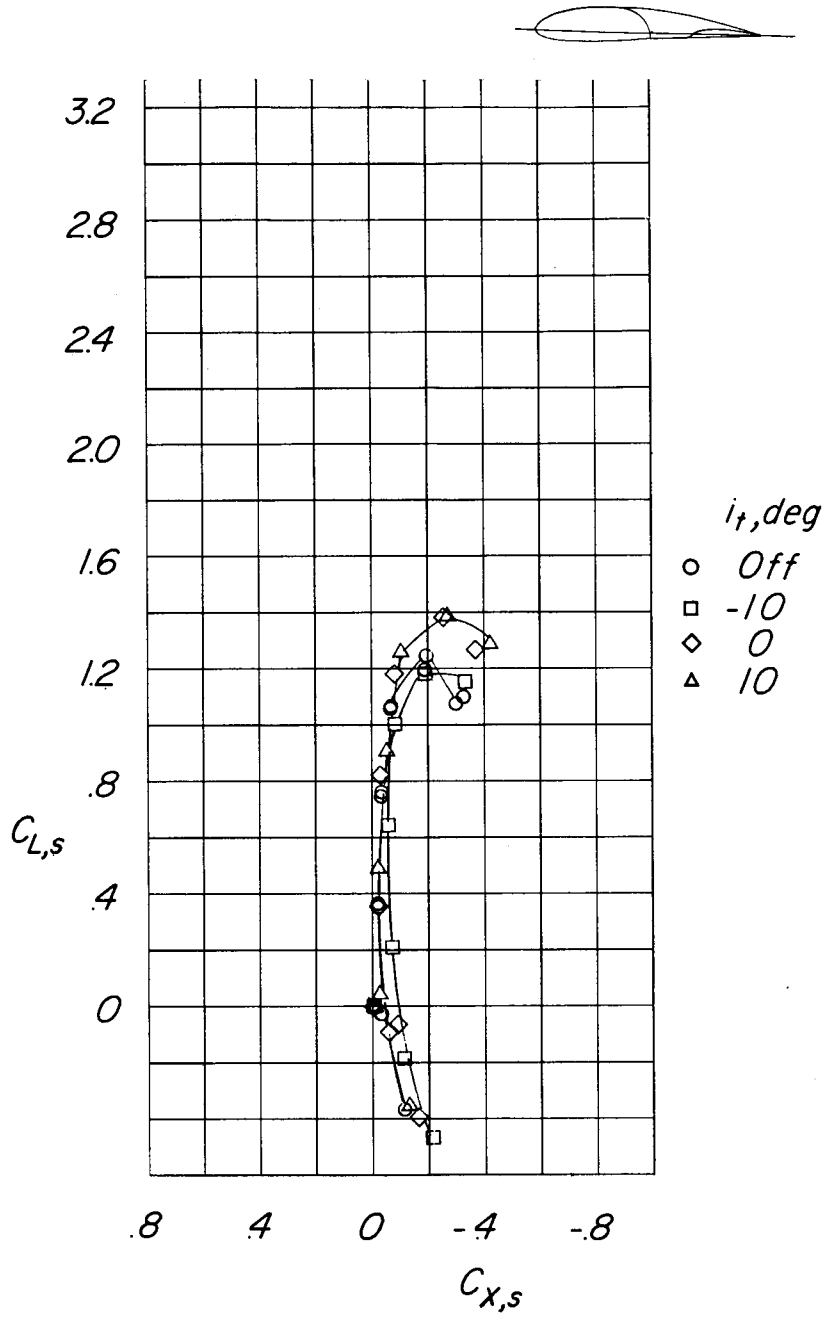

(a) Variation of longitudinal-force coefficient with lift coefficient.

Figure 6.- Effect of stabilizer incidence on longitudinal aerodynamic characteristics out of the region of ground effect. $\delta_{f,S}/\delta_{f,R} = 0/0$; $C_{T,s} = 0$ (propellers off); $C_{\mu} = 0$.

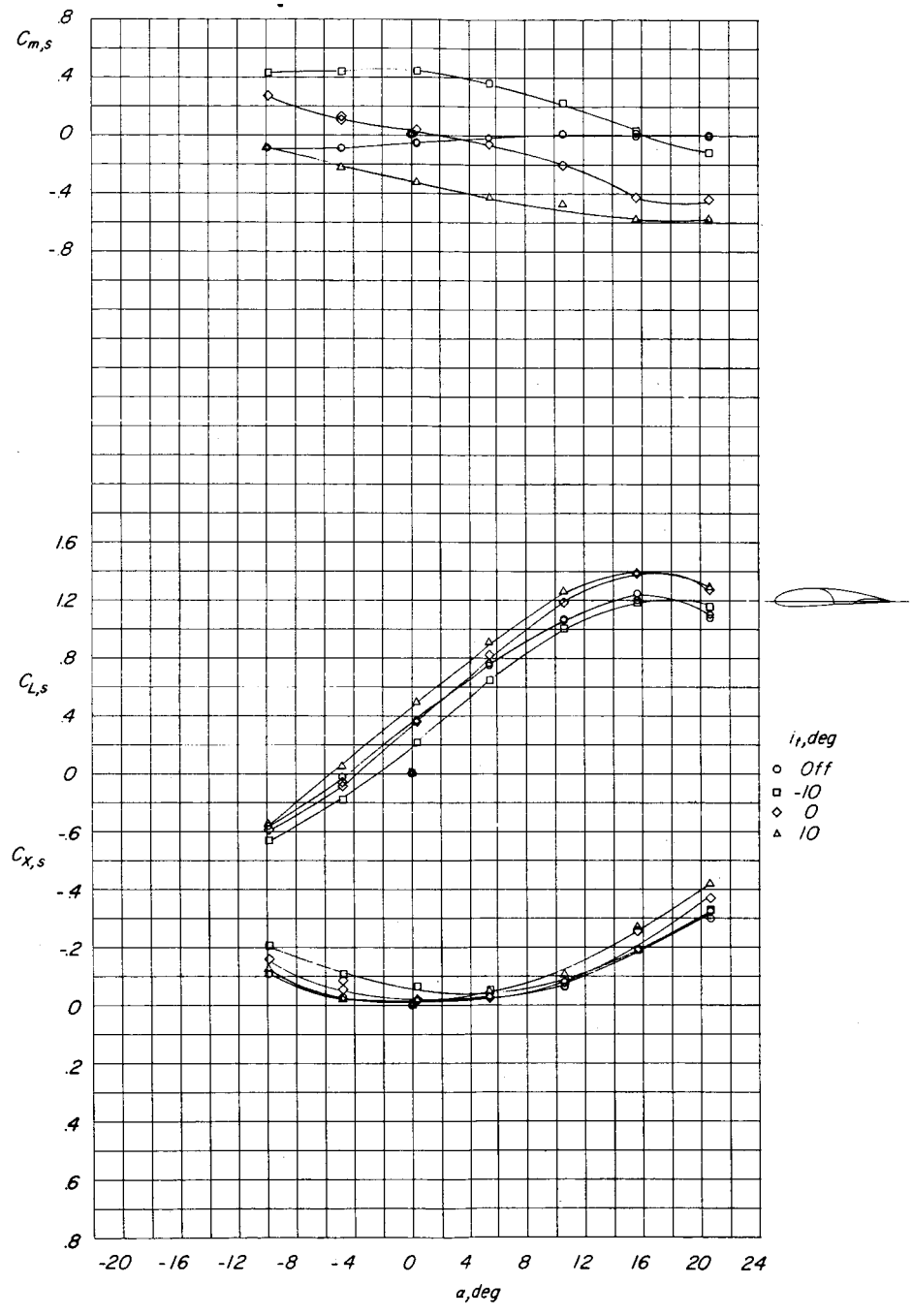

(b) Variation of pitching-moment, lift, and longitudinal-force coefficients with angle of attack.

Figure 6.- Concluded.

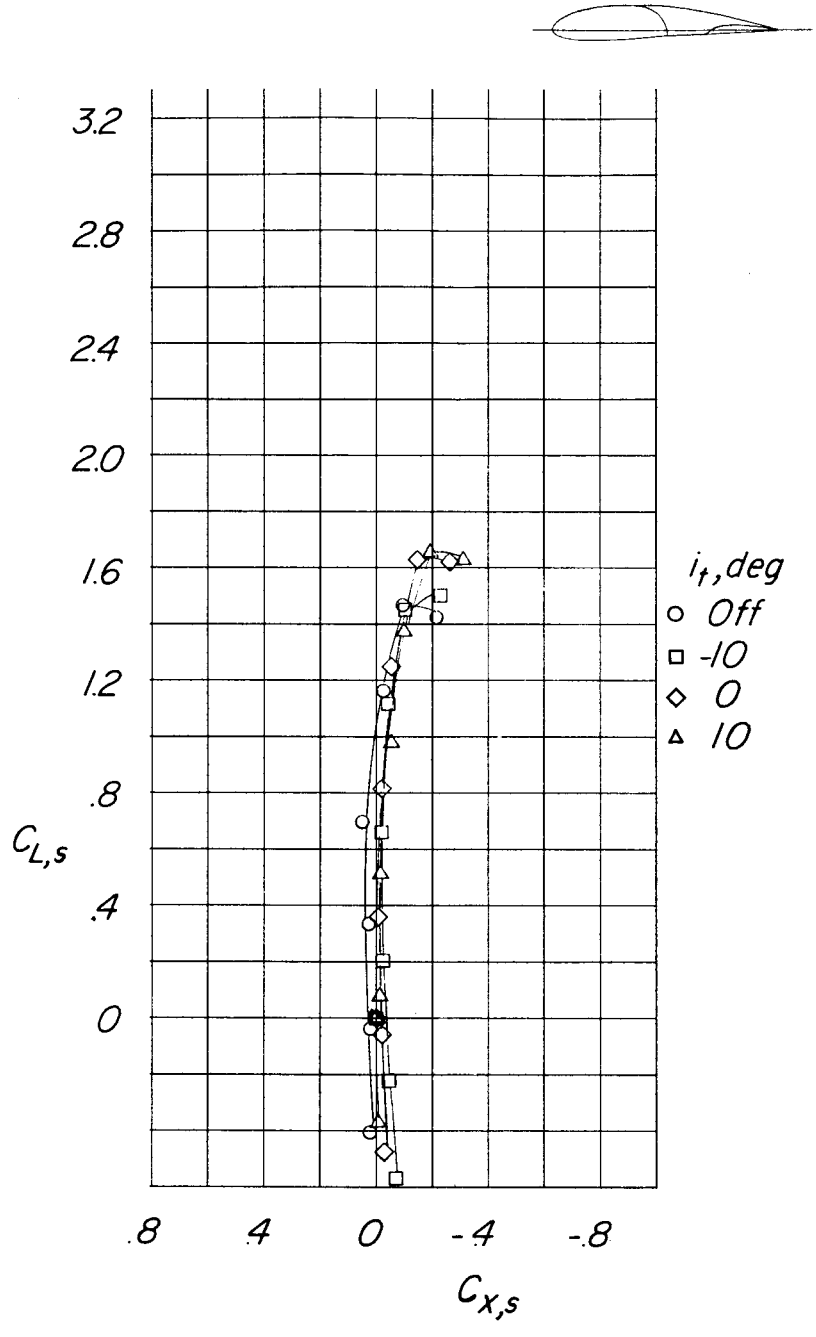

(a) Variation of longitudinal-force coefficient with lift coefficient.

Figure 7.- Effect of stabilizer incidence on longitudinal aerodynamic characteristics out of the region of ground effect. $\delta_{f,S}/\delta_{f,R} = 0/0$; $C_{T,s} = 0$ (propellers on, 4,200 rpm); $C_{\mu} = 0$.

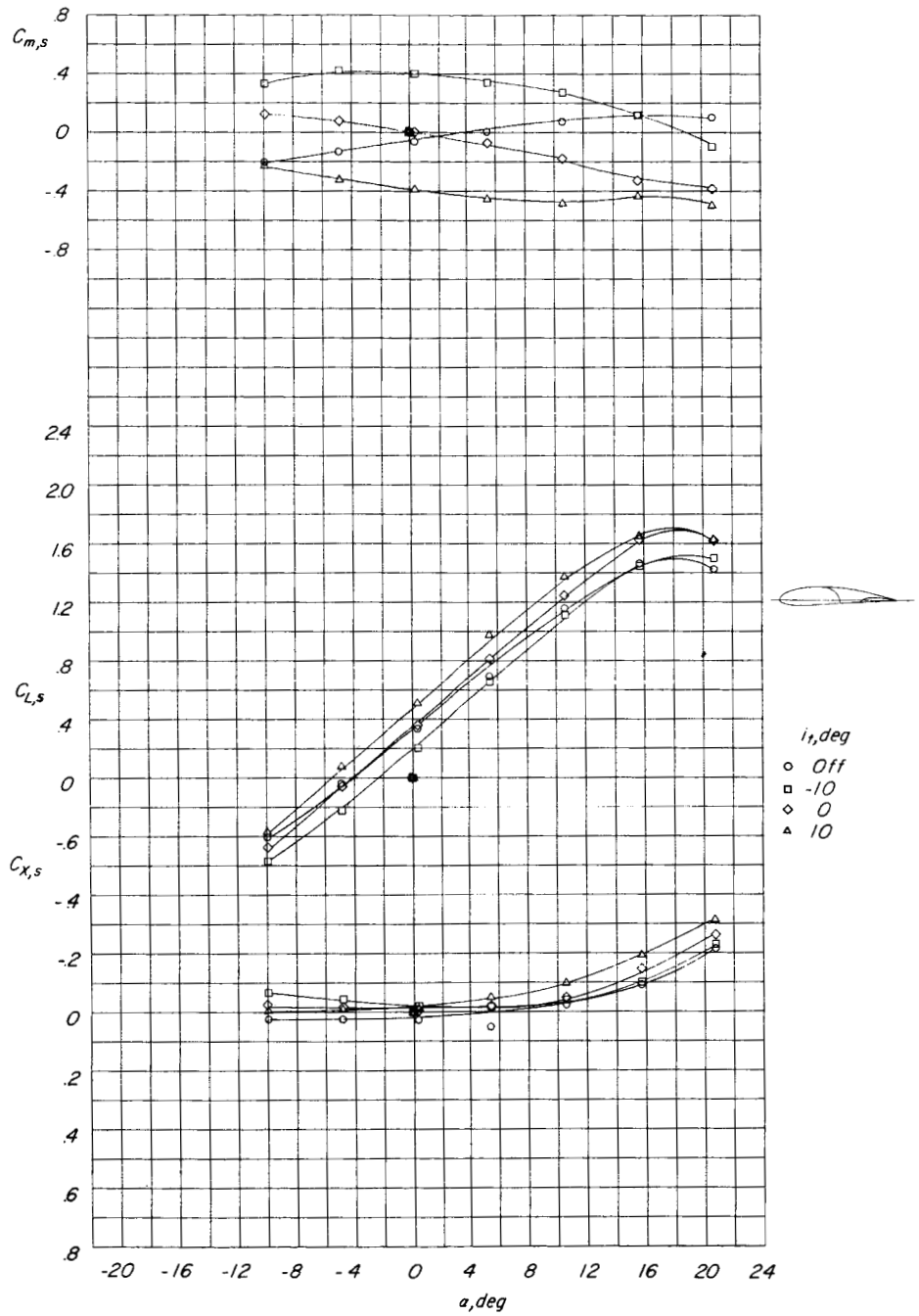

(b) Variation of pitching-moment, lift, and longitudinal-force coefficients with angle of attack.

Figure 7.- Concluded.

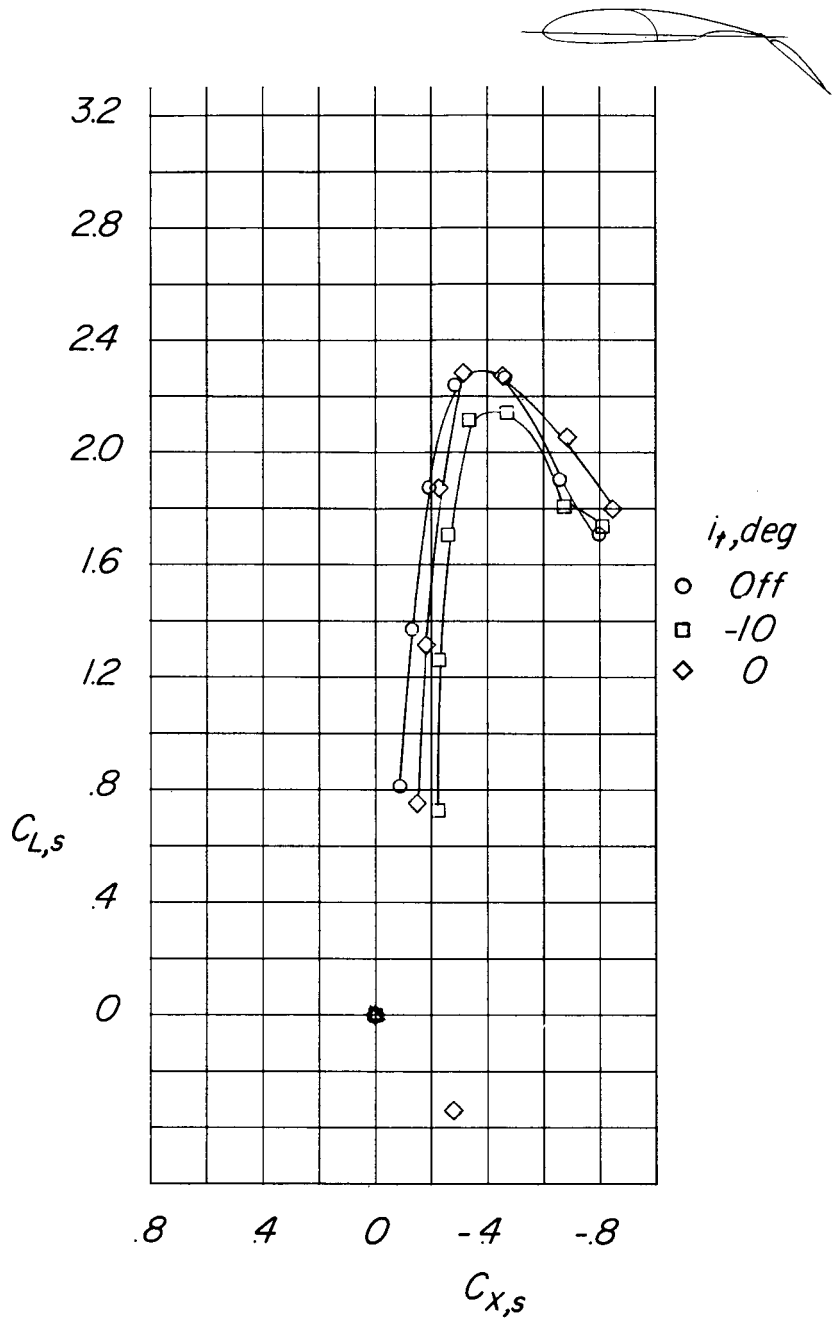

(a) Variation of longitudinal-force coefficient with lift coefficient.

Figure 8.- Effect of stabilizer incidence on longitudinal aerodynamic characteristics out of the region of ground effect. $\delta_{f,S}/\delta_{F,R}$ = 0/40; $C_{T,s}$ = 0 (propellers off); C_{μ} = 0.

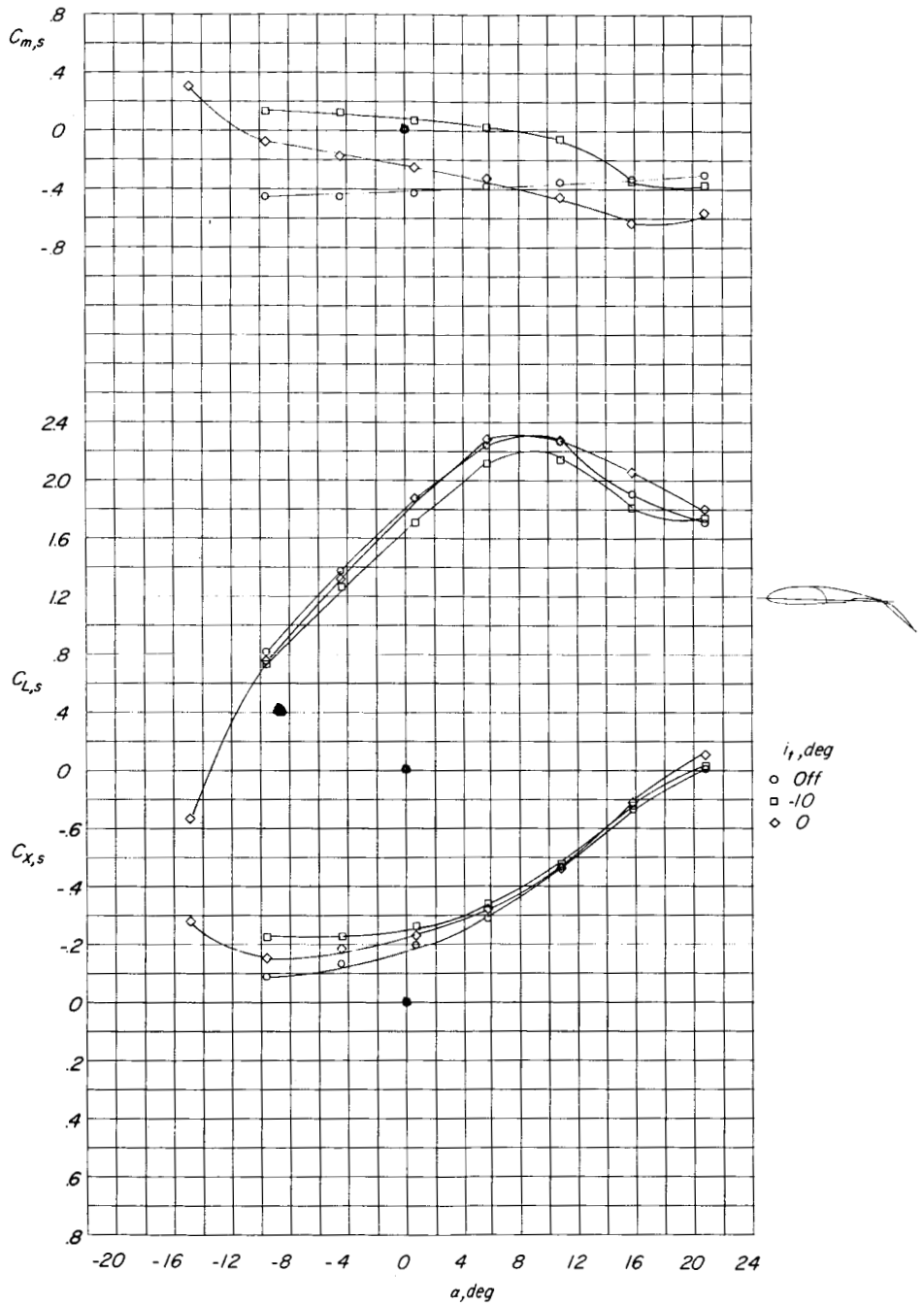

(b) Variation of pitching-moment, lift, and longitudinal-force coefficients with angle of attack.

Figure 8.- Concluded.

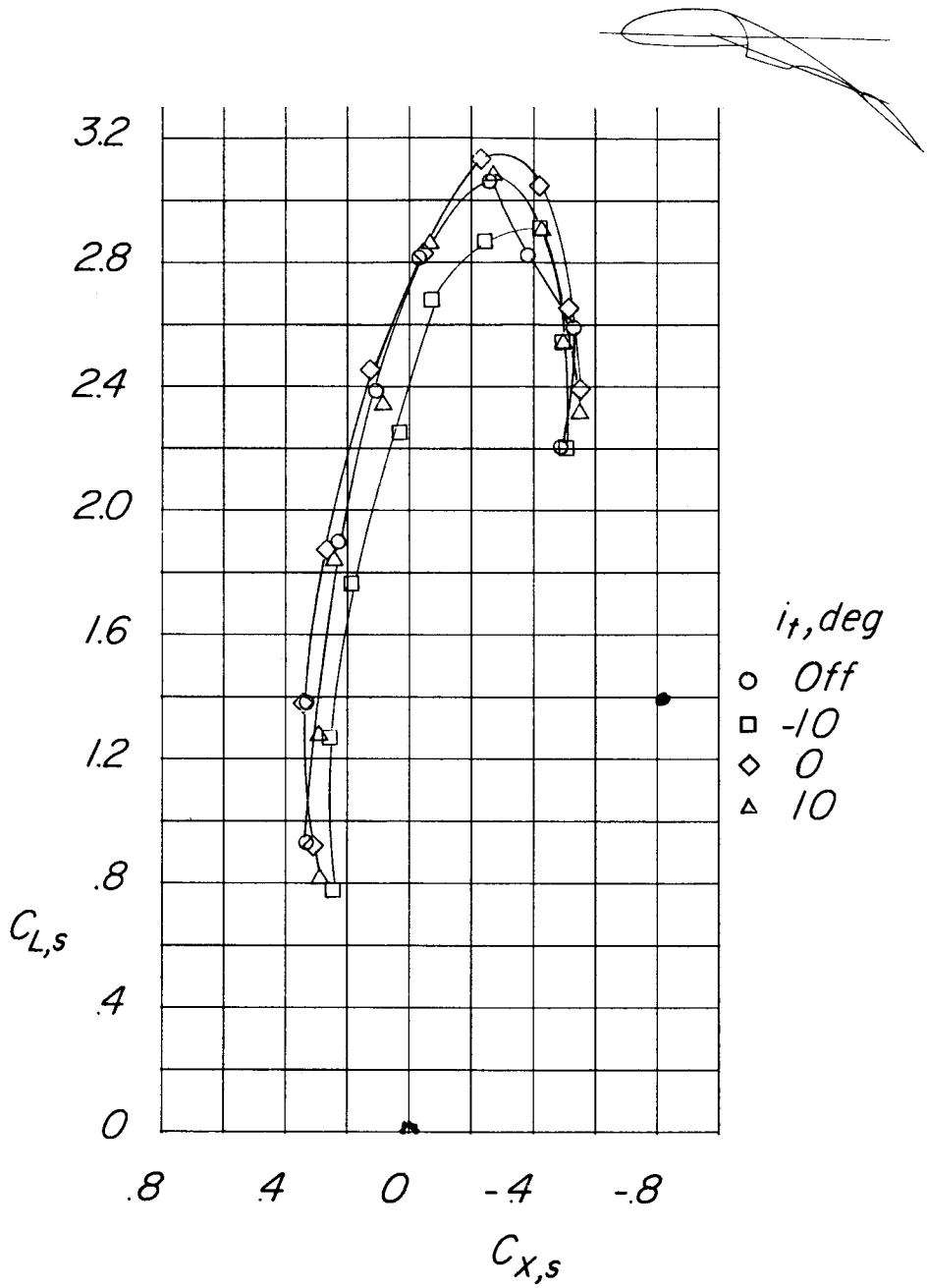

(a) Variation of longitudinal-force coefficient with lift coefficient.

Figure 9.- Effect of stabilizer incidence on longitudinal aerodynamic characteristics out of the region of ground effect. $\delta_{f,S}/\delta_{f,R}$ = 20/20; $C_{T,s}$ = 0.324; C_{μ} = 0.032.

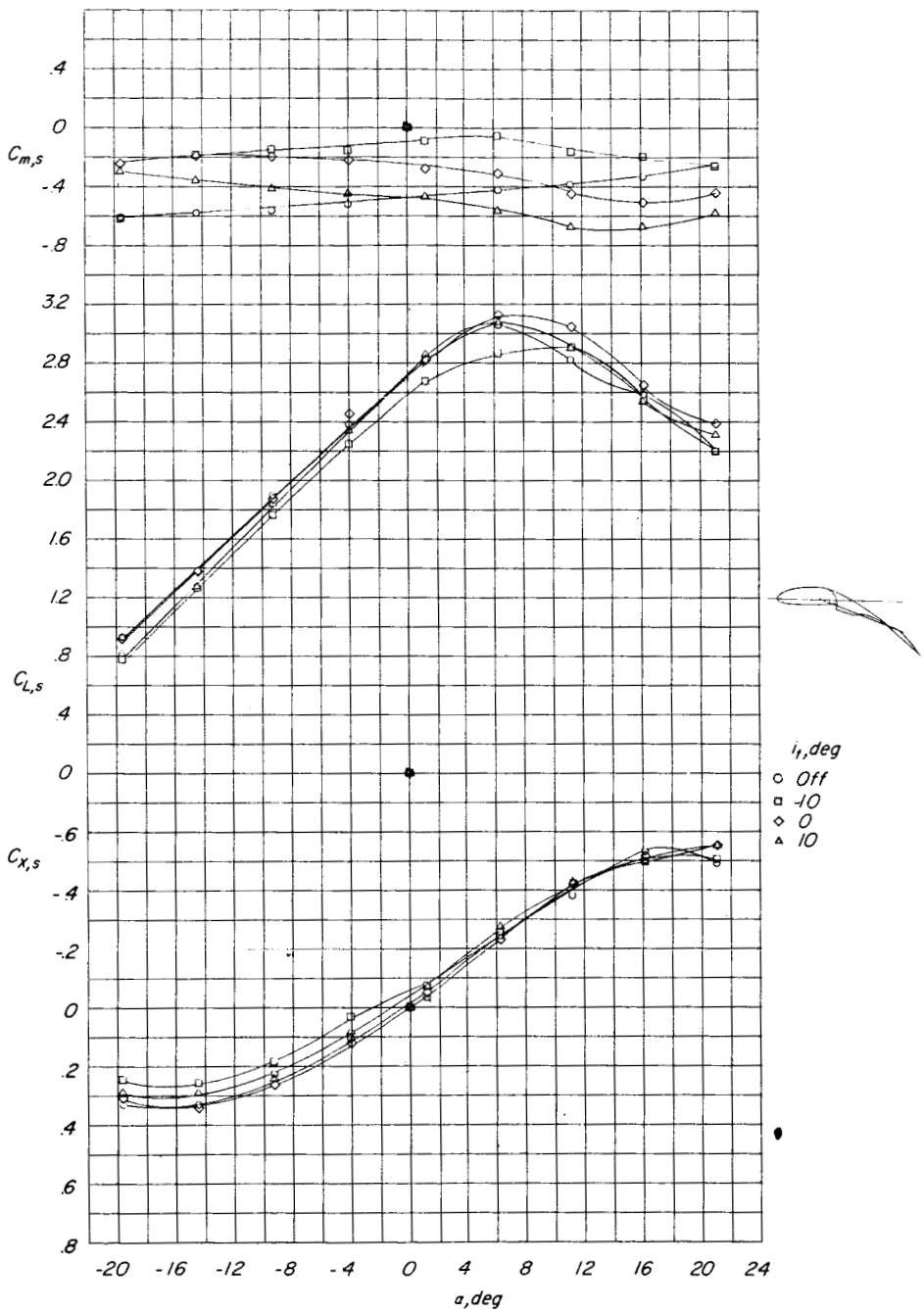

(b) Variation of pitching-moment, lift, and longitudinal-force coefficients with angle of attack.

Figure 9.- Concluded.

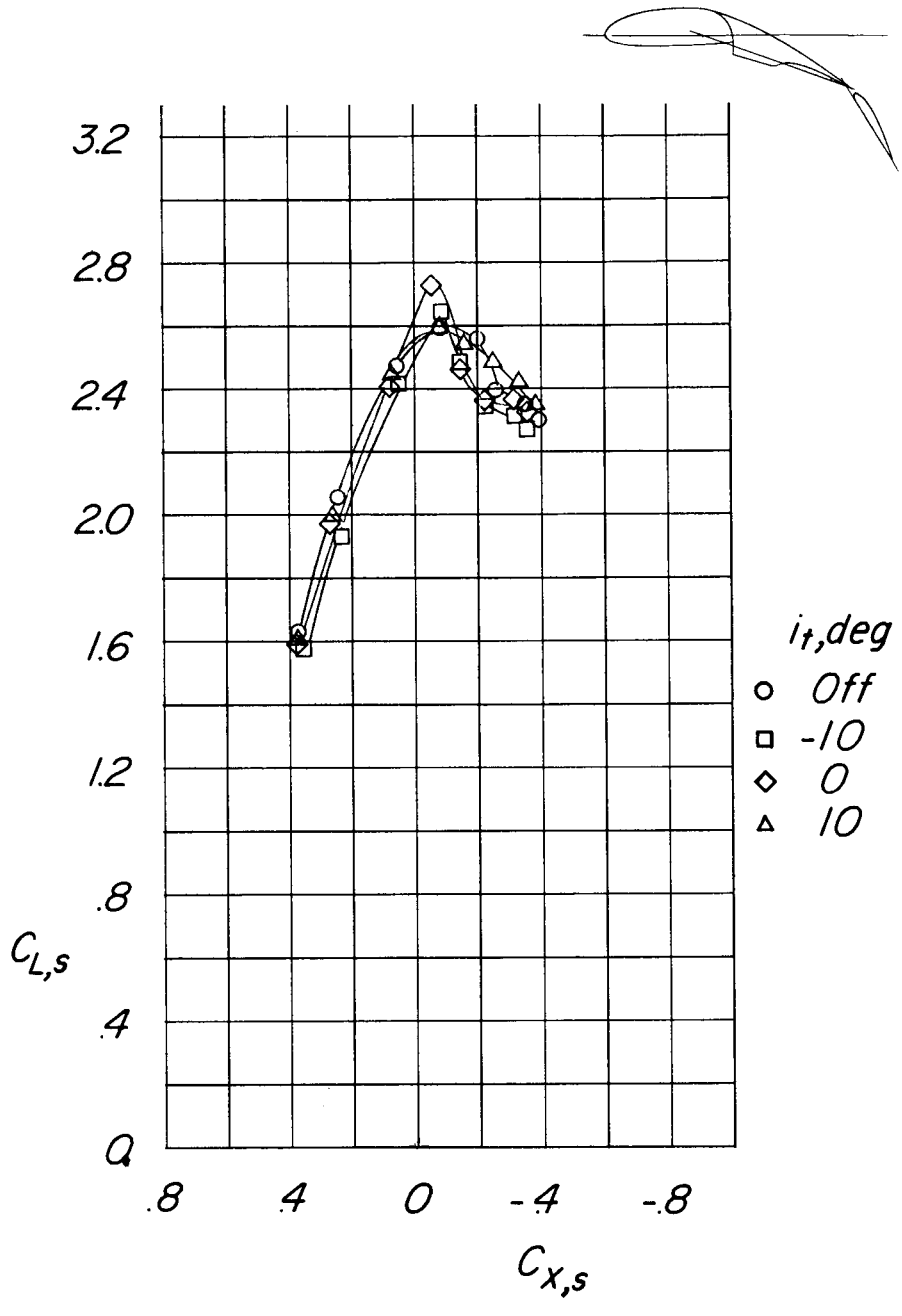

(a) Variation of longitudinal-force coefficient with lift coefficient.

Figure 10.- Effect of stabilizer incidence on longitudinal aerodynamic characteristics out of the region of ground effect. $\delta_{f,S}/\delta_{f,R}$ = 20/40; $C_{T,s}$ = 0.510; C_{μ} = 0.

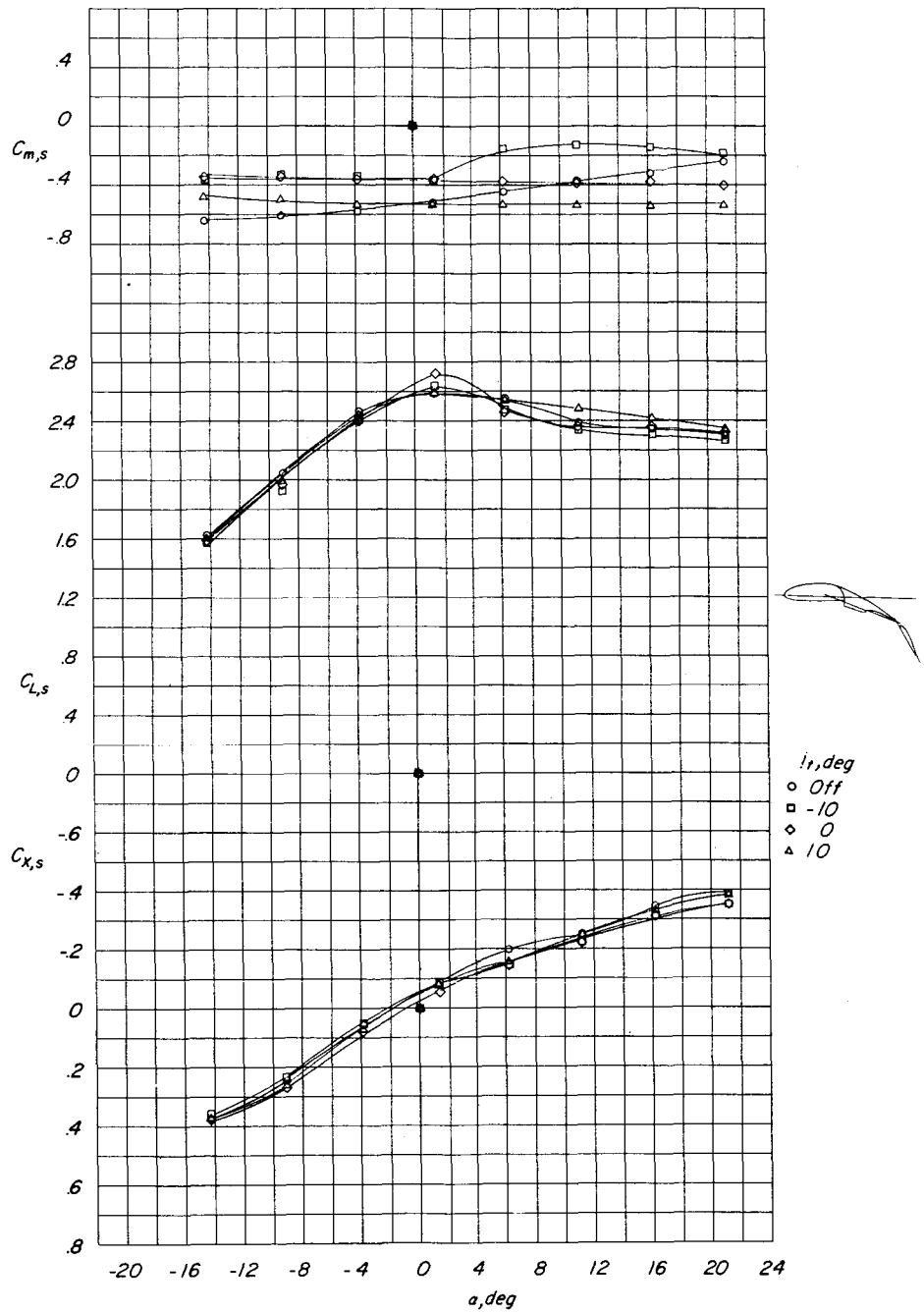

(b) Variation of pitching-moment, lift, and longitudinal-force coefficients with angle of attack.

Figure 10.- Concluded.

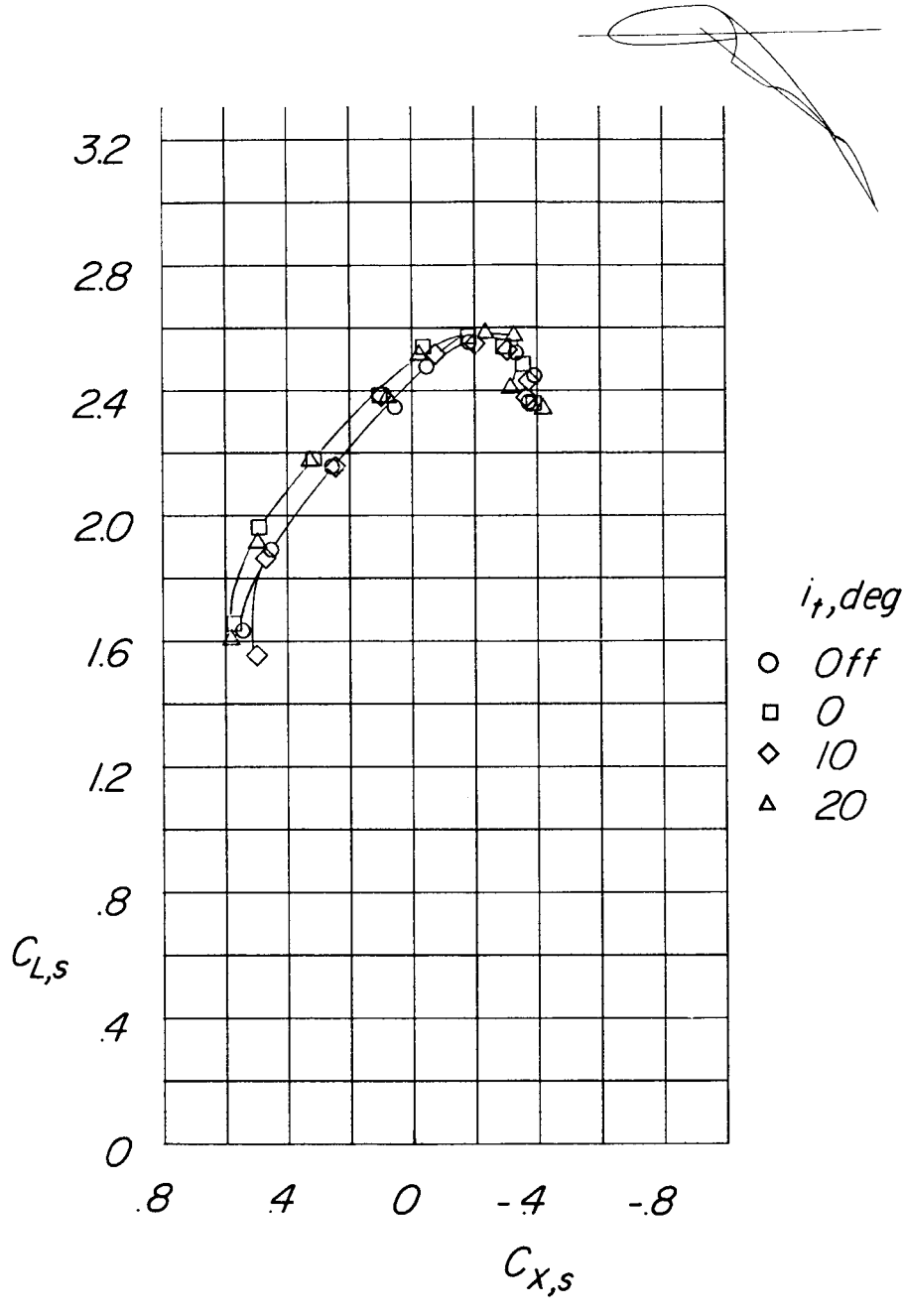

(a) Variation of longitudinal-force coefficient with lift coefficient.

Figure 11.- Effect of stabilizer incidence on longitudinal aerodynamic characteristics out of the region of ground effect. $\delta_{f,S}/\delta_{f,R}$ = 40/20; $C_{T,s}$ = 0.750; C_{μ} = 0.032.

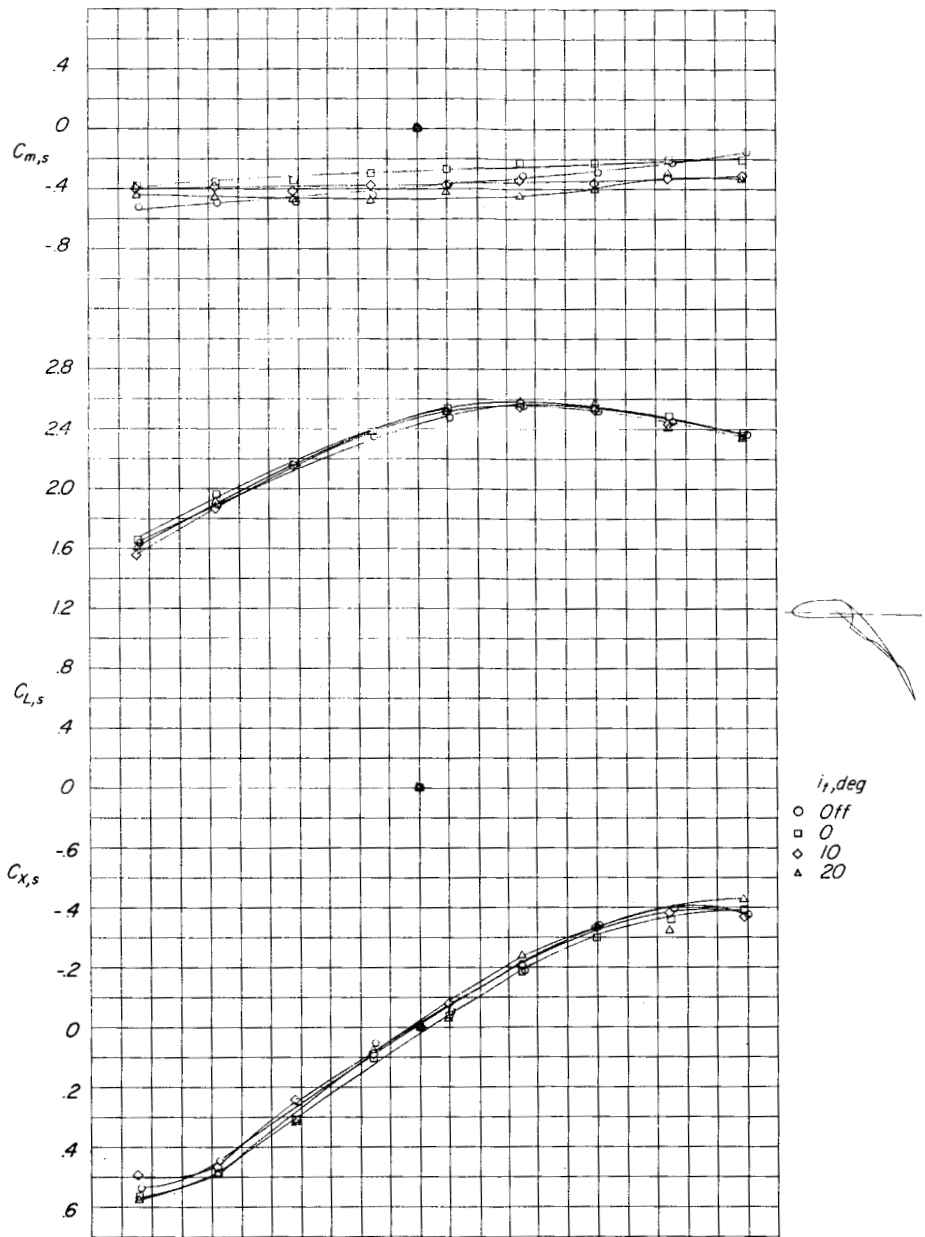

(b) Variation of pitching-moment, lift, and longitudinal-force coefficients with angle of attack.

Figure 11.- Concluded.

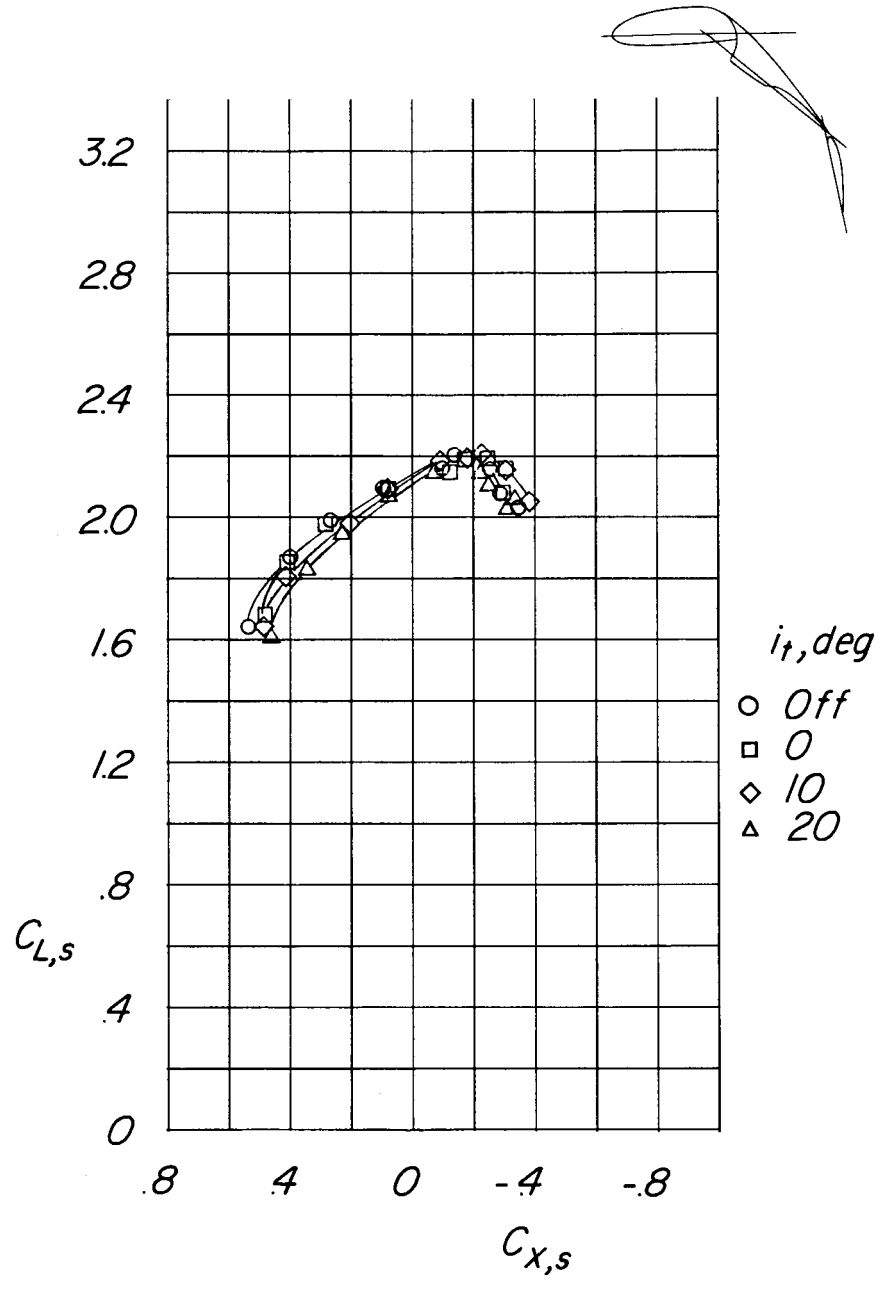

(a) Variation of longitudinal-force coefficient with lift coefficient.

Figure 12.- Effect of stabilizer incidence on longitudinal aerodynamic characteristics out of the region of ground effect. $\delta_{f,S}/\delta_{f,R}$ = 40/40; $C_{T,s}$ = 0.864; C_{μ} = 0.032.

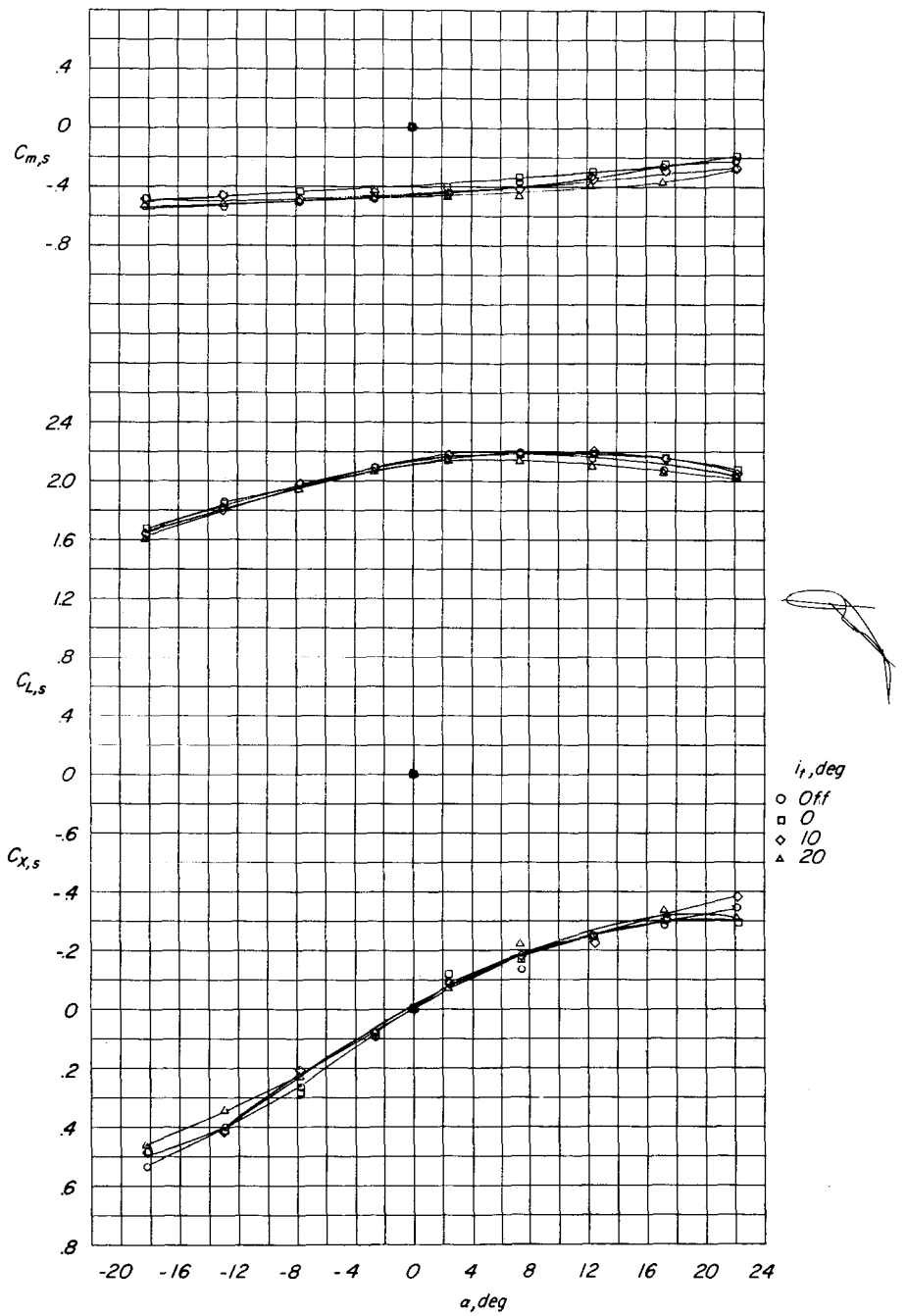

(b) Variation of pitching-moment, lift, and longitudinal-force coefficients with angle of attack.

Figure 12.- Concluded.

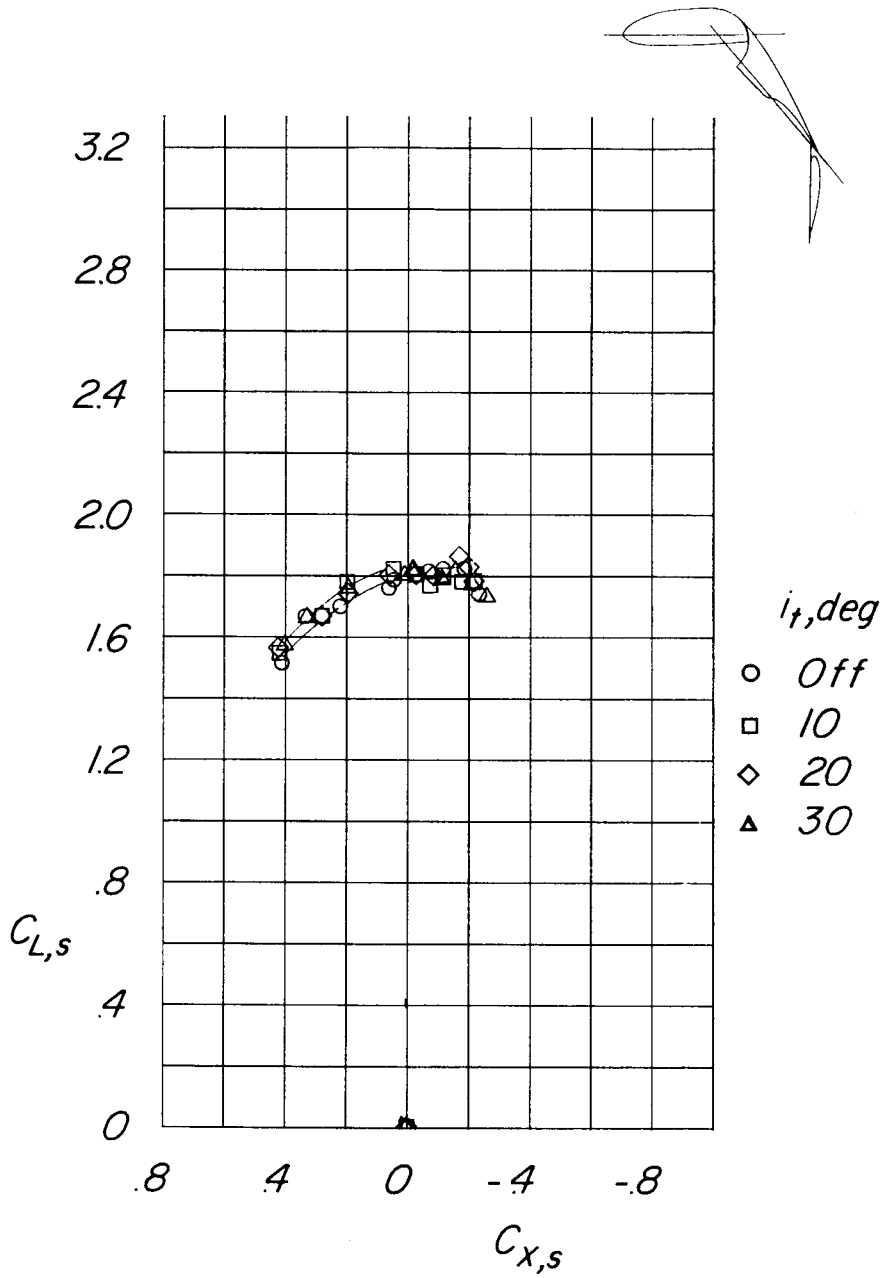

(a) Variation of longitudinal-force coefficient with lift coefficient.

Figure 13.- Effect of stabilizer incidence on longitudinal aerodynamic characteristics out of the region of ground effect. $\delta_{f,S}/\delta_{f,R}$ = 50/40; $C_{T,s}$ = 0.920; C_μ = 0.032.

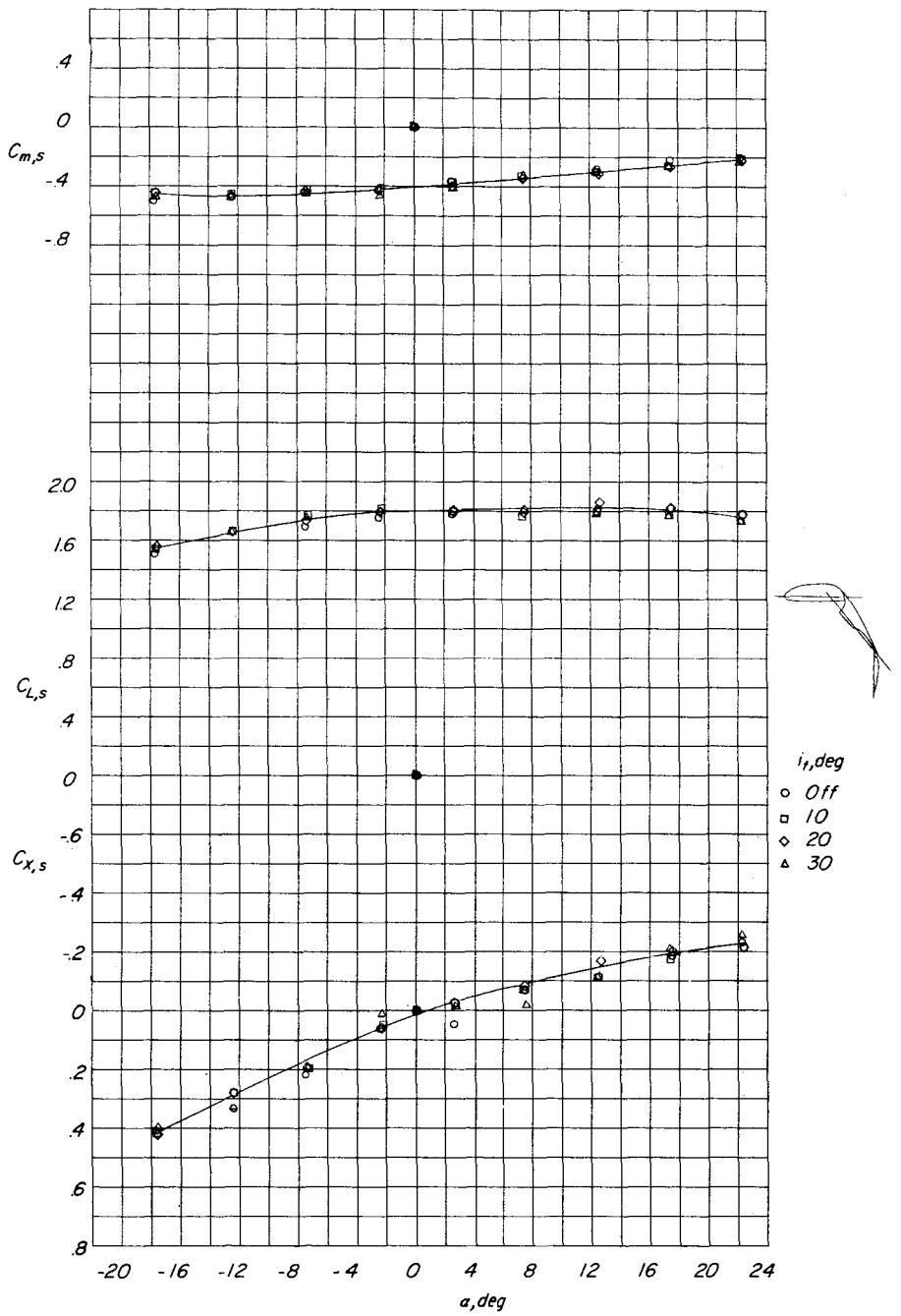

(b) Variation of pitching-moment, lift, and longitudinal-force coefficients with angle of attack.

Figure 13.- Concluded.

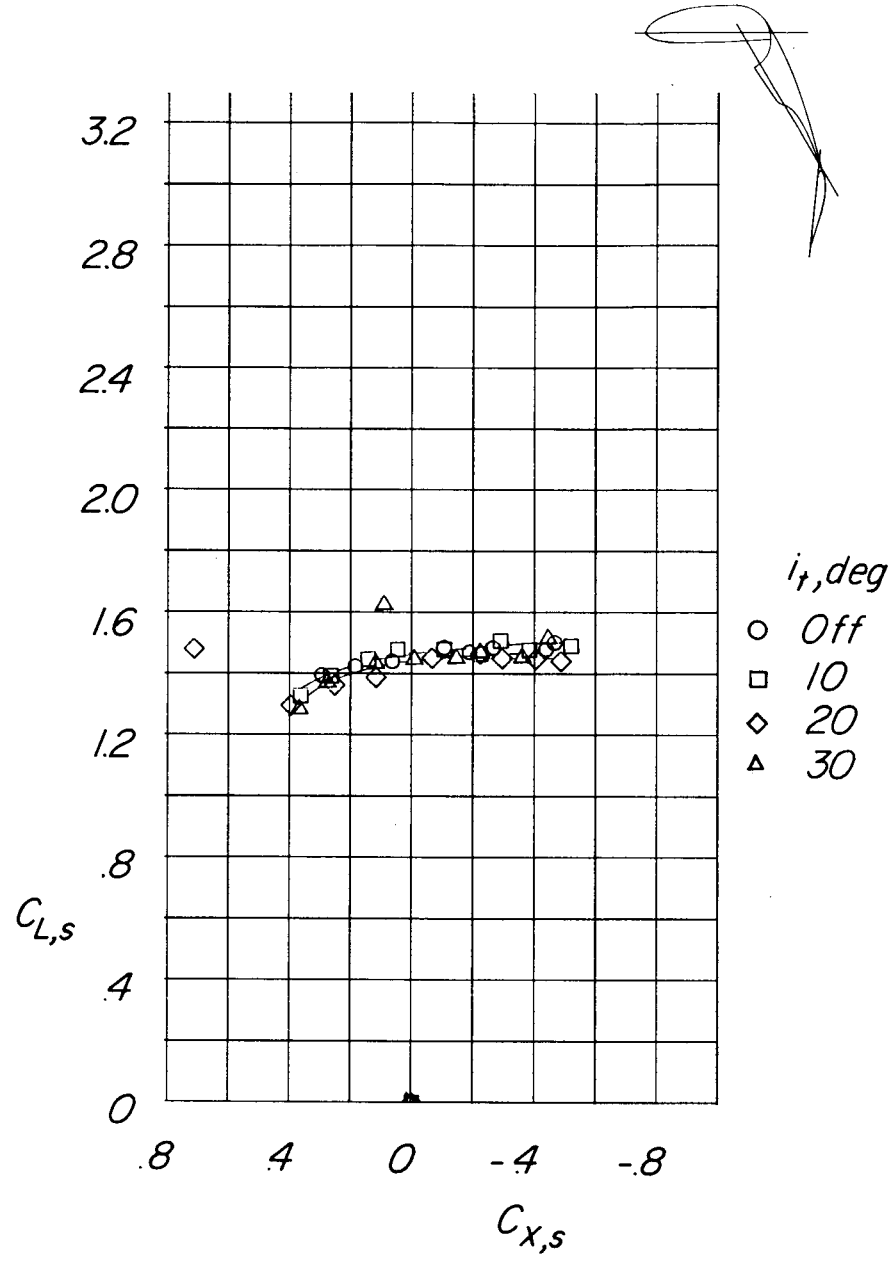

(a) Variation of longitudinal-force coefficient with lift coefficient.

Figure 14.- Effect of stabilizer incidence on longitudinal aerodynamic characteristics out of the region of ground effect. $\delta_{f,S}/\delta_{f,R}$ = 60/40; $C_{T,s}$ = 0.980; C_{μ} = 0.032.

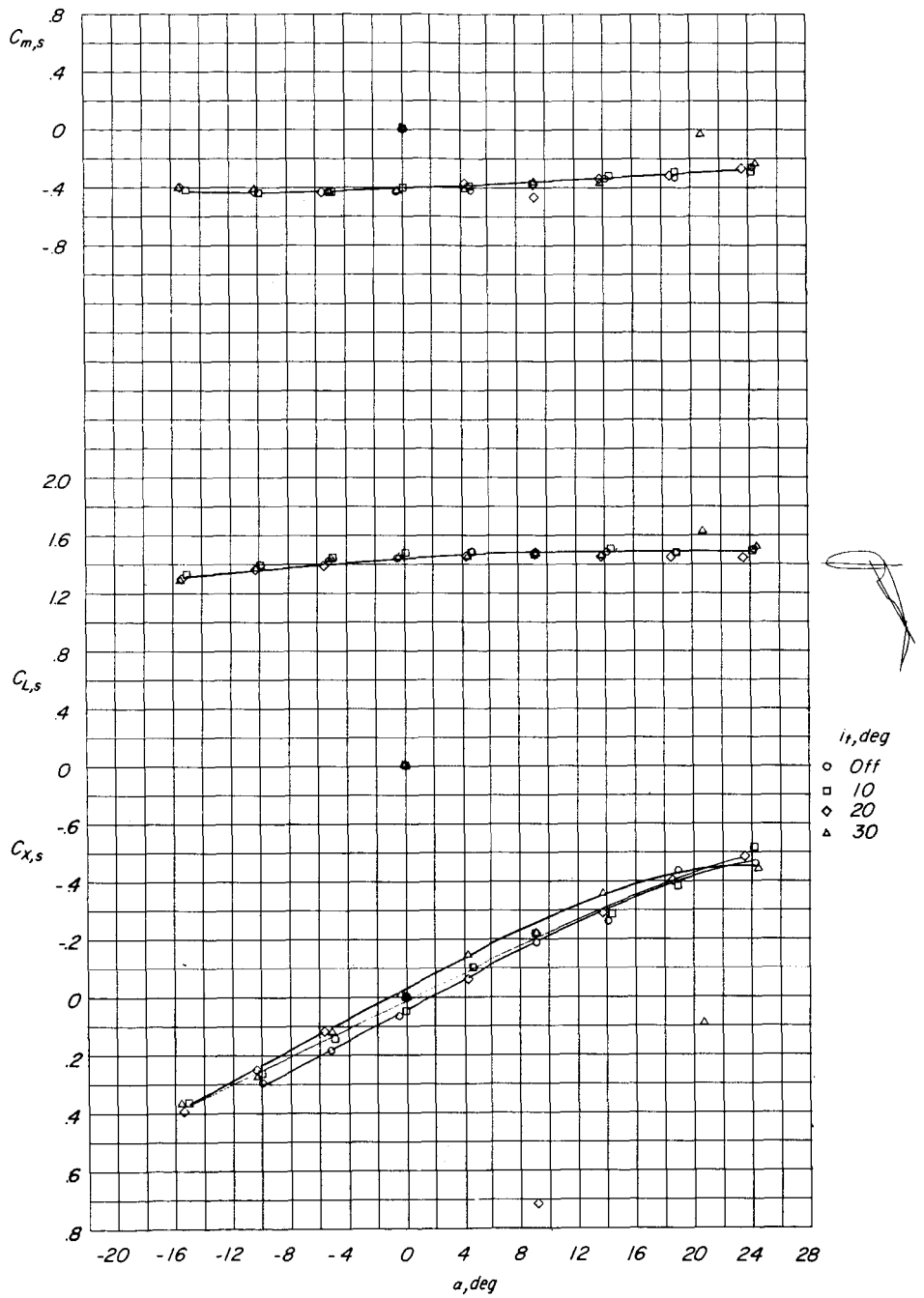

(b) Variation of pitching-moment, lift, and longitudinal-force coefficients with angle of attack.

Figure 14.- Concluded.

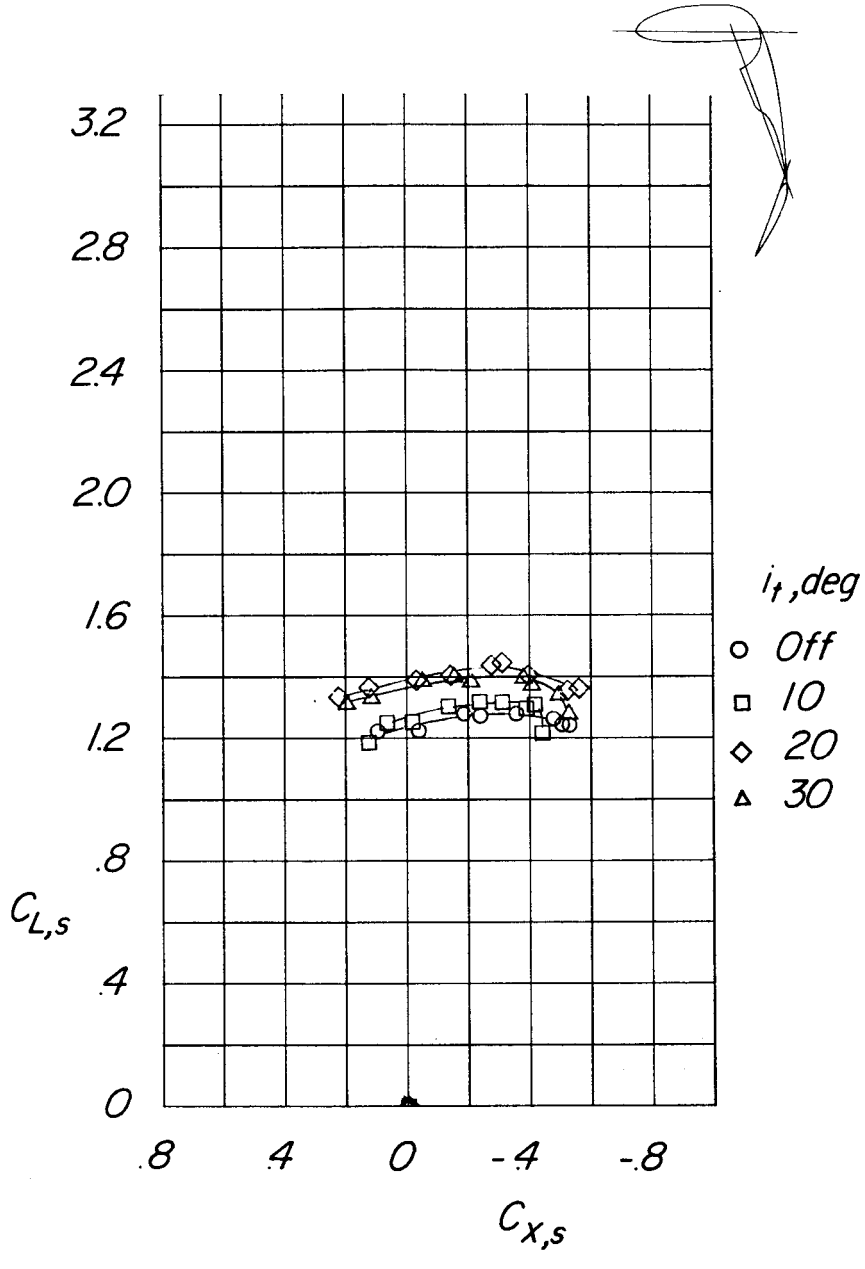

(a) Variation of longitudinal-force coefficient with lift coefficient.

Figure 15.- Effect of stabilizer incidence on longitudinal aerodynamic characteristics out of the region of ground effect. $\delta_{f,S}/\delta_{f,R}$ = 70/40; $C_{T,s}$ = 0.980; C_{μ} = 0.032.

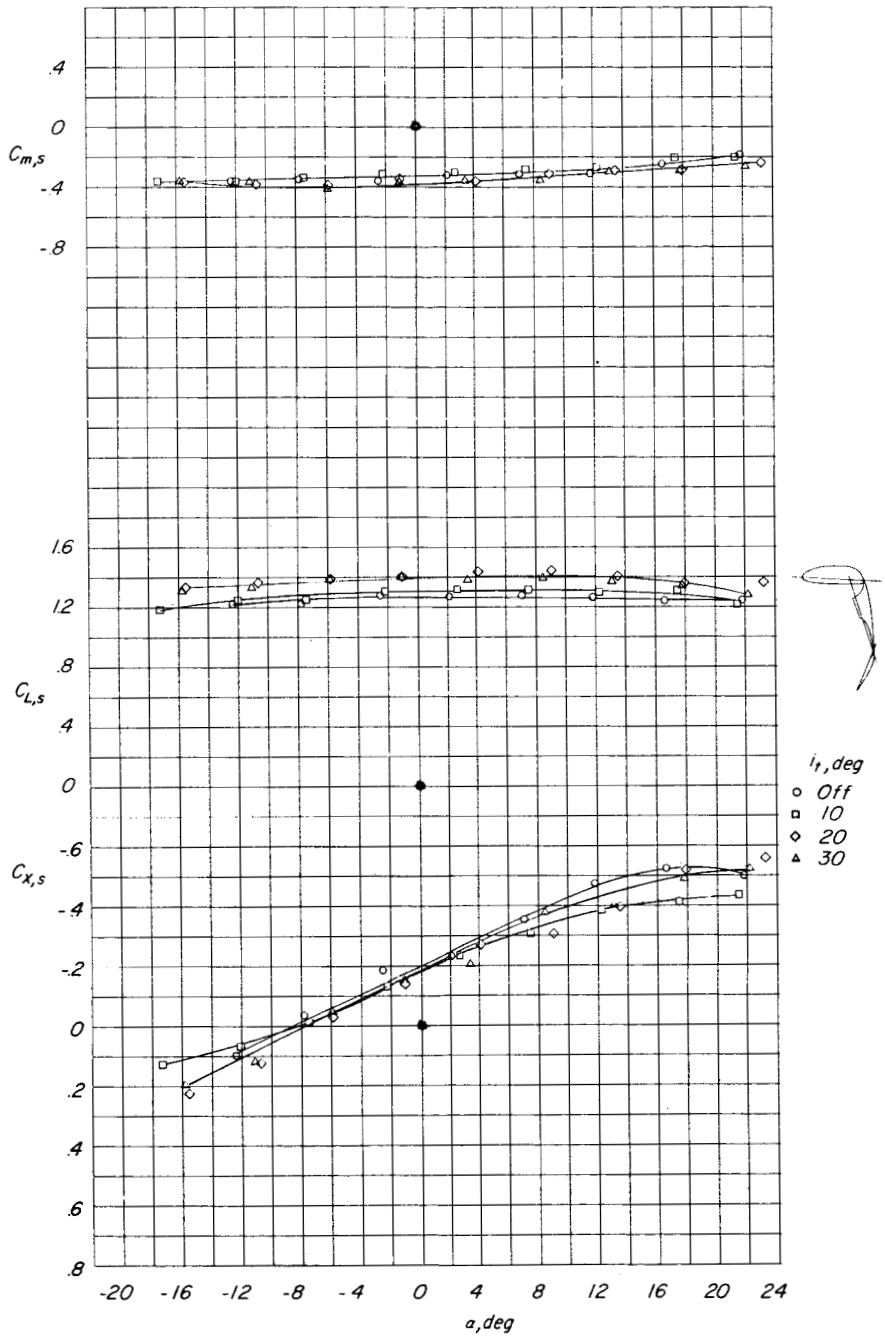

(b) Variation of pitching-moment, lift, and longitudinal-force coefficients with angle of attack.

Figure 15.- Concluded.

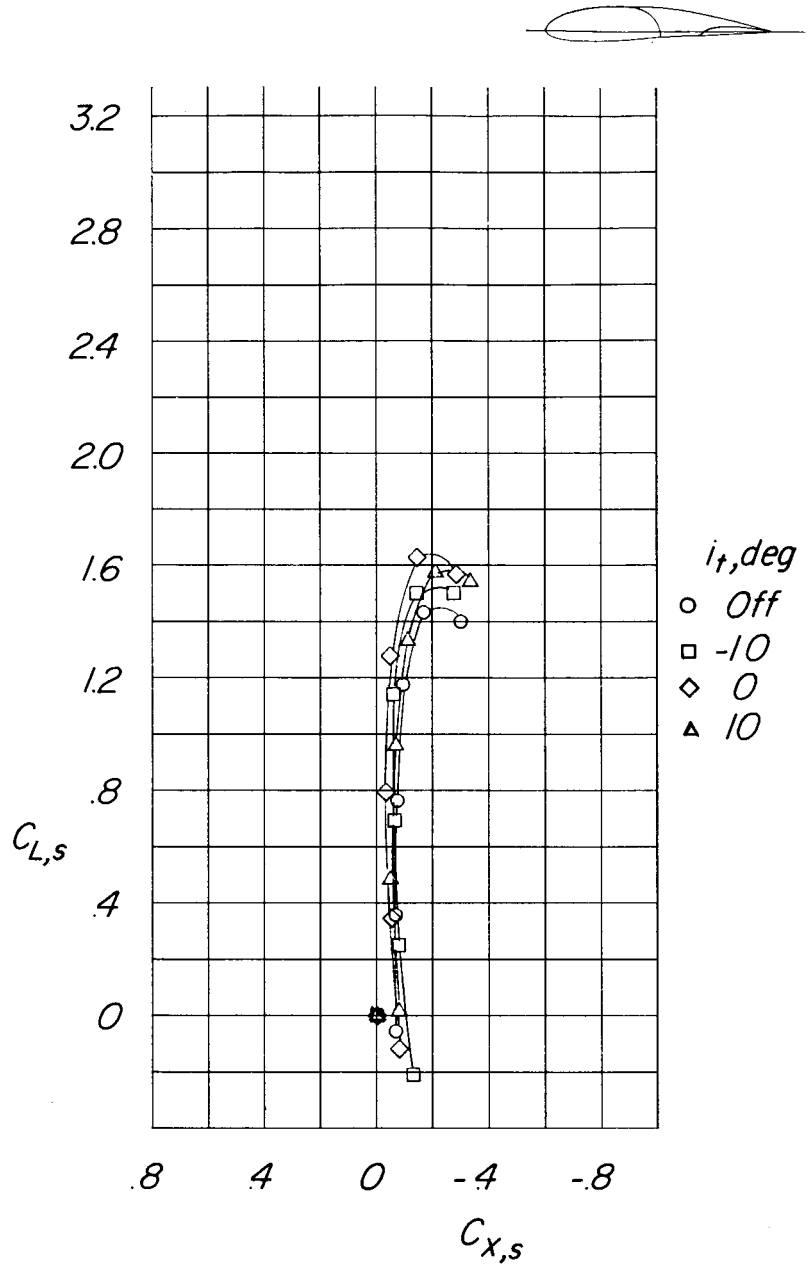

(a) Variation of longitudinal-force coefficient with lift coefficient.

Figure 16.- Effect of stabilizer incidence on longitudinal aerodynamic characteristics within the region of ground effect. $\delta_{f,S}/\delta_{f,R} = 0/0$; $C_{T,s} = 0$ (propellers off); $C_\mu = 0$; $h/D = 0.56$; $h'/D = 0.78$.

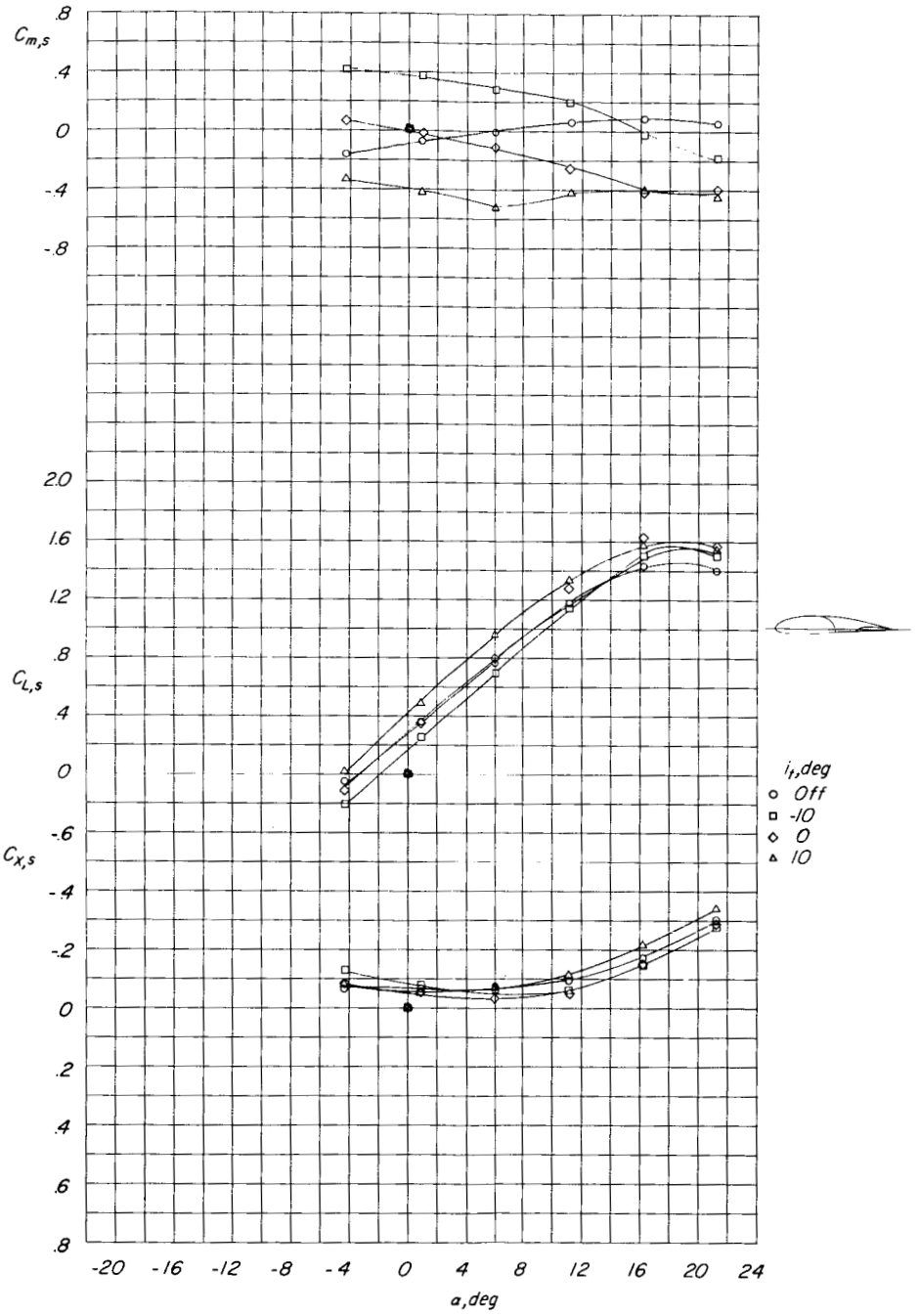

(b) Variation of pitching-moment, lift, and longitudinal-force coefficients with angle of attack.

Figure 16.- Concluded.

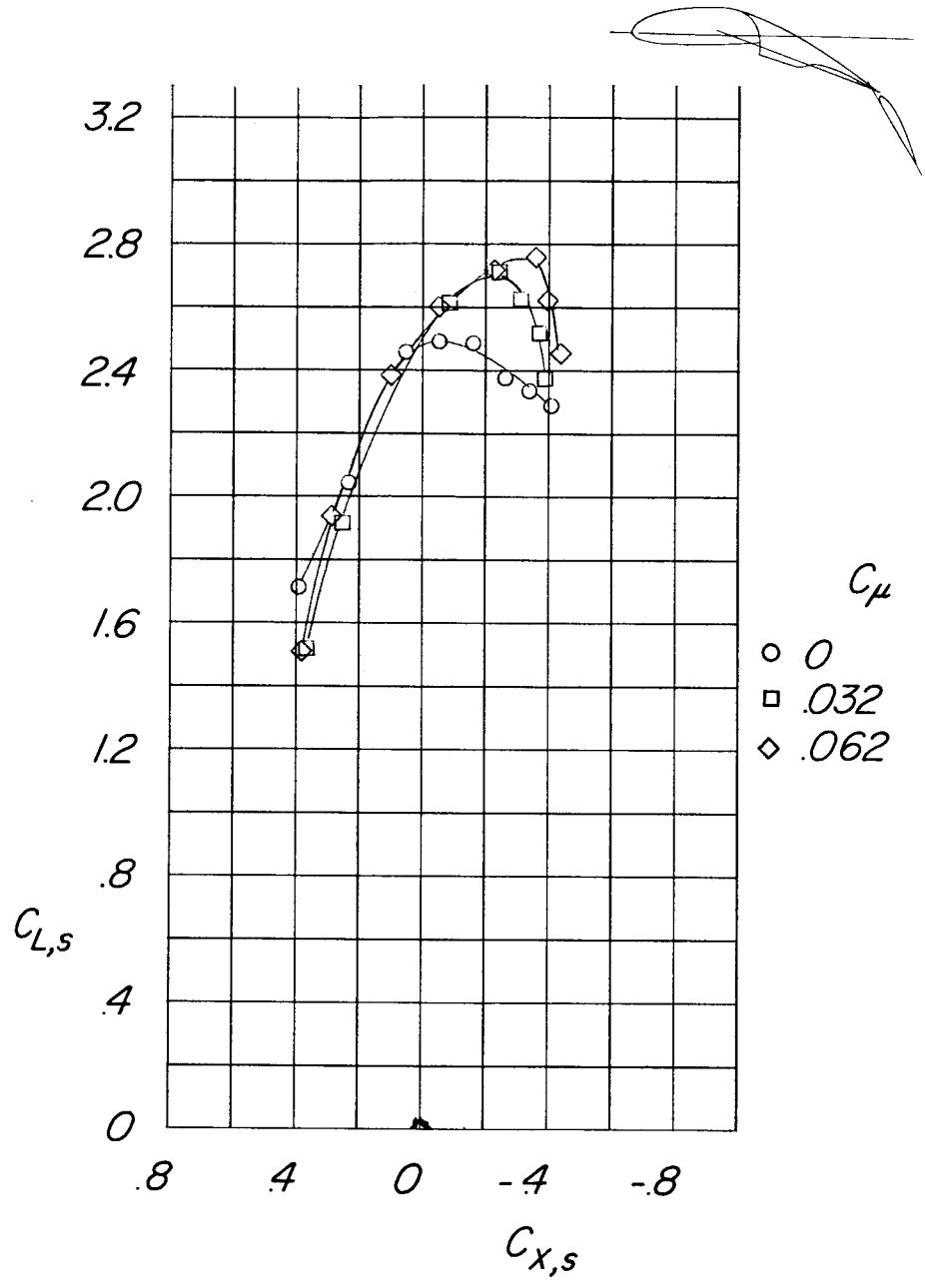

(a) Variation of longitudinal-force coefficient with lift coefficient.

Figure 17.- Effect of boundary-layer control on longitudinal aerodynamic characteristics out of the region of ground effect. $\delta_{f,S}/\delta_{f,R}$ = 20/40; $C_{T,s}$ = 0.510; horizontal tail off.

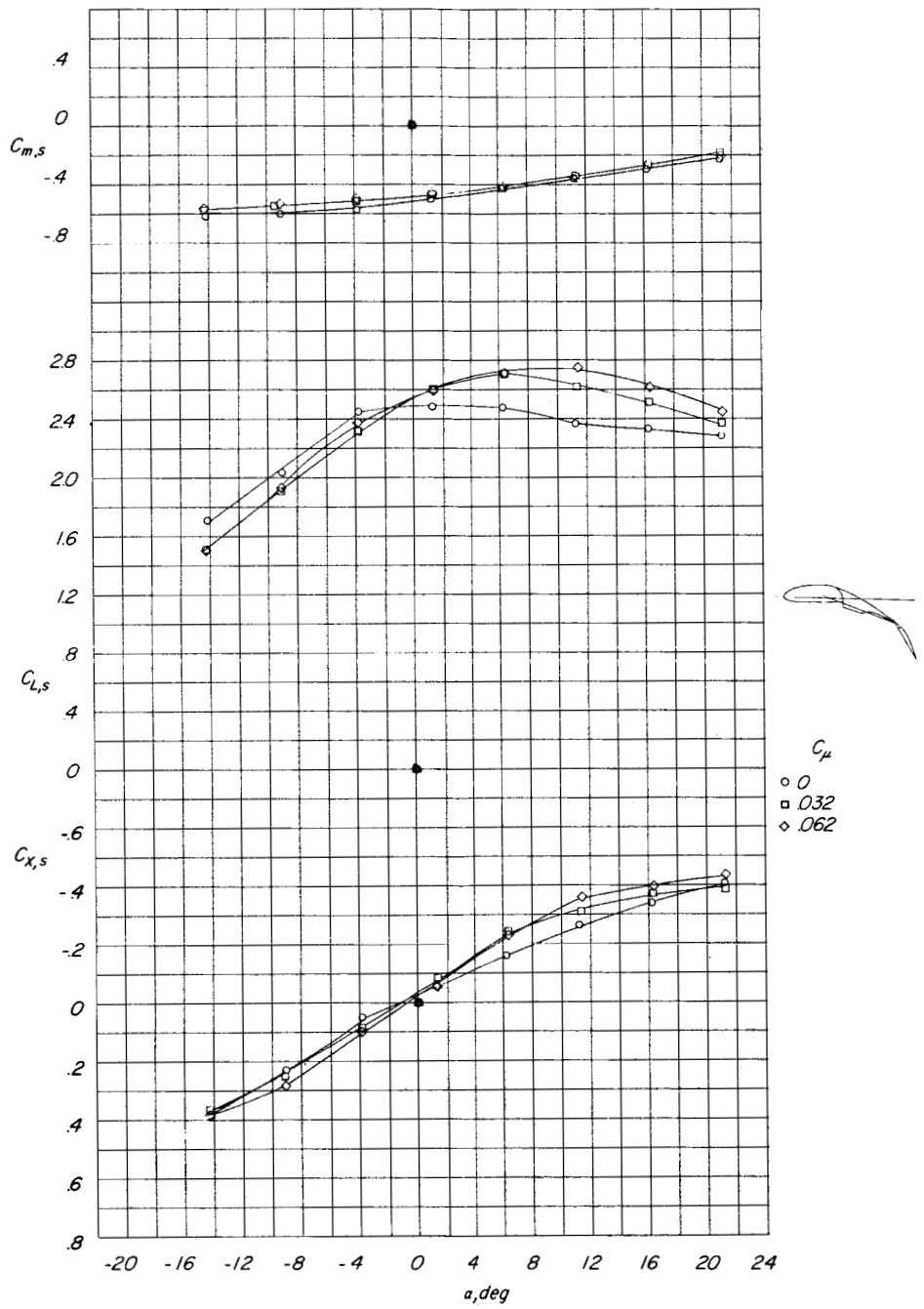

(b) Variation of pitching-moment, lift, and longitudinal-force coefficients with angle of attack.

Figure 17.- Concluded.

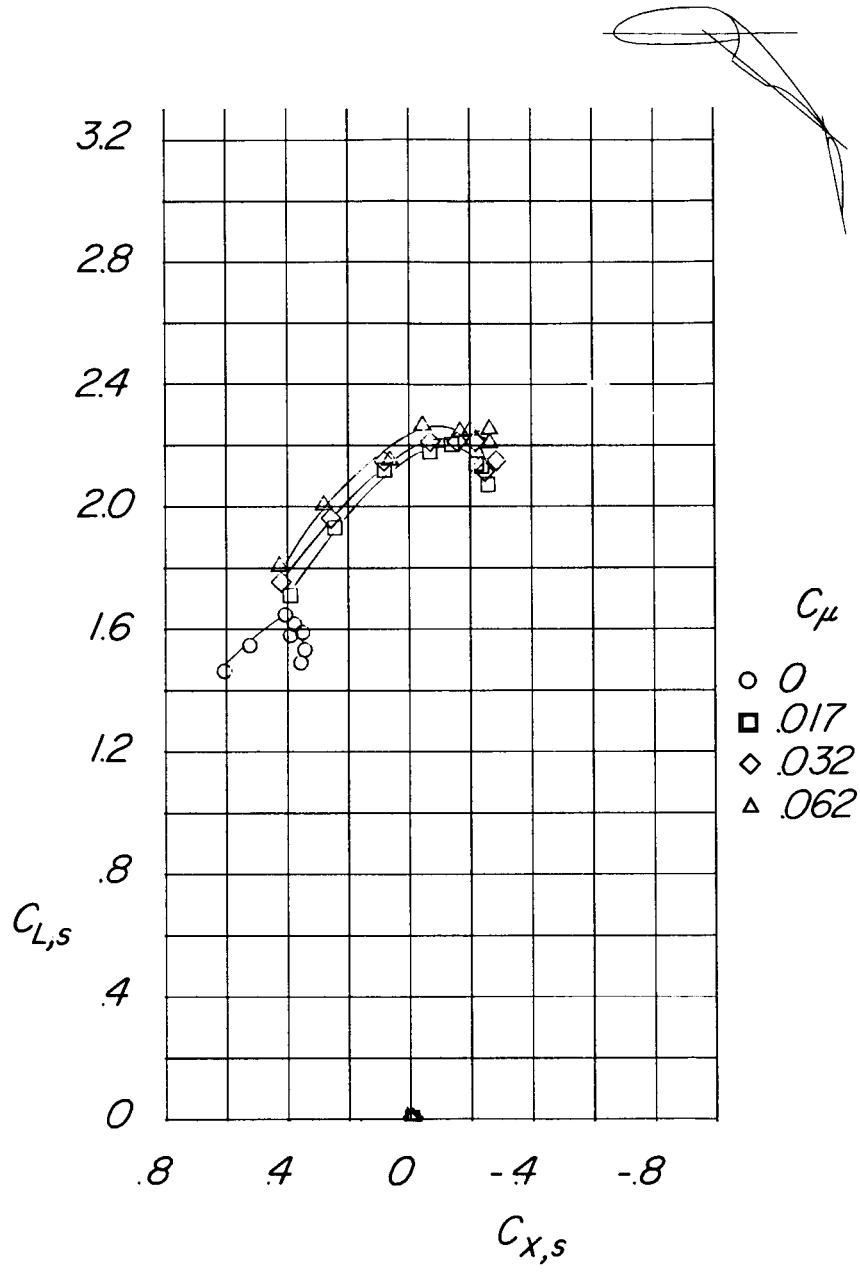

(a) Variation of longitudinal-force coefficient with lift coefficient.

Figure 18.- Effect of boundary-layer control on longitudinal aerodynamic characteristics out of the region of ground effect. $\delta_{f,S}/\delta_{f,R}$ = 40/40; $C_{T,s}$ = 0.845; horizontal tail off.

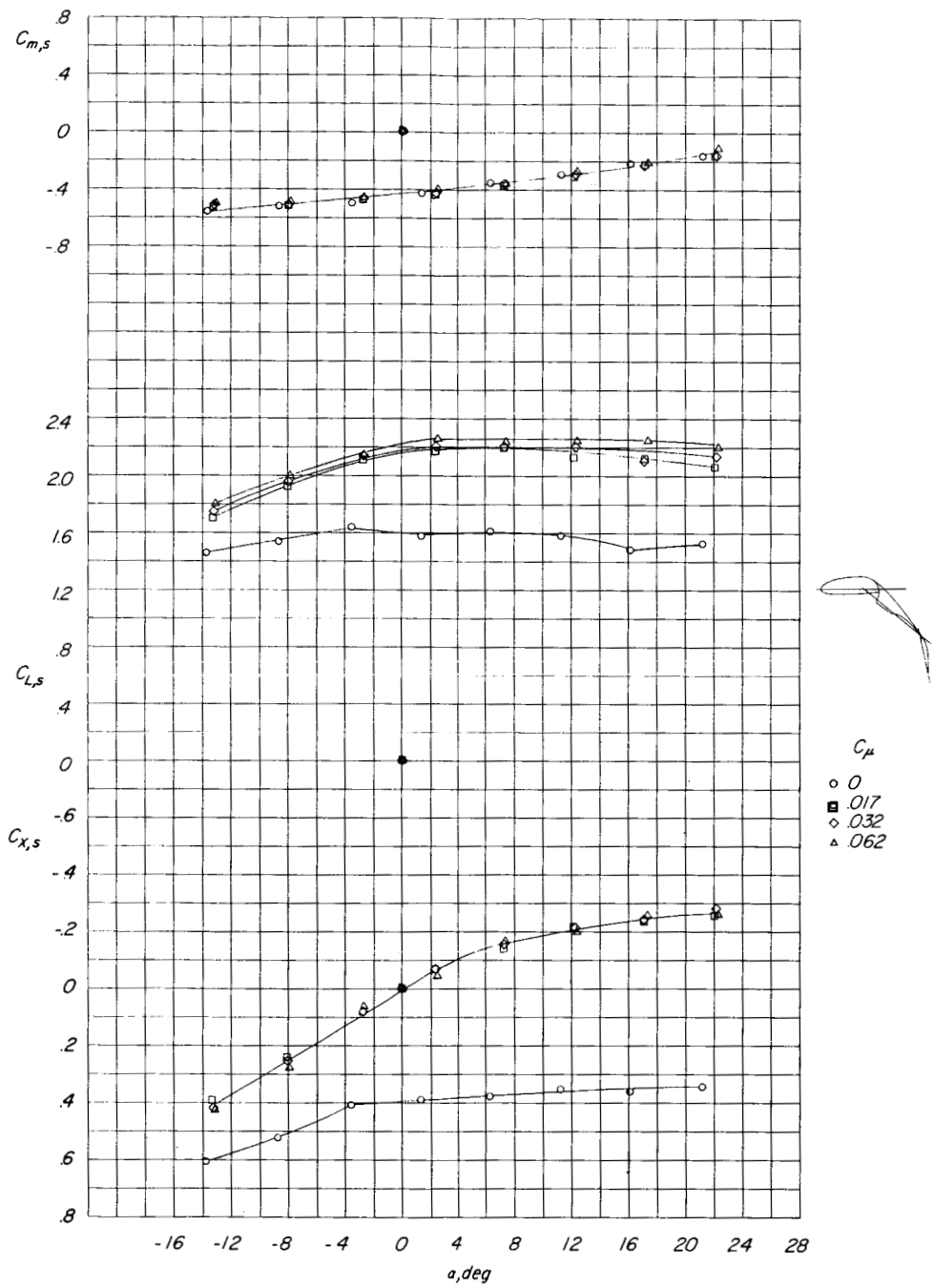

(b) Variation of pitching-moment, lift, and longitudinal-force coefficients with angle of attack.

Figure 18.- Concluded.

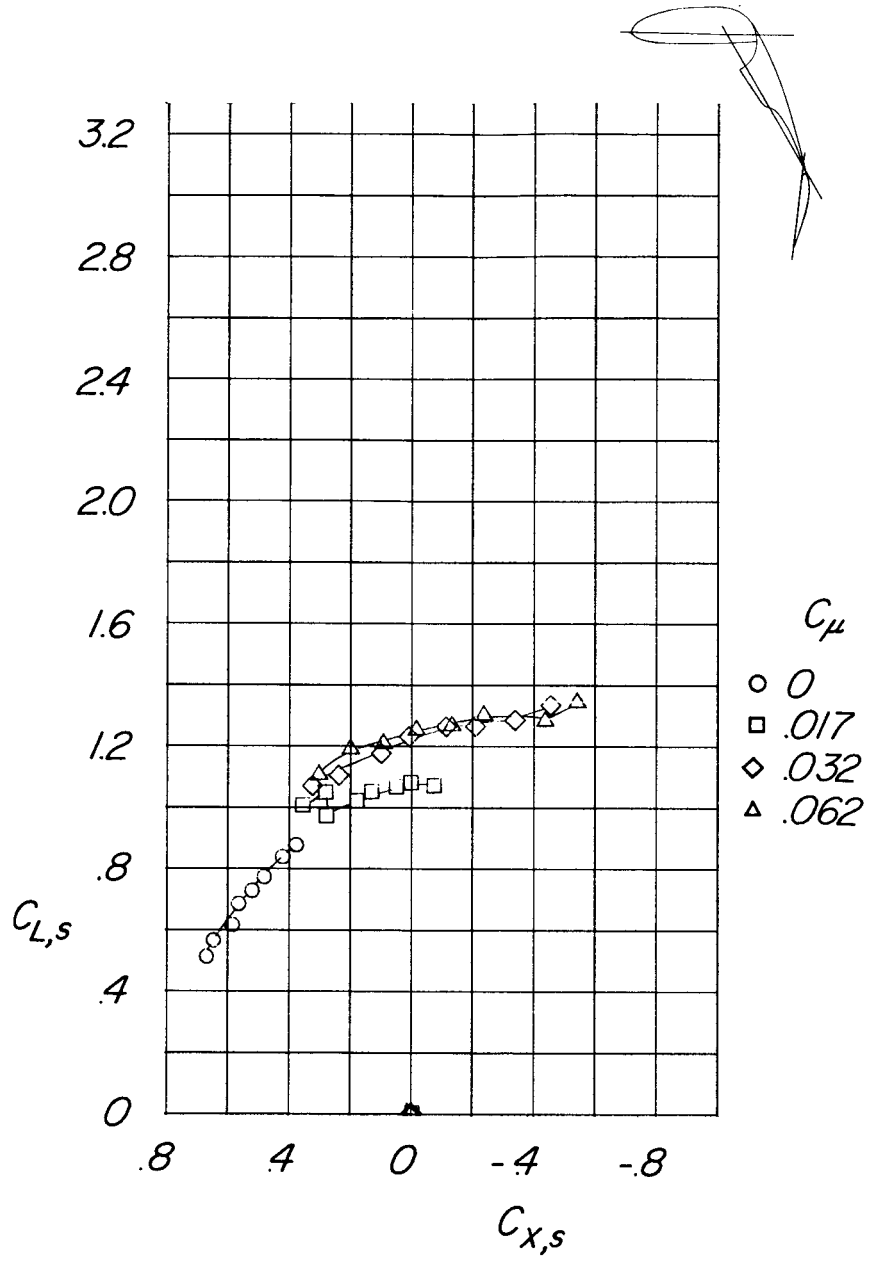

(a) Variation of longitudinal-force coefficient with lift coefficient.

Figure 19.- Effect of boundary-layer control on longitudinal aerodynamic characteristics out of the region of ground effect. $\delta_{f,S}/\delta_{f,R}$ = 60/40; $C_{T,s}$ = 0.984; horizontal tail off.

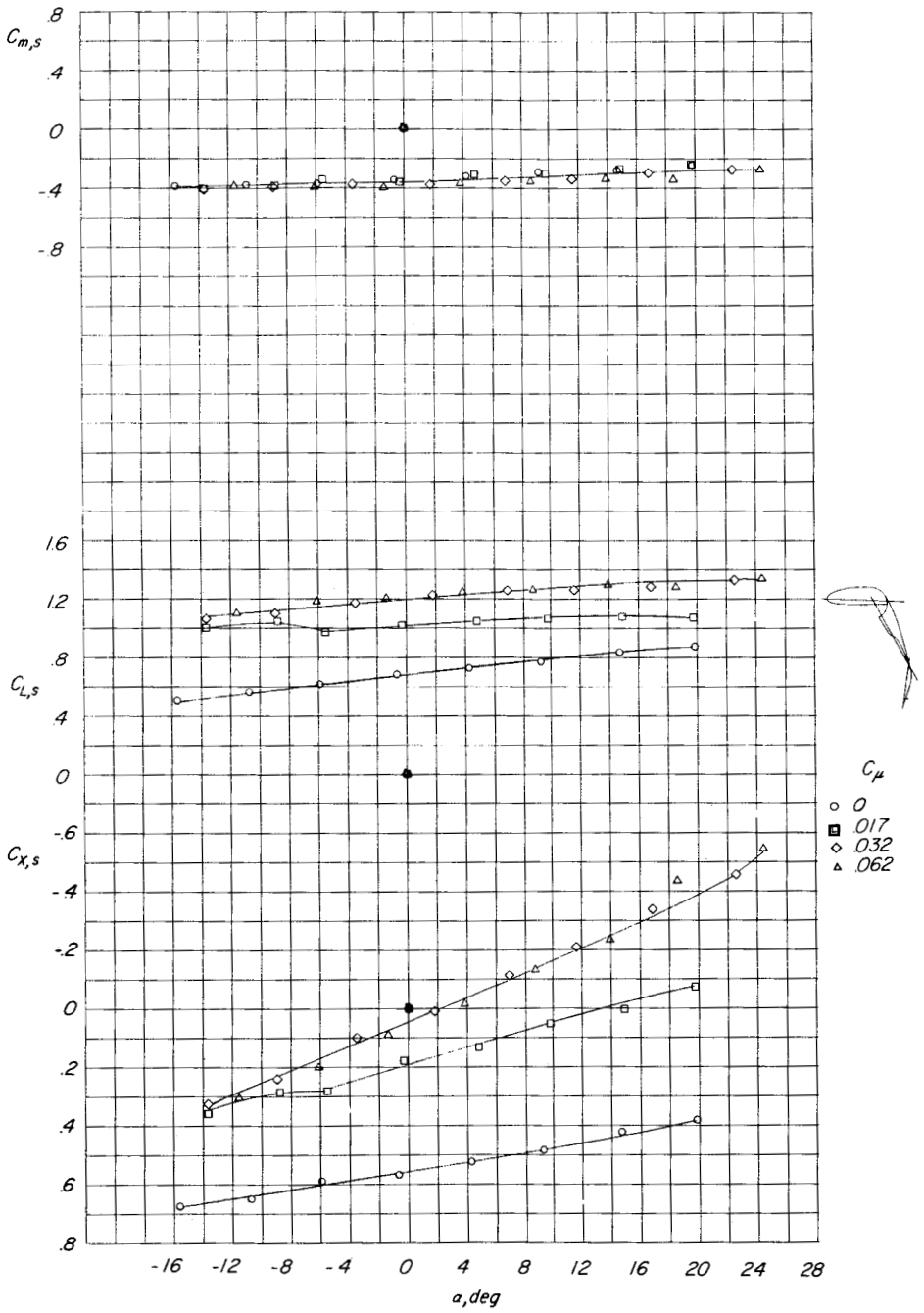

(b) Variation of pitching-moment, lift, and longitudinal-force coefficients with angle of attack.

Figure 19.- Concluded.

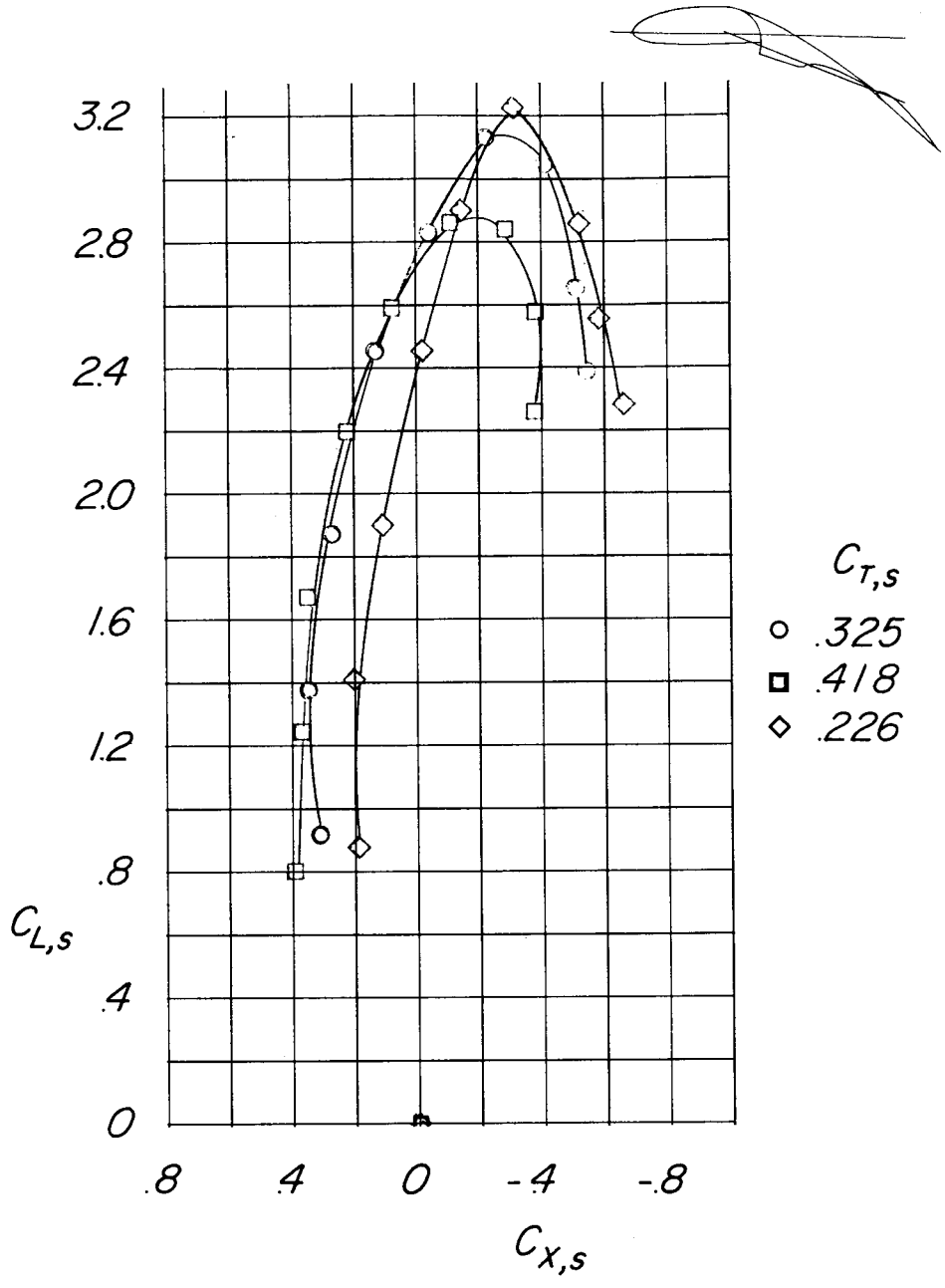

(a) Variation of longitudinal-force coefficient with lift coefficient.

Figure 20.- Effect of variation in thrust coefficient on longitudinal aerodynamic characteristics out of the region of ground effect. $\delta_{f,S}/\delta_{f,R}$ = 20/20; i_t = 0°; C_μ = 0.032.

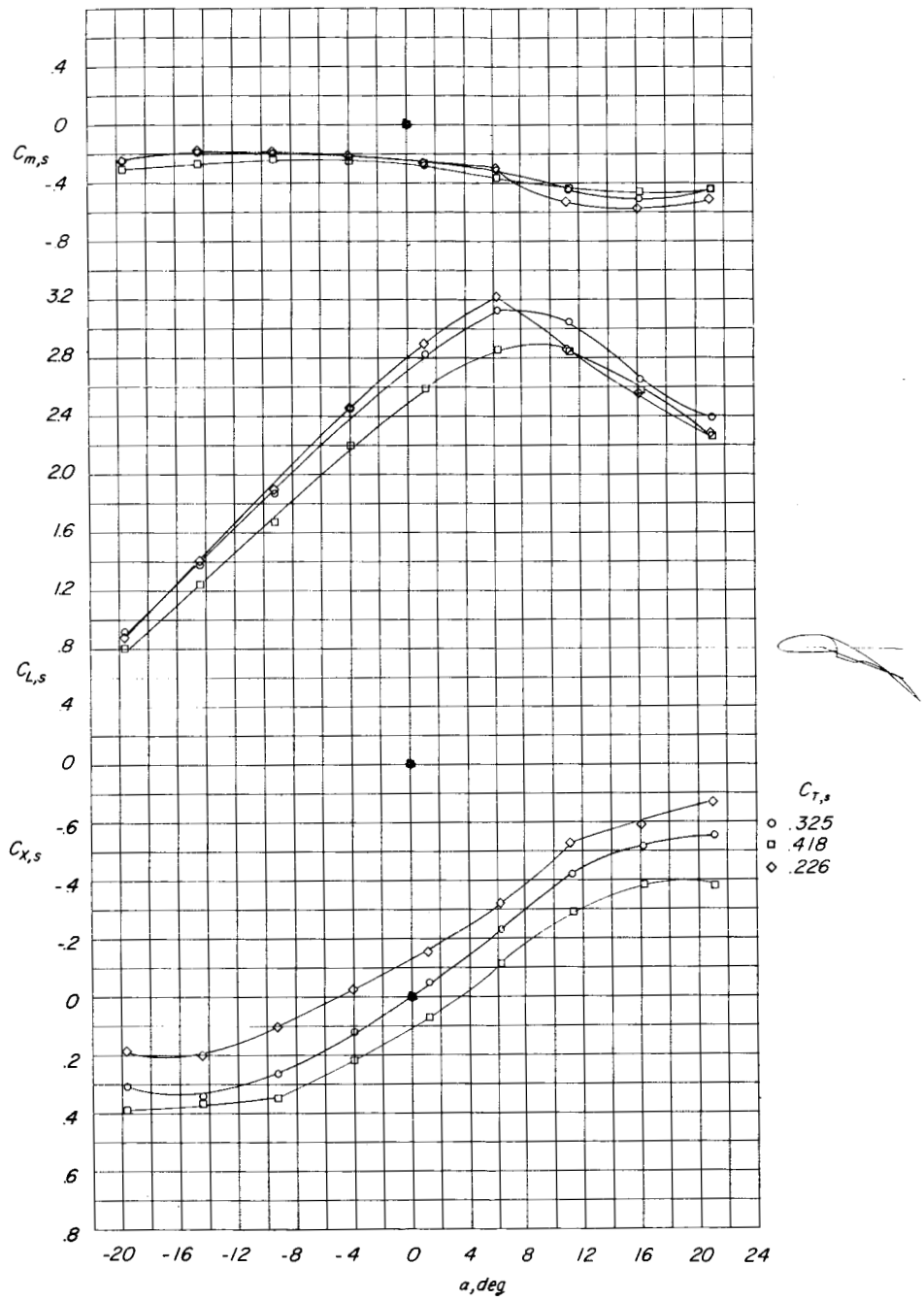

(b) Variation of pitching-moment, lift, and longitudinal-force coefficients with angle of attack.

Figure 20.- Concluded.

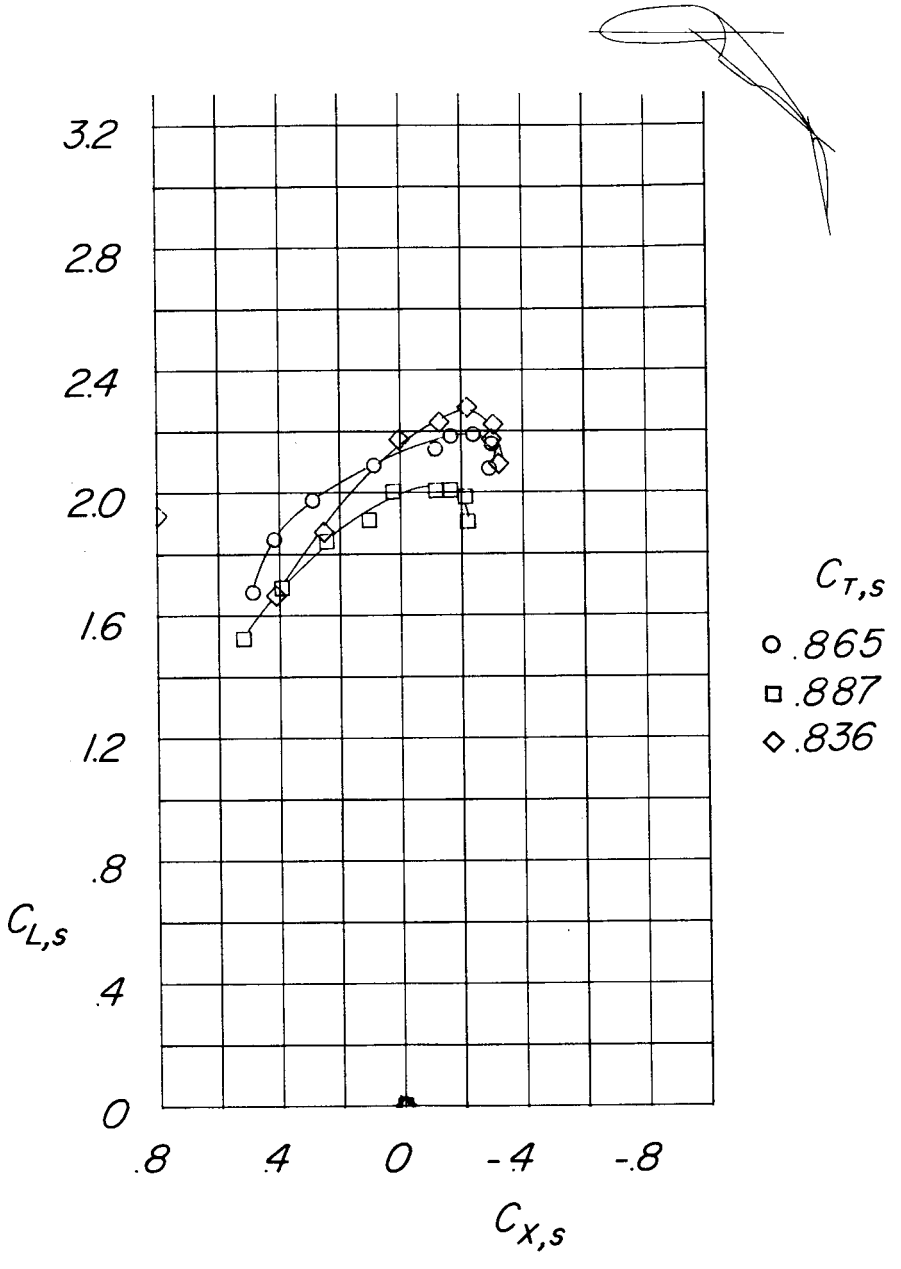

(a) Variation of longitudinal-force coefficient with lift coefficient.

Figure 21.- Effect of variation in thrust coefficient on longitudinal aerodynamic characteristics out of the region of ground effect. $\delta_{f,S}/\delta_{f,R}$ = 40/40; i_t = 0°; C_μ = 0.032.

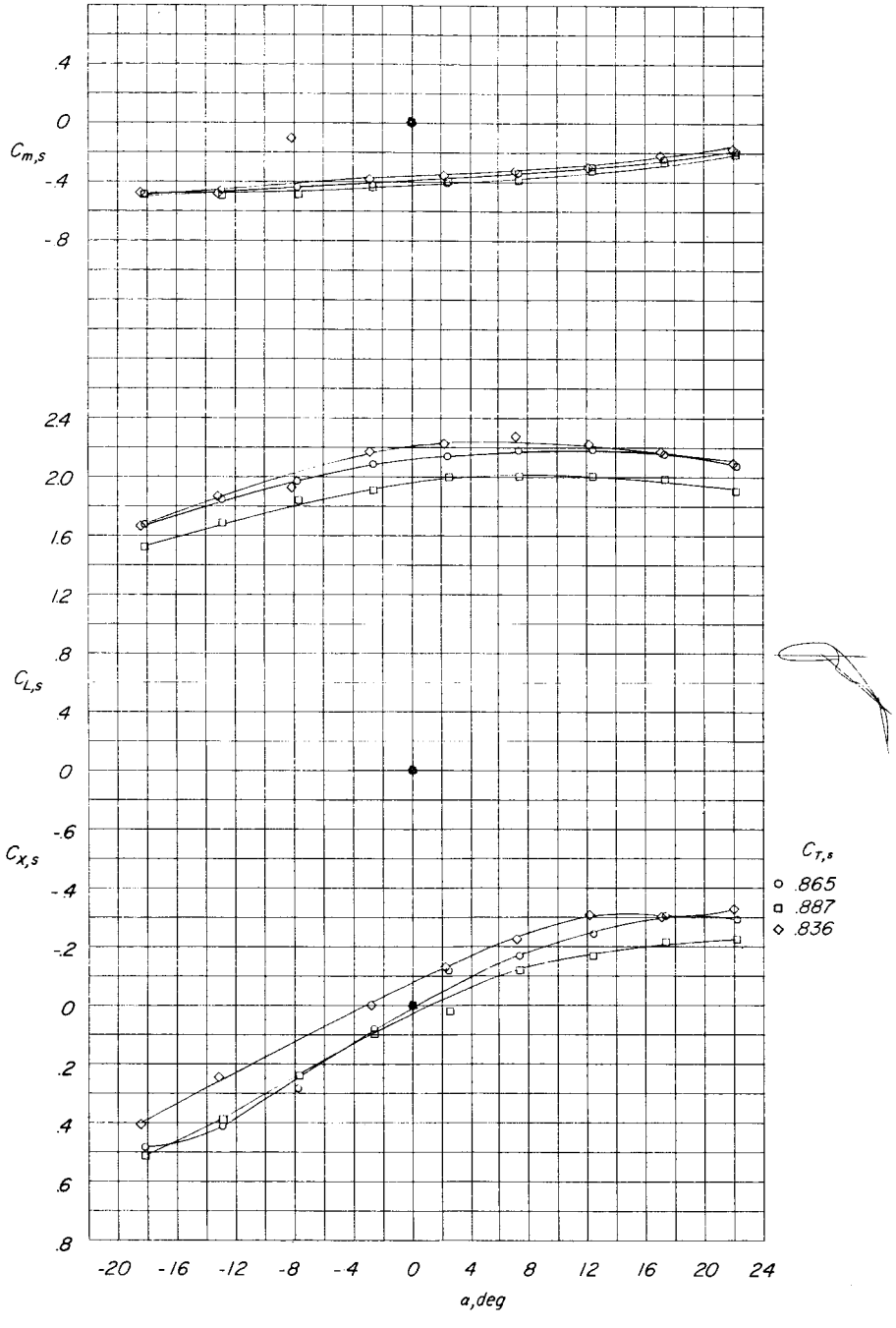

(b) Variation of pitching-moment, lift, and longitudinal-force coefficients with angle of attack.

Figure 21.- Concluded.

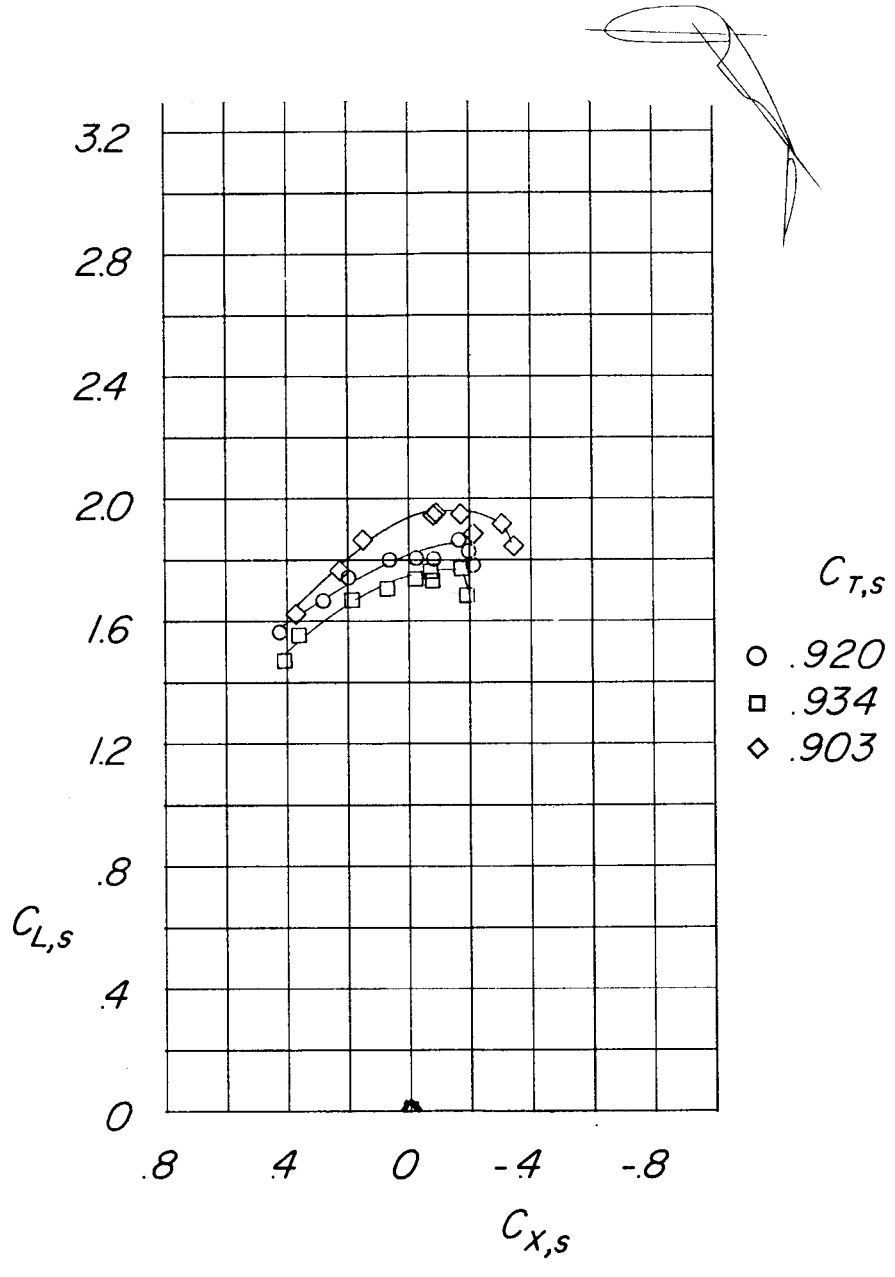

(a) Variation of longitudinal-force coefficient with lift coefficient.

Figure 22.- Effect of variation in thrust coefficient on longitudinal aerodynamic characteristics out of the region of ground effect. $\delta_{f,S}/\delta_{f,R}$ = 50/40; i_t = 20°; C_μ = 0.032.

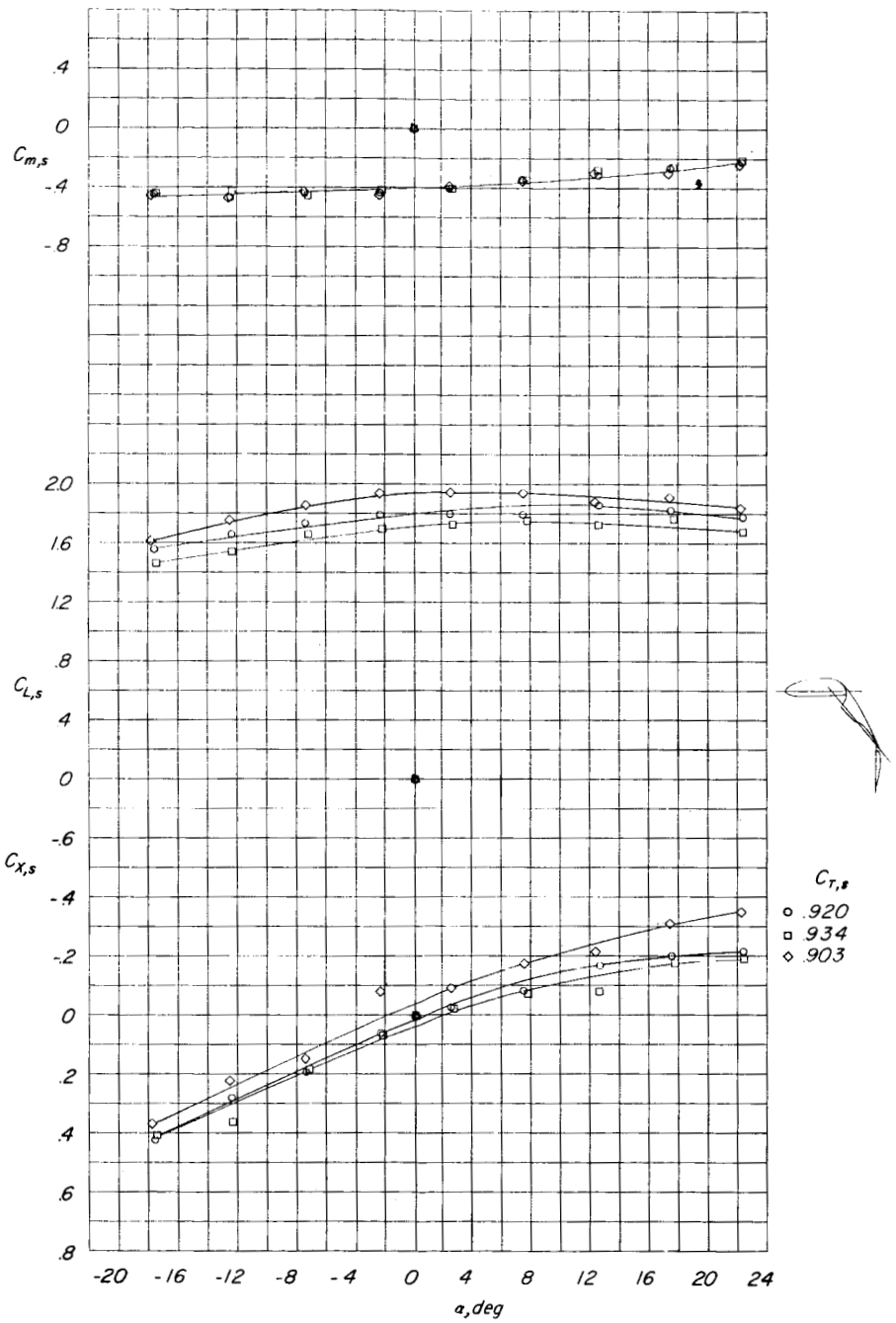

(b) Variation of pitching-moment, lift, and longitudinal-force coefficients with angle of attack.

Figure 22.- Concluded.

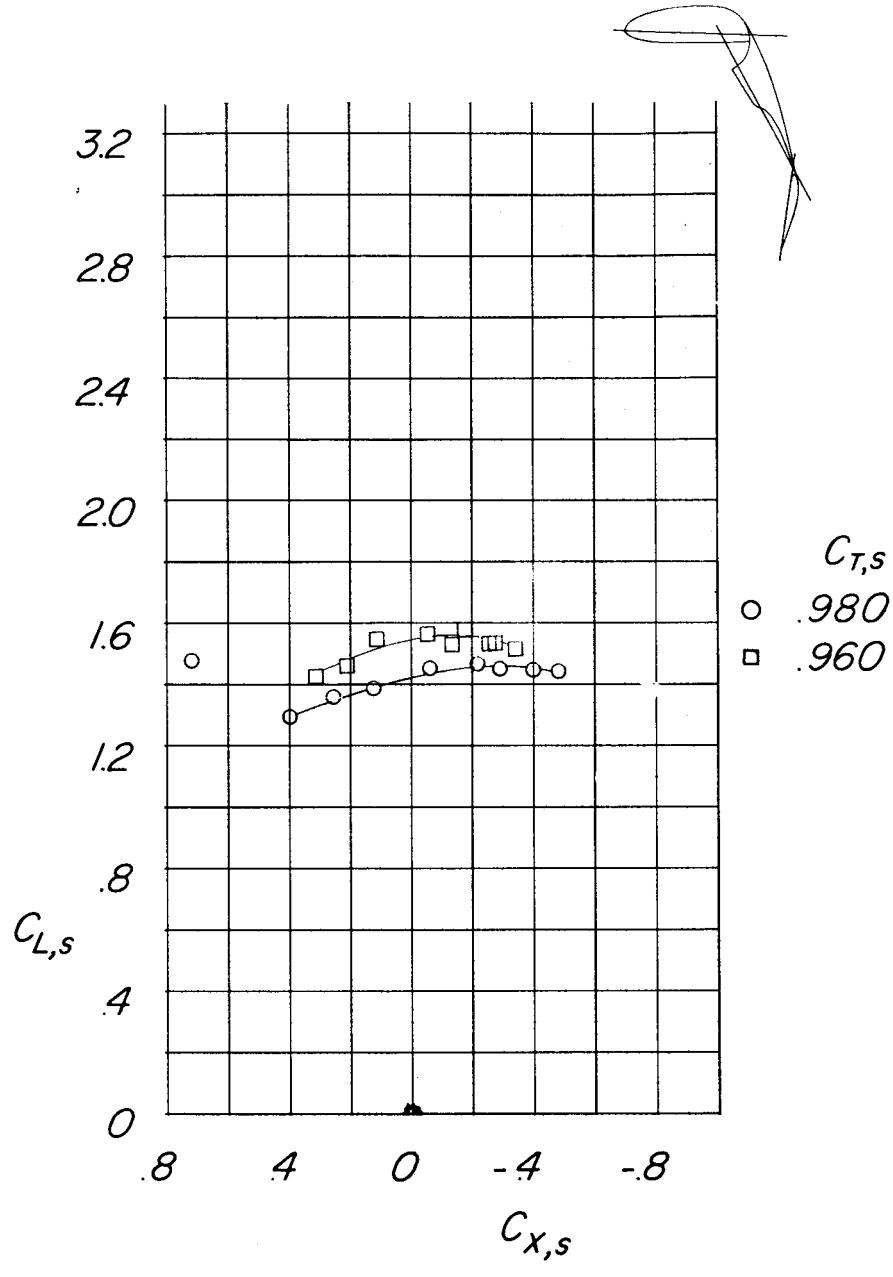

(a) Variation of longitudinal-force coefficient with lift coefficient.

Figure 23.- Effect of variation in thrust coefficient on longitudinal aerodynamic characteristics out of the region of ground effect. $\delta_{f,S}/\delta_{f,R}$ = 60/40; i_t = 20°; C_μ = 0.032.

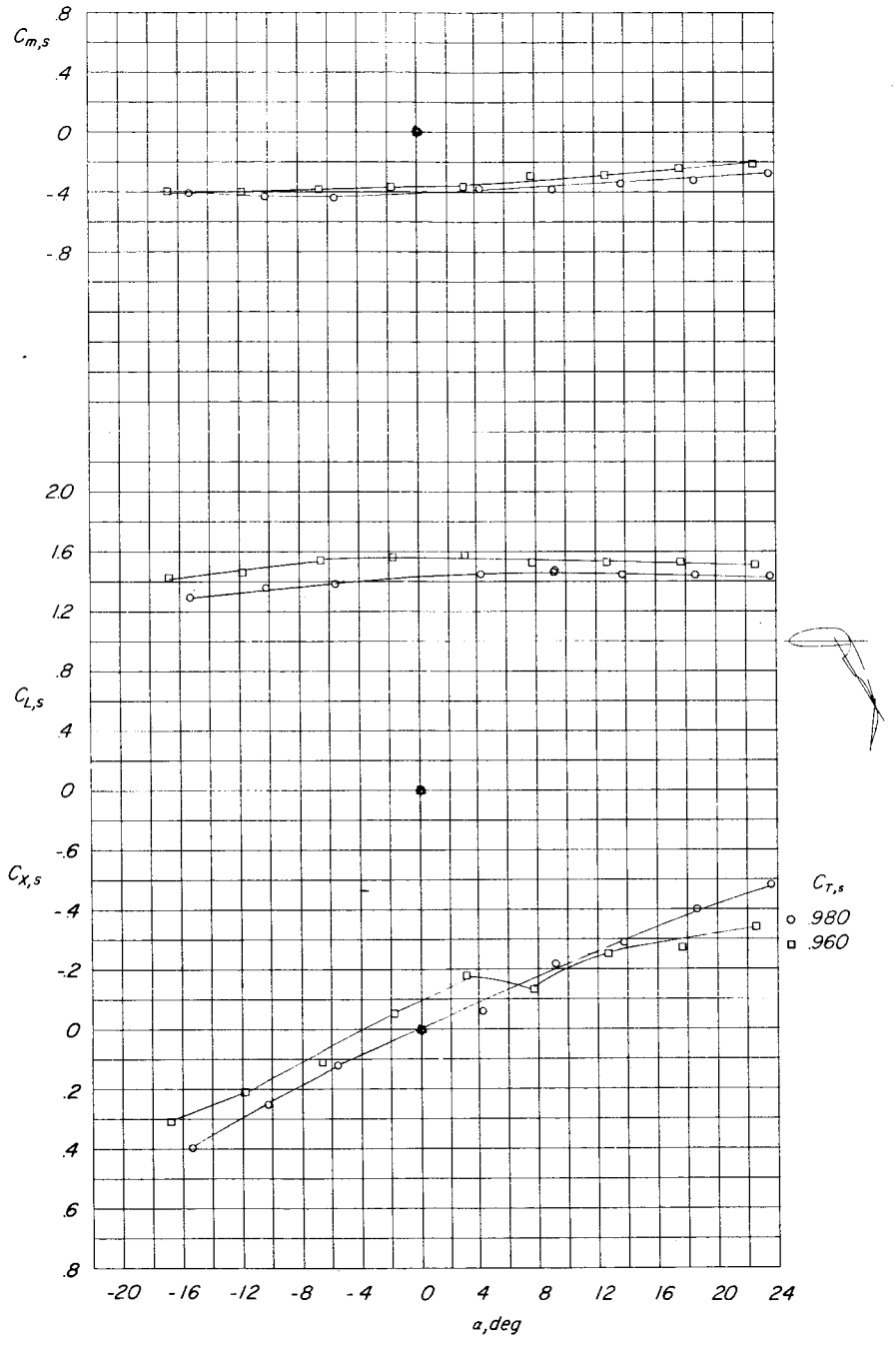

(b) Variation of pitching-moment, lift, and longitudinal-force coefficients with angle of attack.

Figure 23.- Concluded.

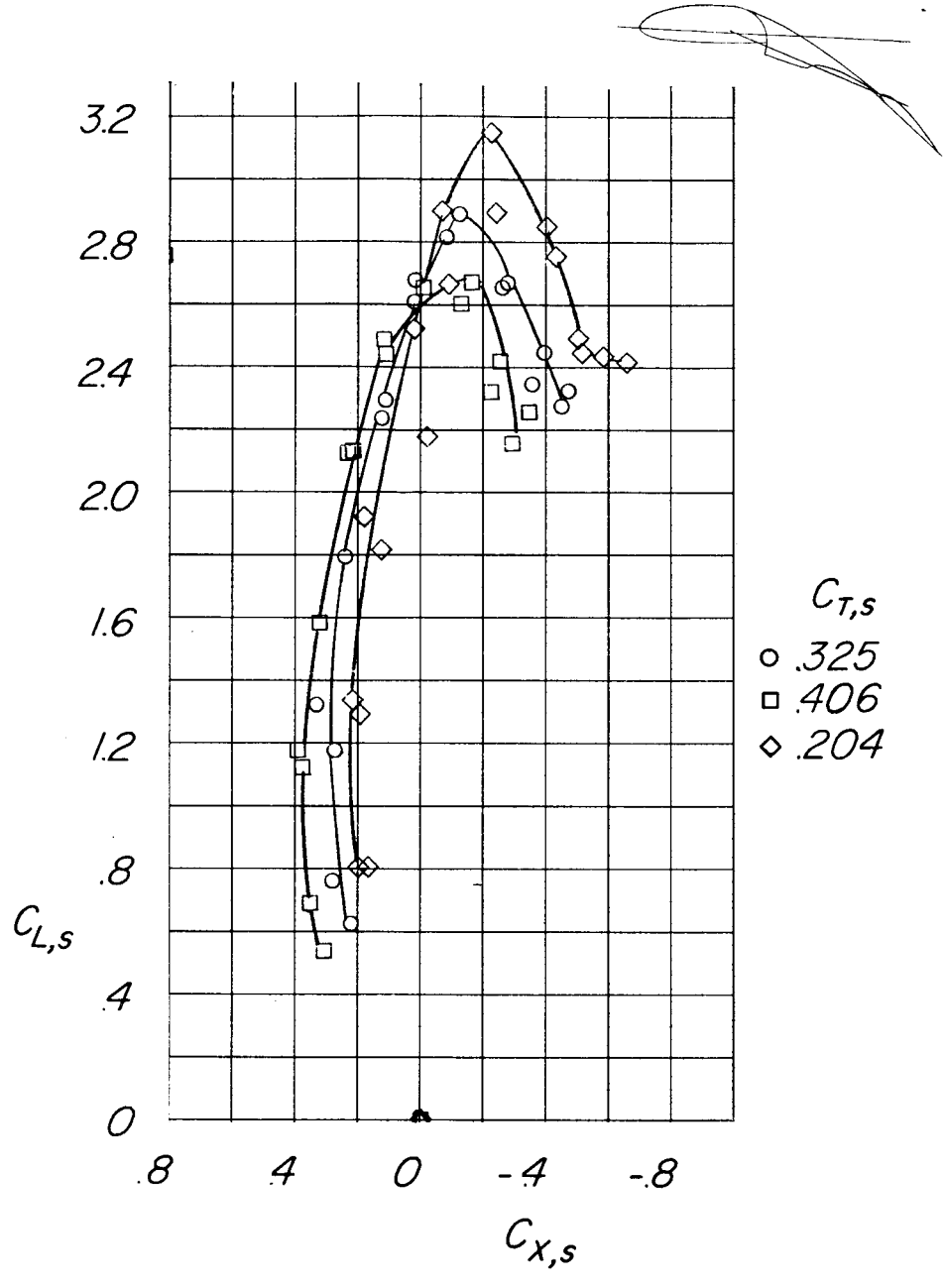

(a) Variation of longitudinal-force coefficient with lift coefficient.

Figure 24.- Effect of variation in thrust coefficient on longitudinal aerodynamic characteristics in the region of ground effect. $\delta_{f,S}/\delta_{f,R}$ = 20/20; i_t = 0°; C_μ = 0.032; h/D = 0.94; h'/D = 0.87.

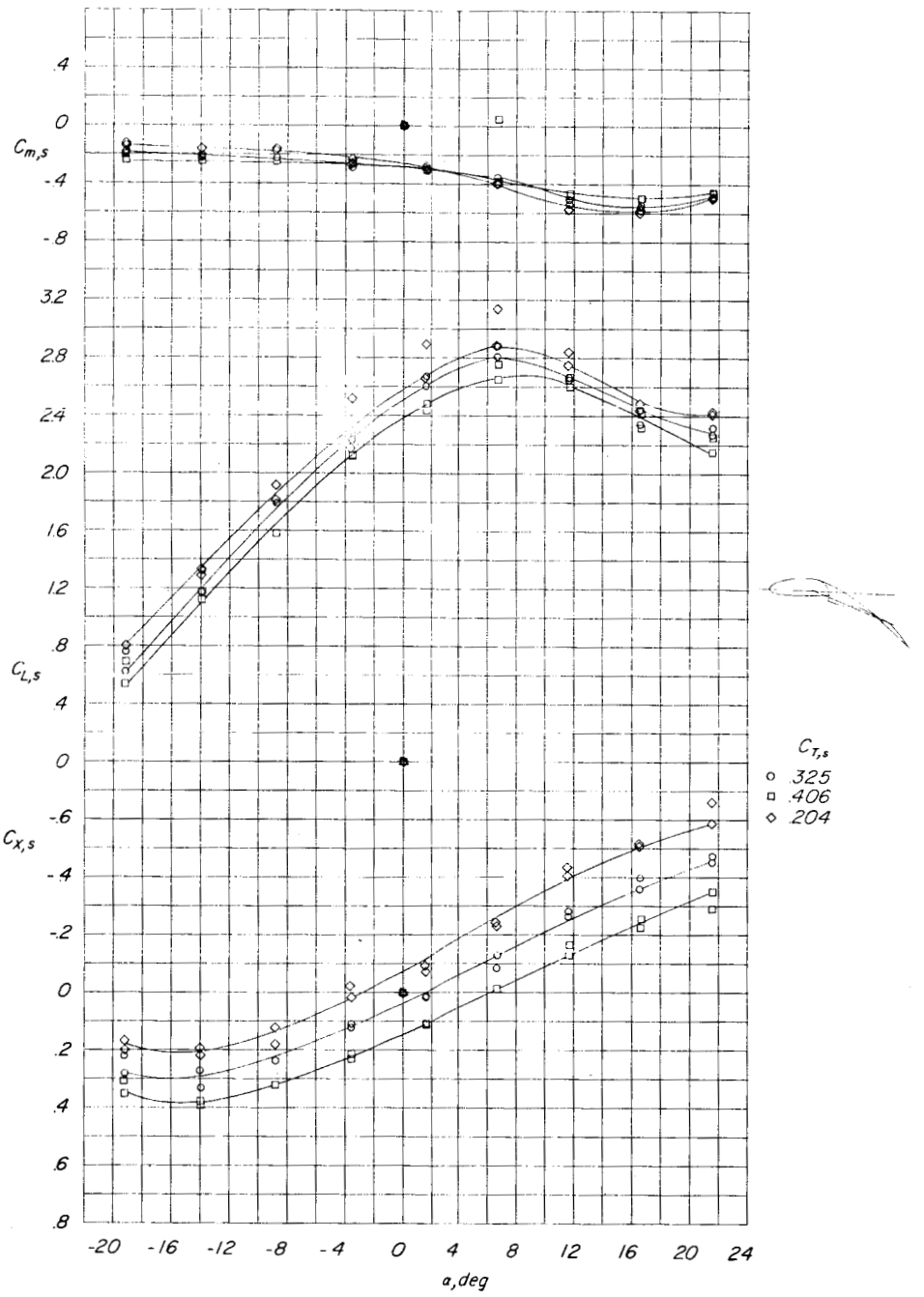

(b) Variation of pitching-moment, lift, and longitudinal-force coefficients with angle of attack.

Figure 24.- Concluded.

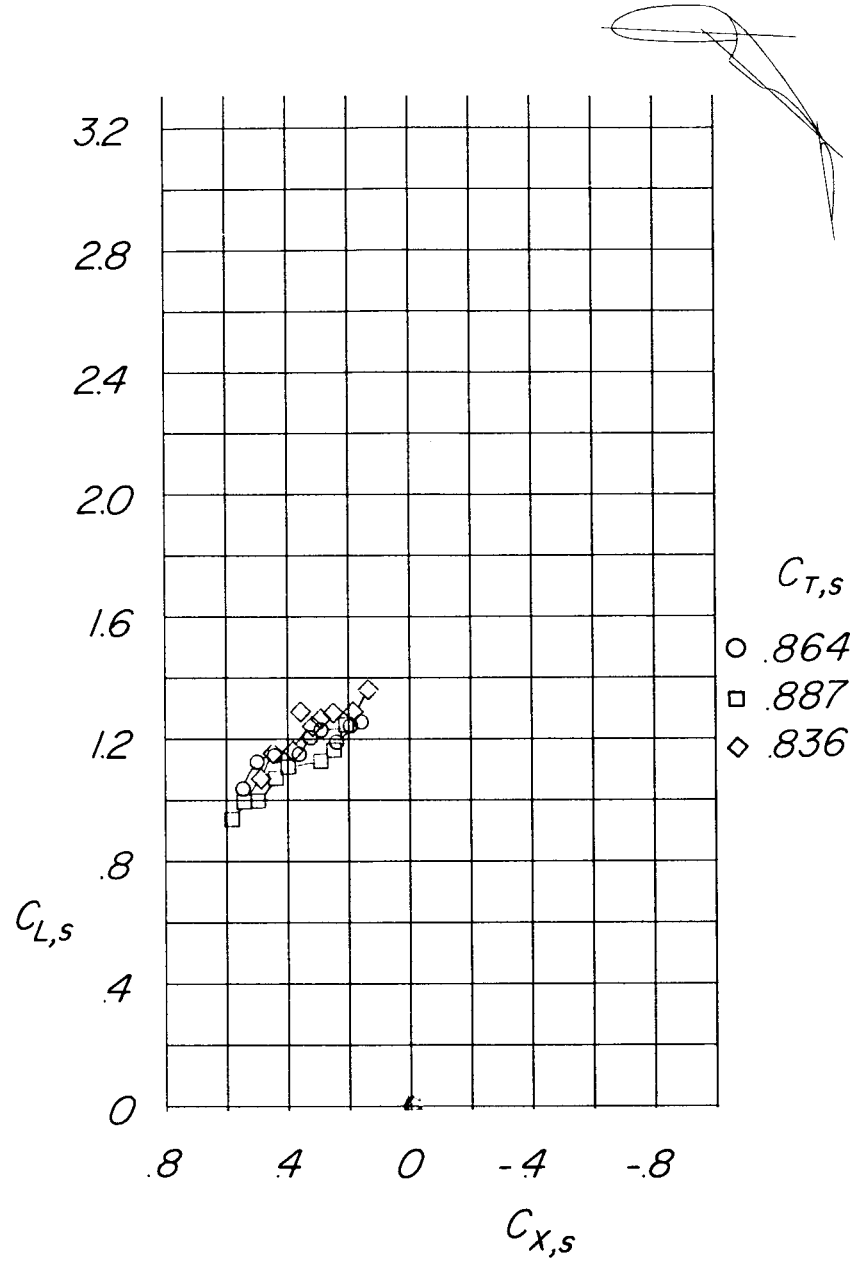

(a) Variation of longitudinal-force coefficient with lift coefficient.

Figure 25.- Effect of variation in thrust coefficient on longitudinal aerodynamic characteristics in the region of ground effect. $\delta_{f,S}/\delta_{f,R}$ = 40/40; i_t = 0°; C_μ = 0.032; h/D = 0.94; h'/D = 0.67.

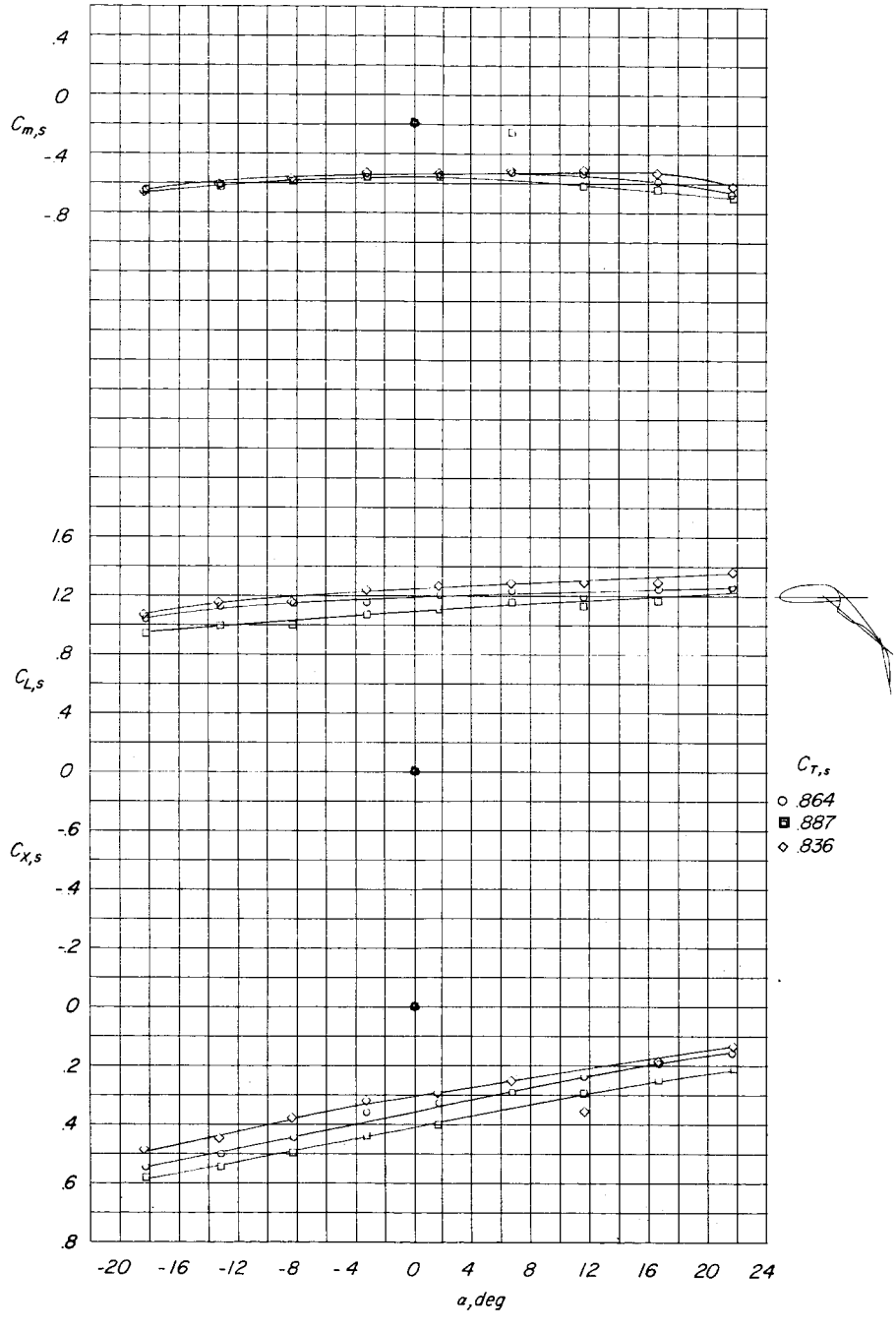

(b) Variation of pitching-moment, lift, and longitudinal-force coefficients with angle of attack.

Figure 25.- Concluded.

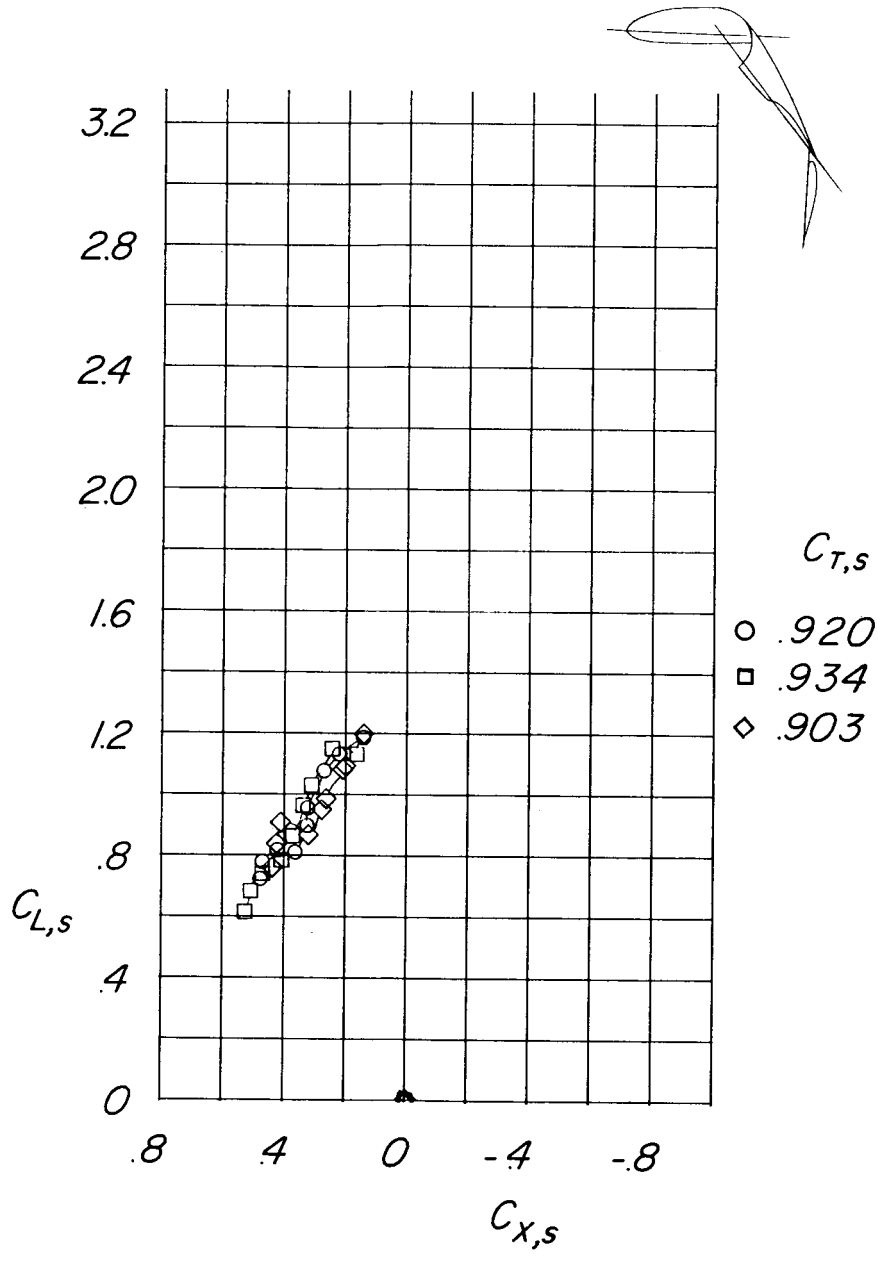

(a) Variation of longitudinal-force coefficient with lift coefficient.

Figure 26.- Effect of variation in thrust coefficient on longitudinal aerodynamic characteristics in the region of ground effect. $\delta_{f,S}/\delta_{f,R}$ = 50/40; i_t = 0°; C_μ = 0.032; h/D = 0.94; h'/D = 0.62.

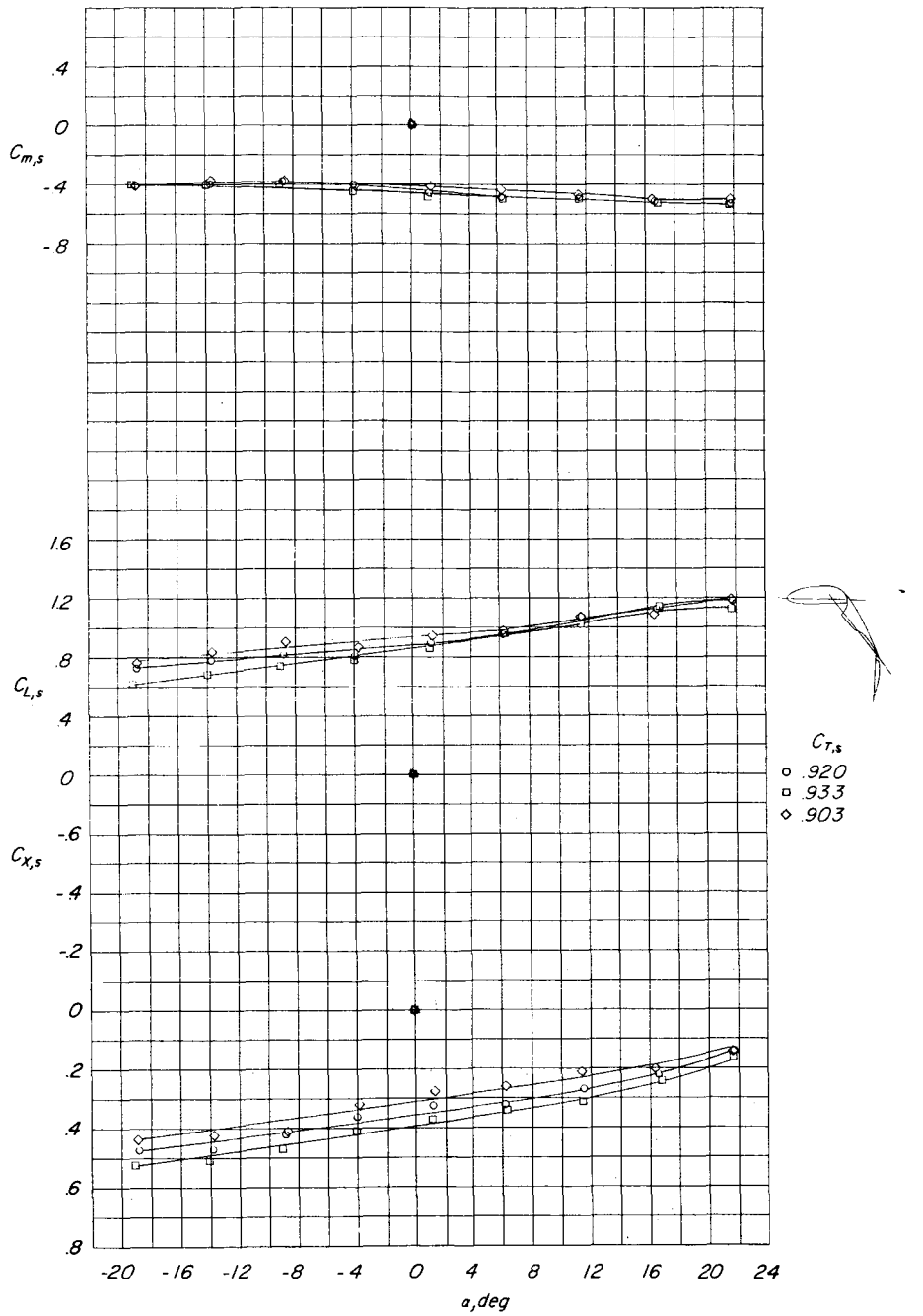

(b) Variation of pitching-moment, lift, and longitudinal-force coefficients with angle of attack.

Figure 26.- Concluded.

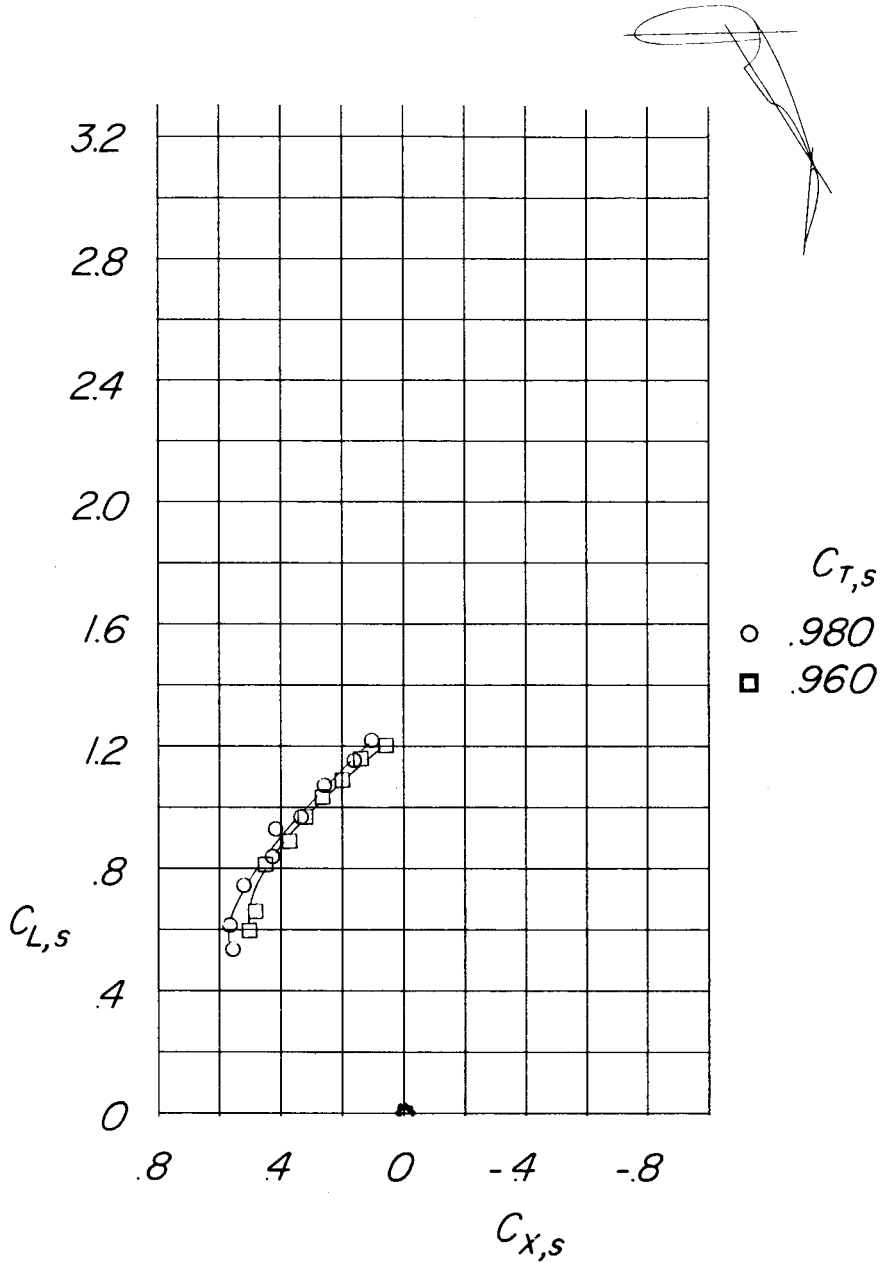

(a) Variation of longitudinal-force coefficient with lift coefficient.

Figure 27.- Effect of variation in thrust coefficient on longitudinal aerodynamic characteristics in the region of ground effect. $\delta_{f,S}/\delta_{f,R}$ = 50/40; i_t = 20°; C_μ = 0.032; h/D = 0.94; h'/D = 0.62.

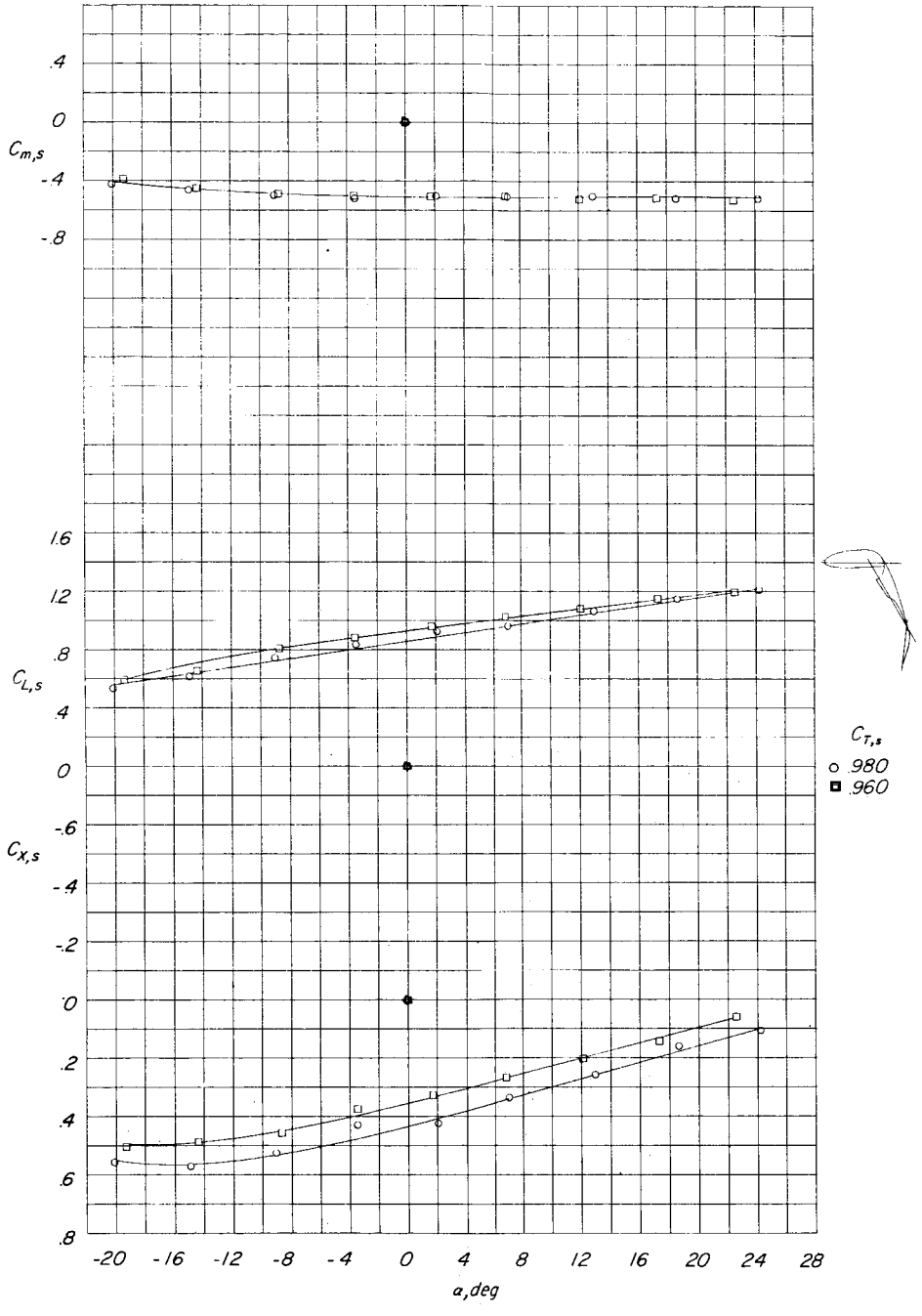

(b) Variation of pitching-moment, lift, and longitudinal-force coefficients with angle of attack.

Figure 27.- Concluded.

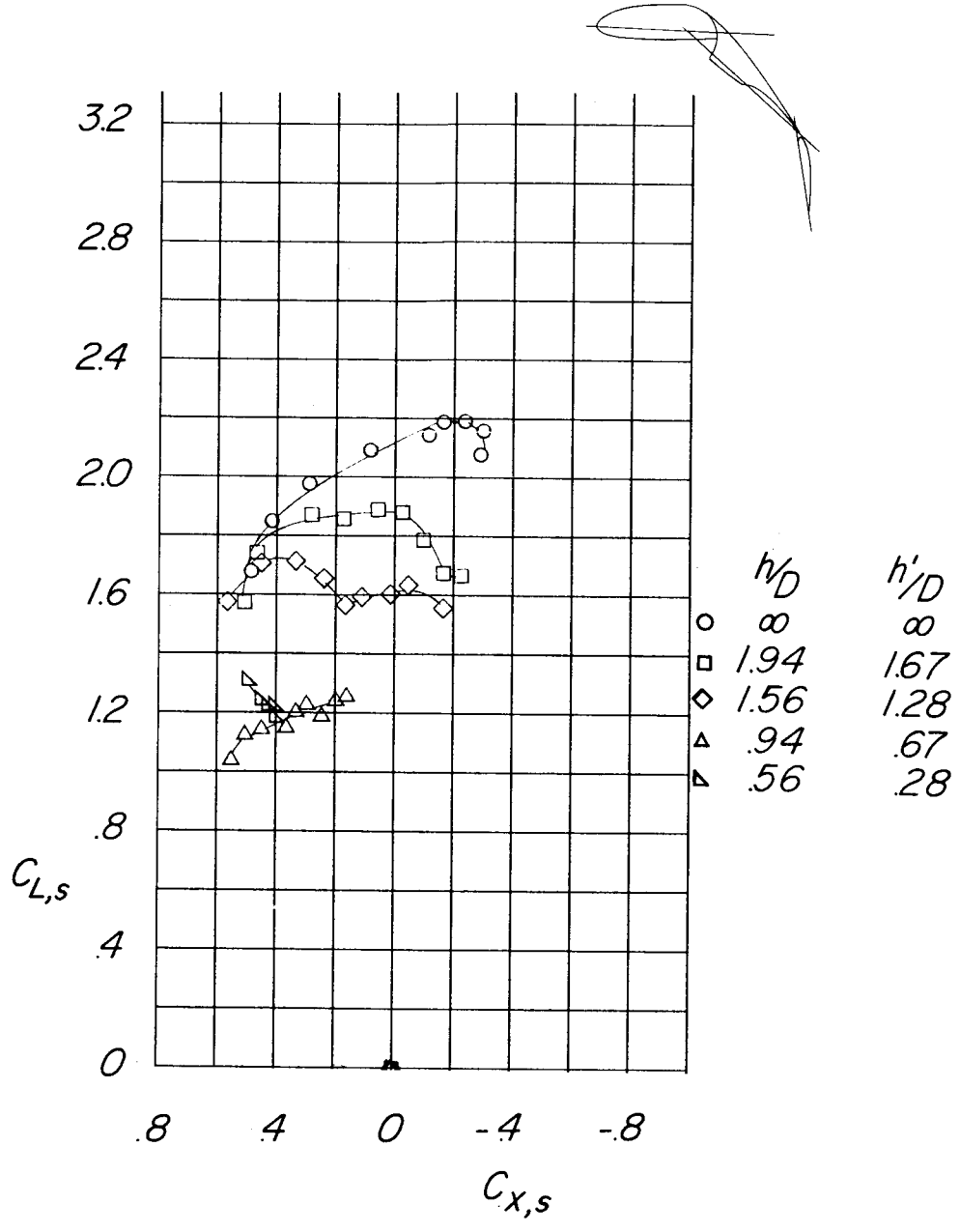

(a) Variation of longitudinal-force coefficient with lift coefficient.

Figure 28.- Effect of height above ground on longitudinal aerodynamic characteristics. $\delta_{f,S}/\delta_{f,R} = 40/40$; $C_{T,s} = 0.864$; $i_t = 0^o$; $C_\mu = 0.032$.

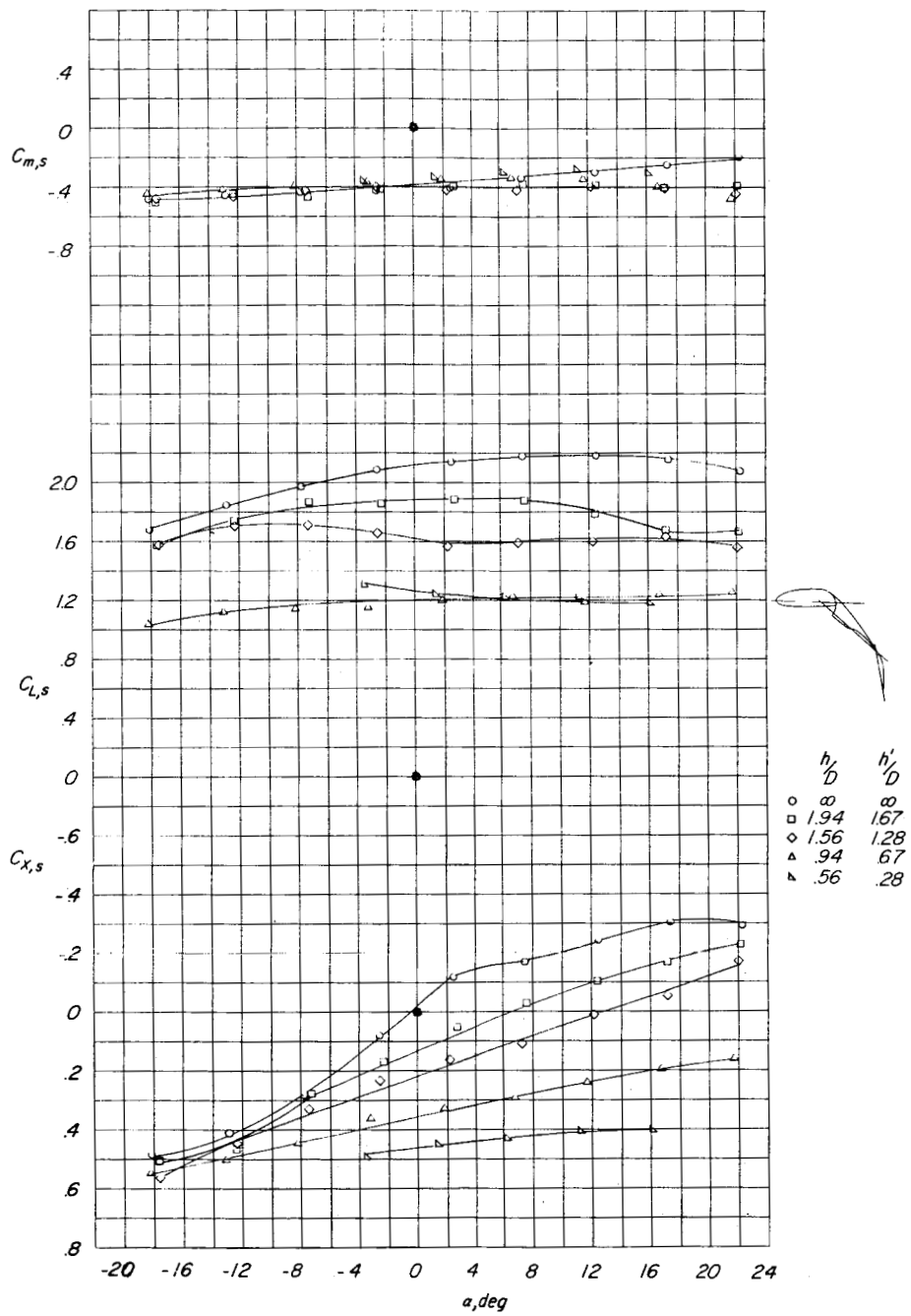

(b) Variation of pitching-moment, lift, and longitudinal-force coefficients with angle of attack.

Figure 28.- Concluded.

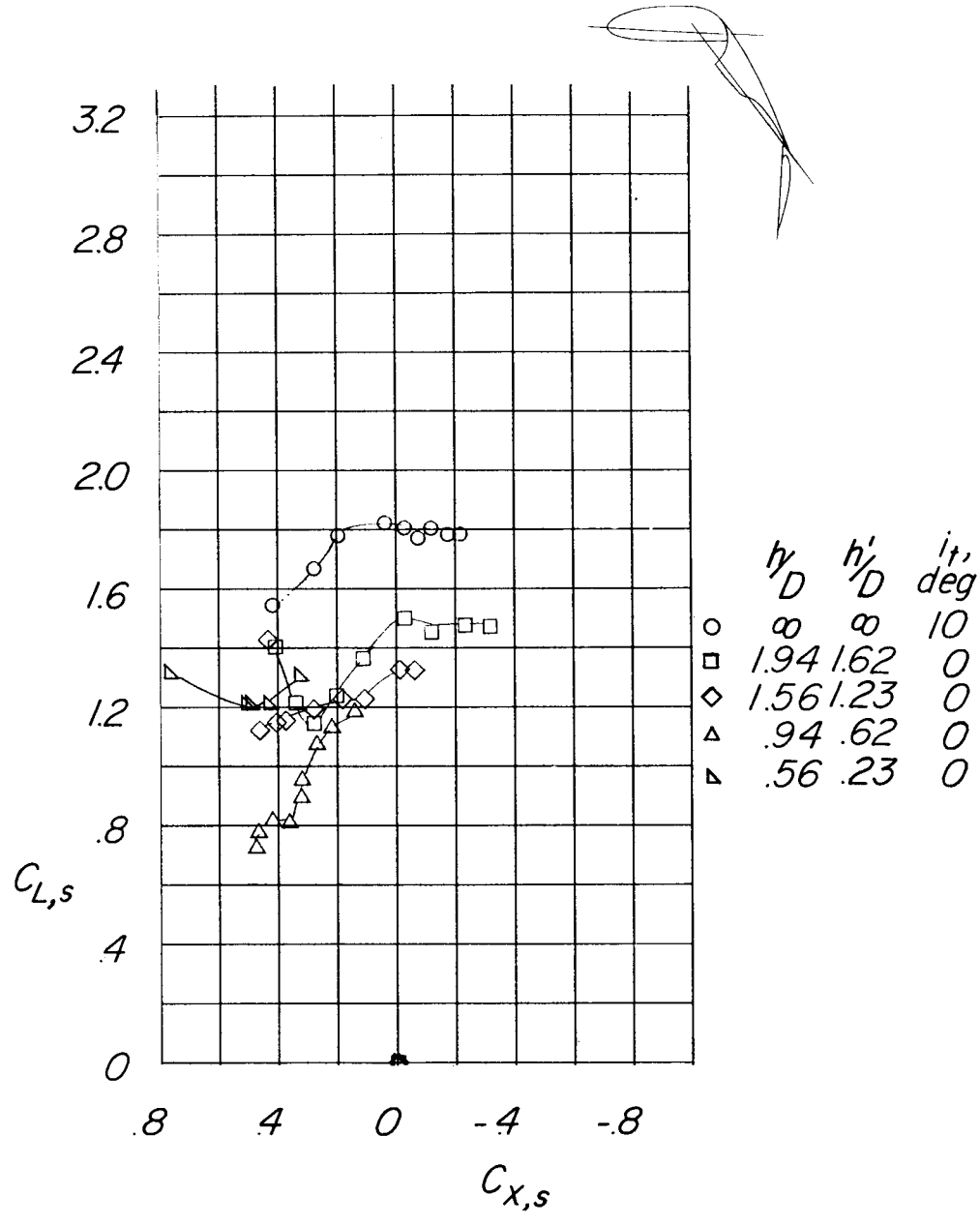

(a) Variation of longitudinal-force coefficient with lift coefficient.

Figure 29.- Effect of height above ground on longitudinal aerodynamic characteristics. $\delta_{f,S}/\delta_{f,R} = 50/40$; $C_{T,s} = 0.920$; $C_{\mu} = 0.032$.

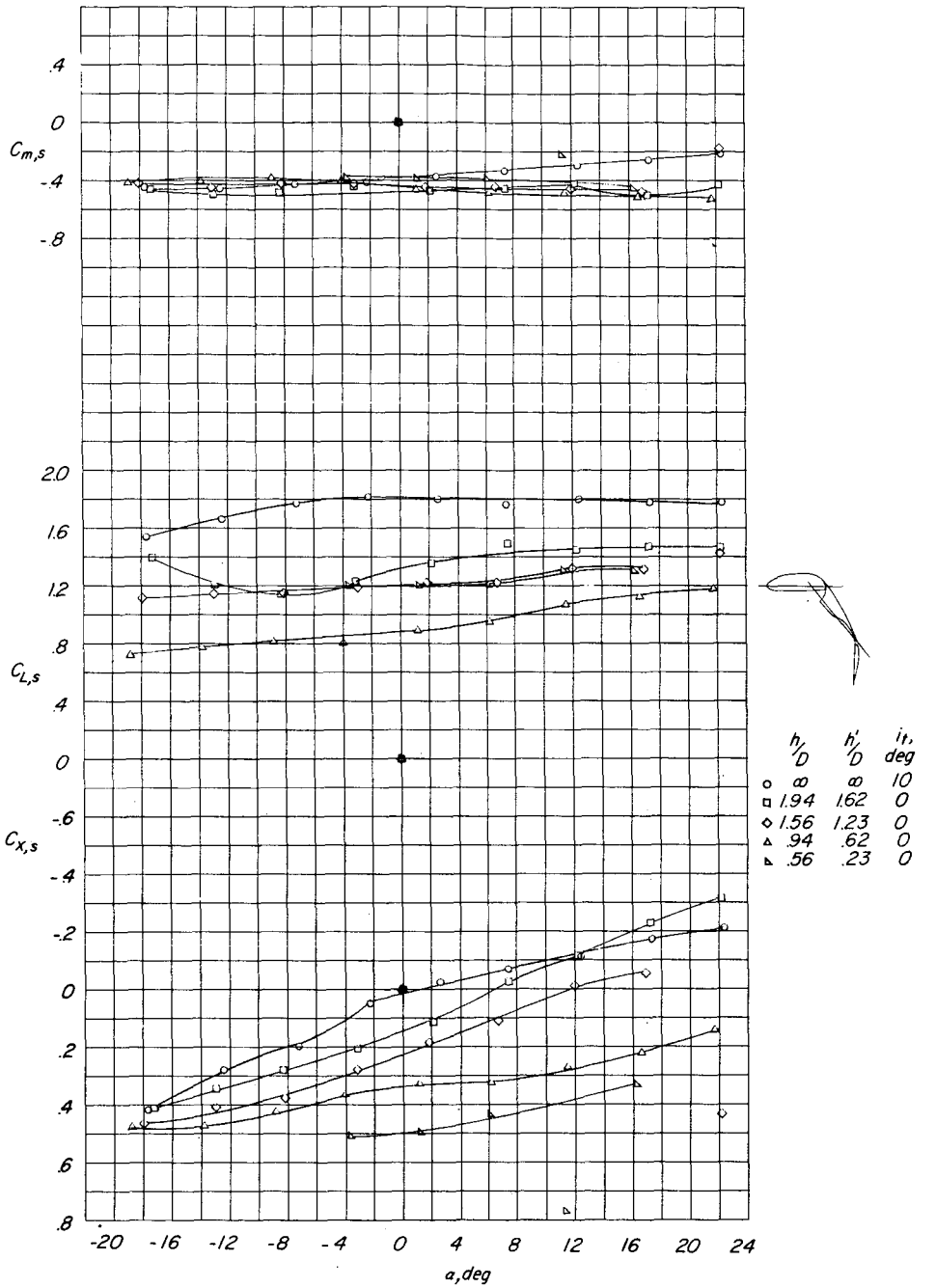

(b) Variation of pitching-moment, lift, and longitudinal-force coefficients with angle of attack.

Figure 29.- Concluded.

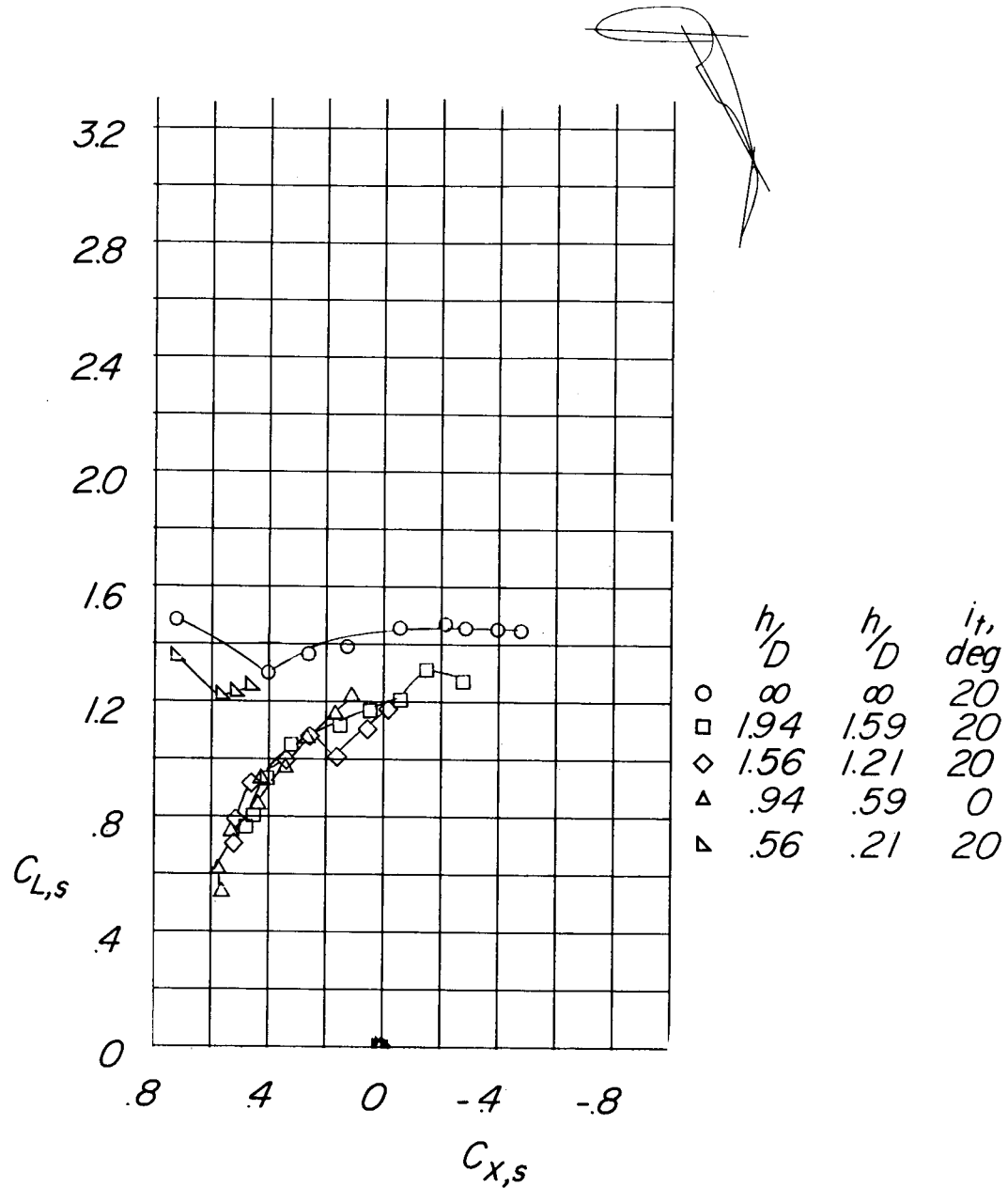

(a) Variation of longitudinal-force coefficient with lift coefficient.

Figure 30.- Effect of height above ground on longitudinal aerodynamic characteristics. $\delta_{f,S}/\delta_{f,R} = 60/40$; $C_{T,s} = 0.980$; $C_{\mu} = 0.032$.

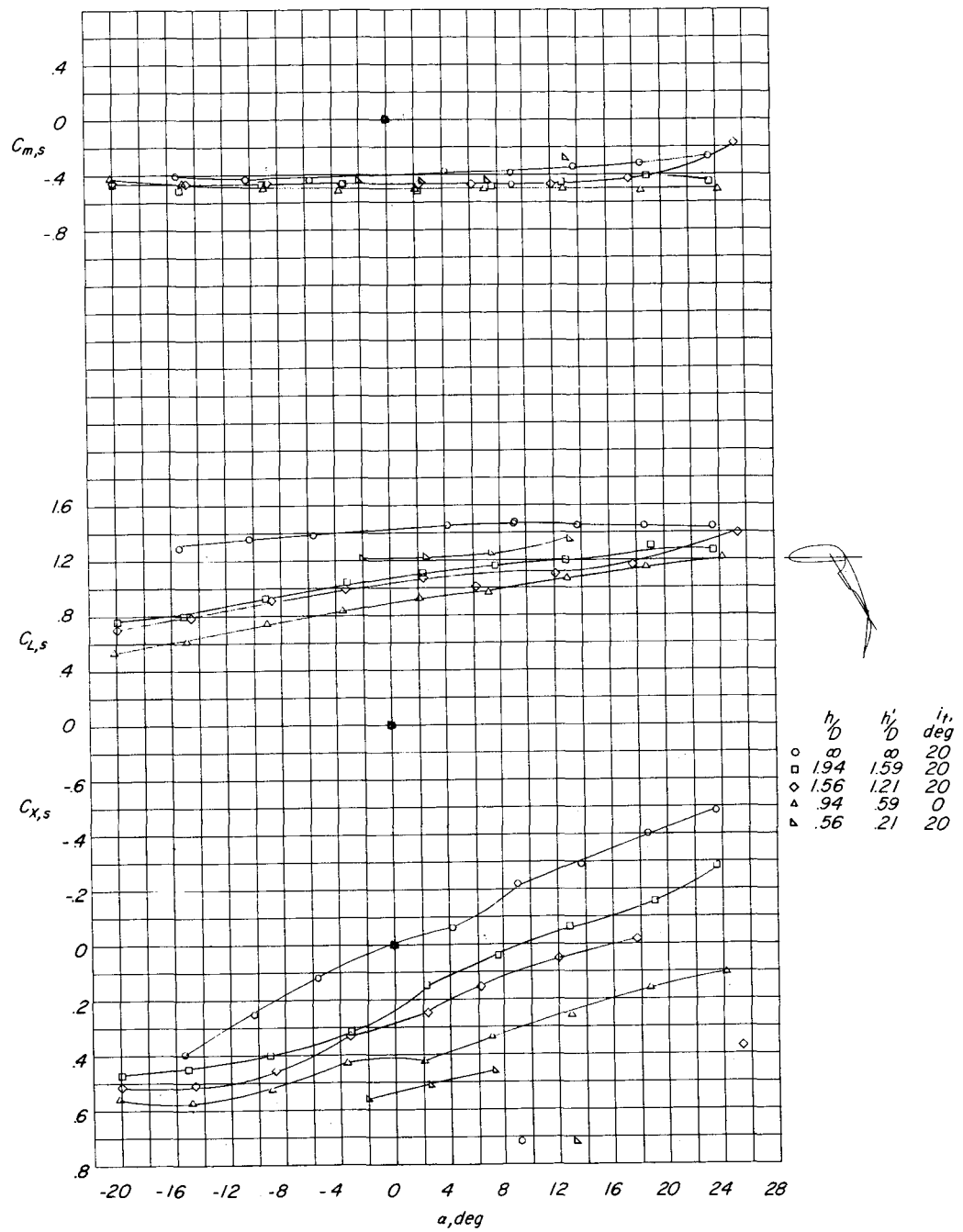

(b) Variation of pitching-moment, lift, and longitudinal-force coefficients with angle of attack.

Figure 30.- Concluded.

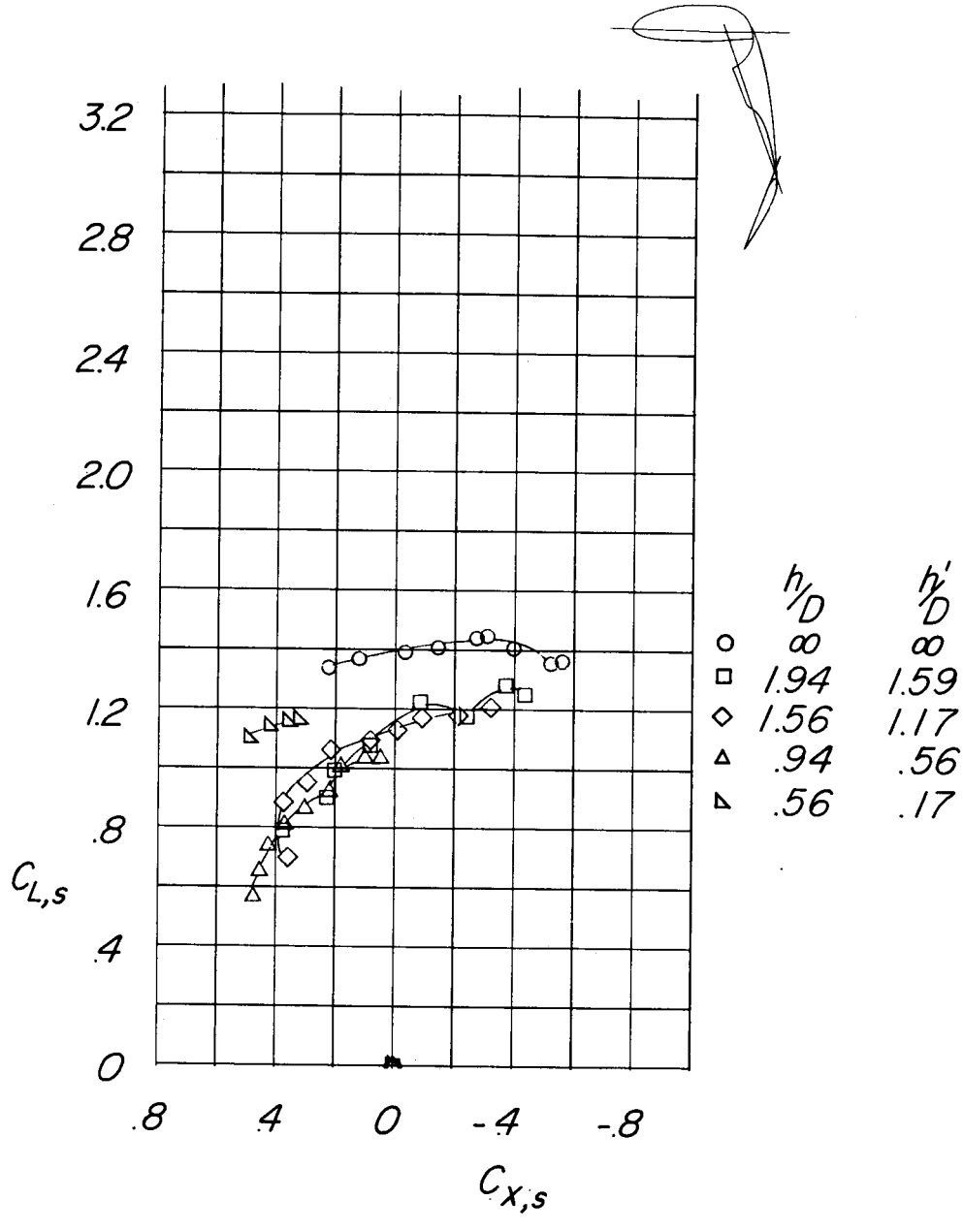

(a) Variation of longitudinal-force coefficient with lift coefficient.

Figure 31.- Effect of height above ground on longitudinal aerodynamic characteristics. $\delta_{f,S}/\delta_{f,R} = 70/40$; $C_{T,s} = 0.980$; $i_t = 20^\circ$; $C_\mu = 0.032$.

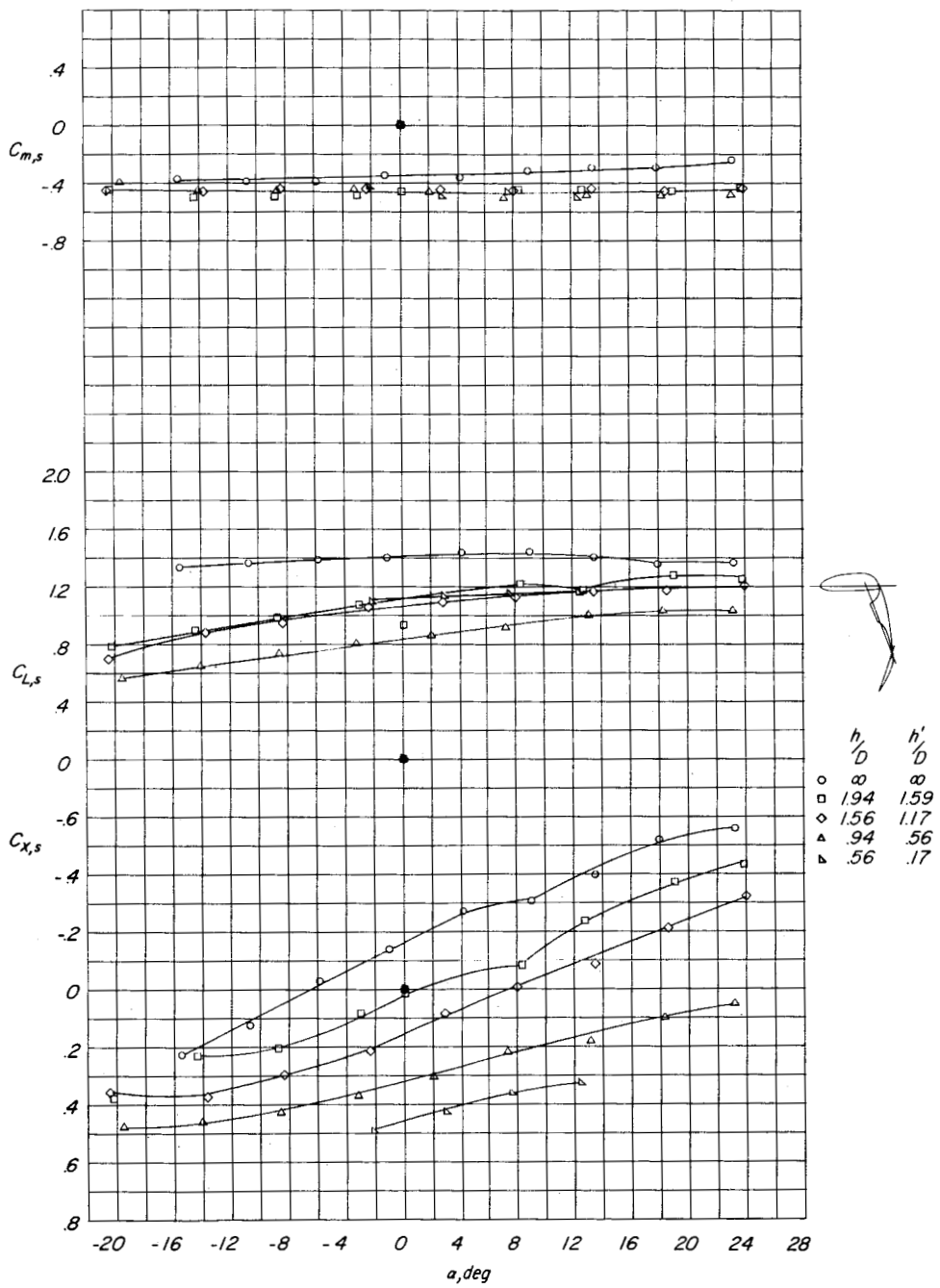

(b) Variation of pitching-moment, lift, and longitudinal-force coefficients with angle of attack.

Figure 31.- Concluded.

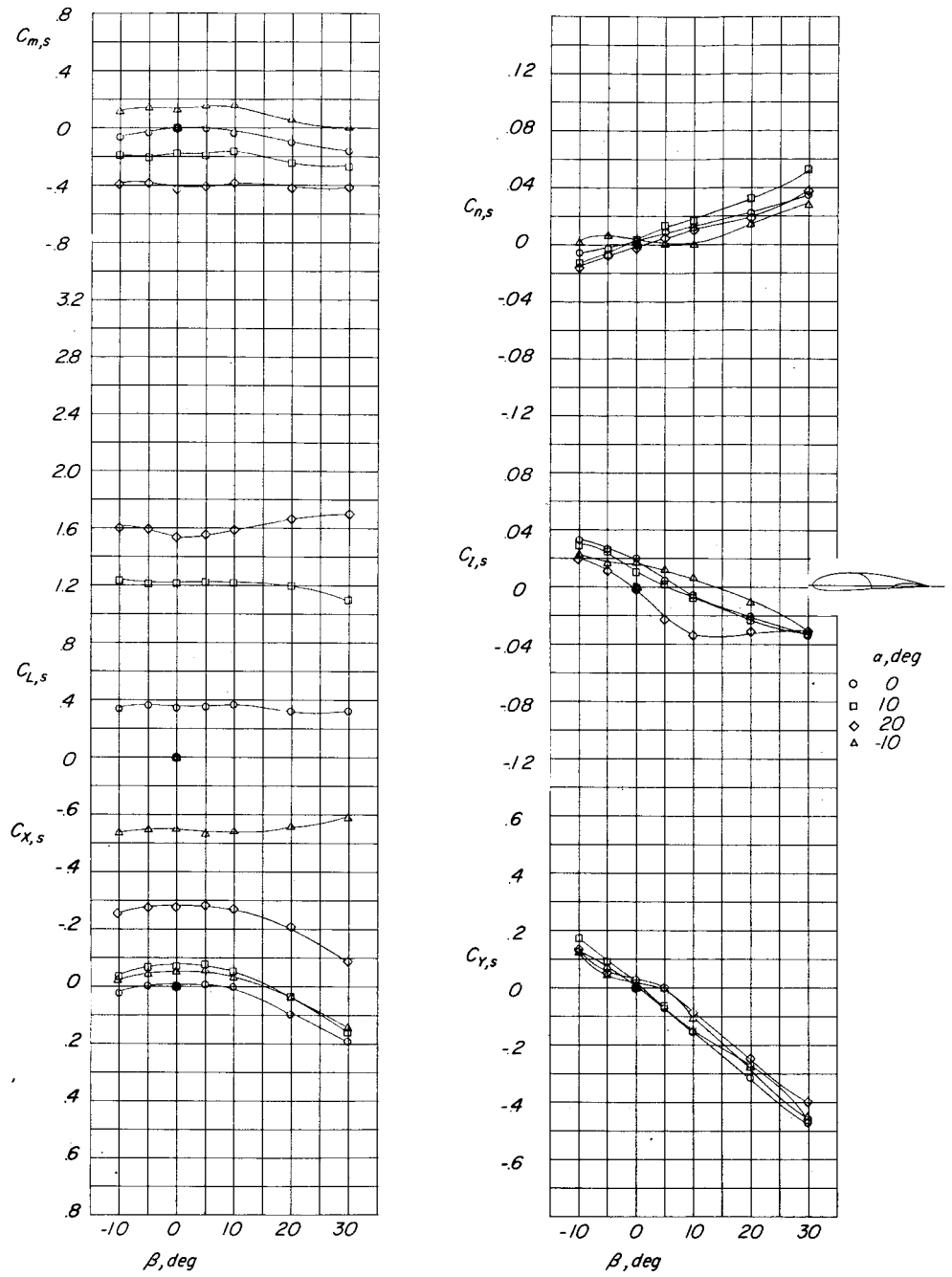

(a) $\delta_{f,S}/\delta_{f,R} = 0/0$; $C_{T,s} = 0$ (propellers off); $i_t = 0^o$; $C_\mu = 0$.

Figure 32.- Effect of angle of attack on lateral aerodynamic characteristics out of the region of ground effect.

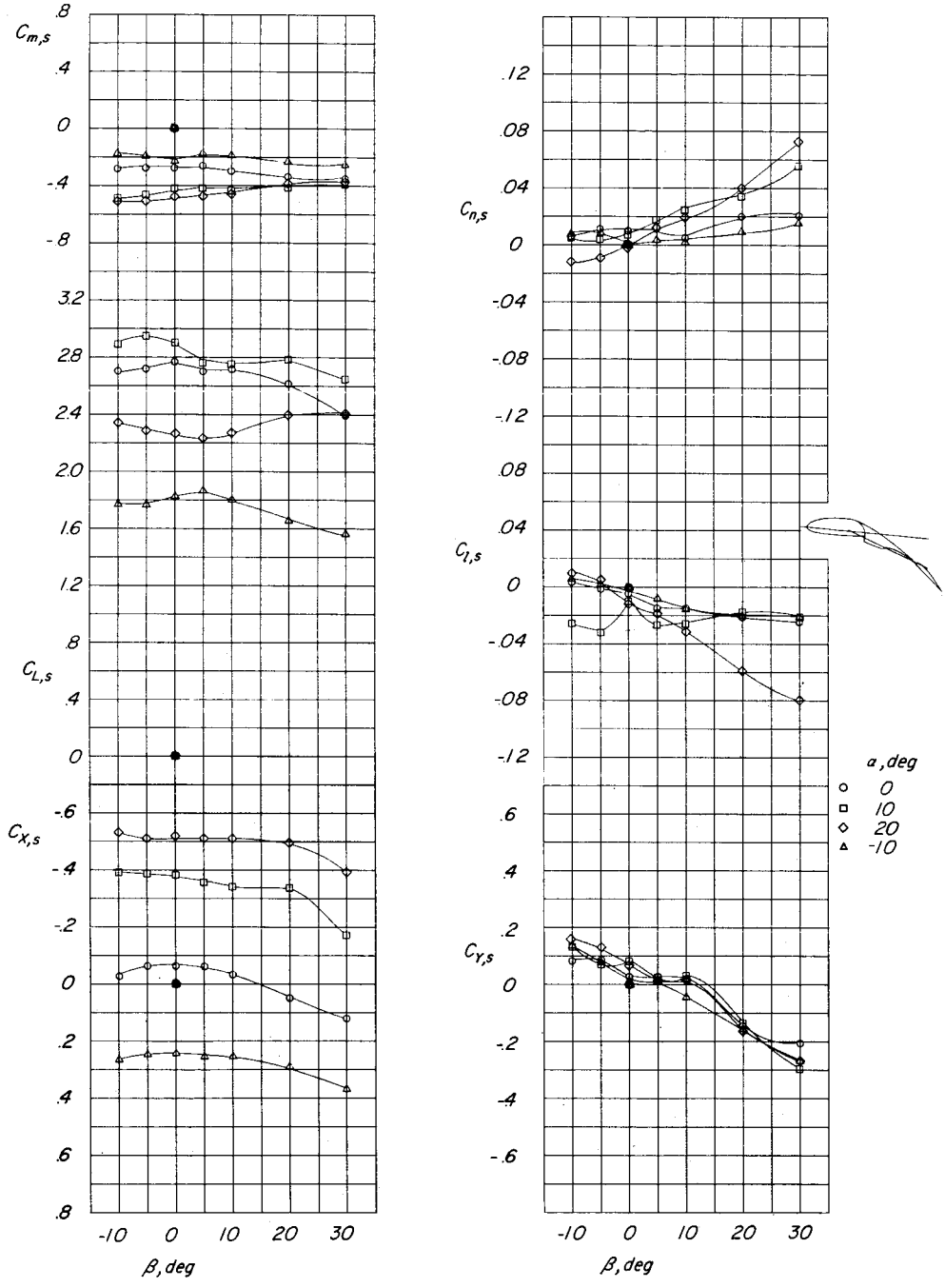

(b) $\delta_{f,S}/\delta_{f,R}$ = 20/20; $C_{T,s}$ = 0.325; i_t = 0°; C_μ = 0.062.

Figure 32.- Continued.

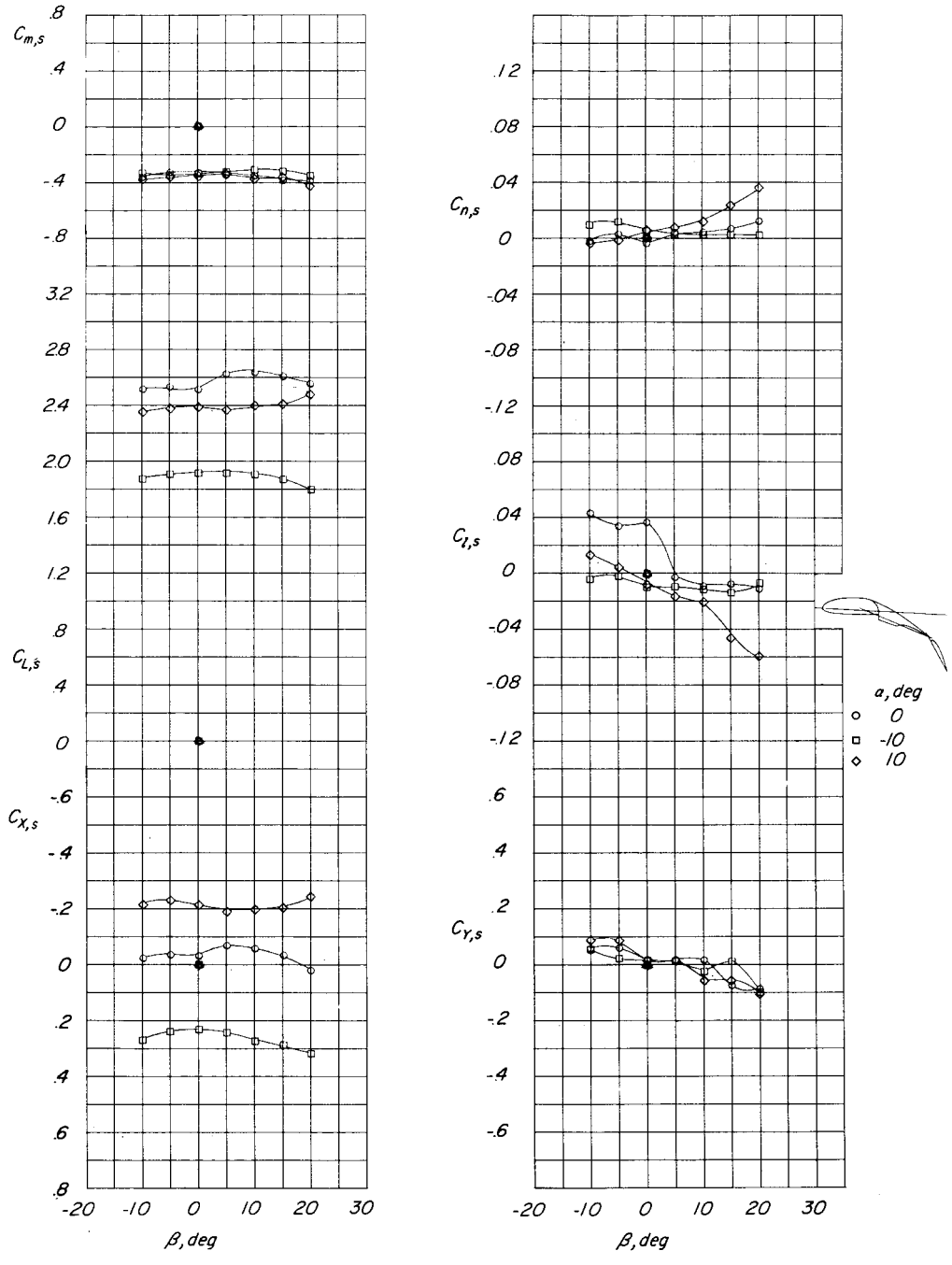

(c) $\delta_{f,S}/\delta_{f,R}$ = 20/40; $C_{T,s}$ = 0.510; i_t = 0°; C_μ = 0.

Figure 32.- Continued.

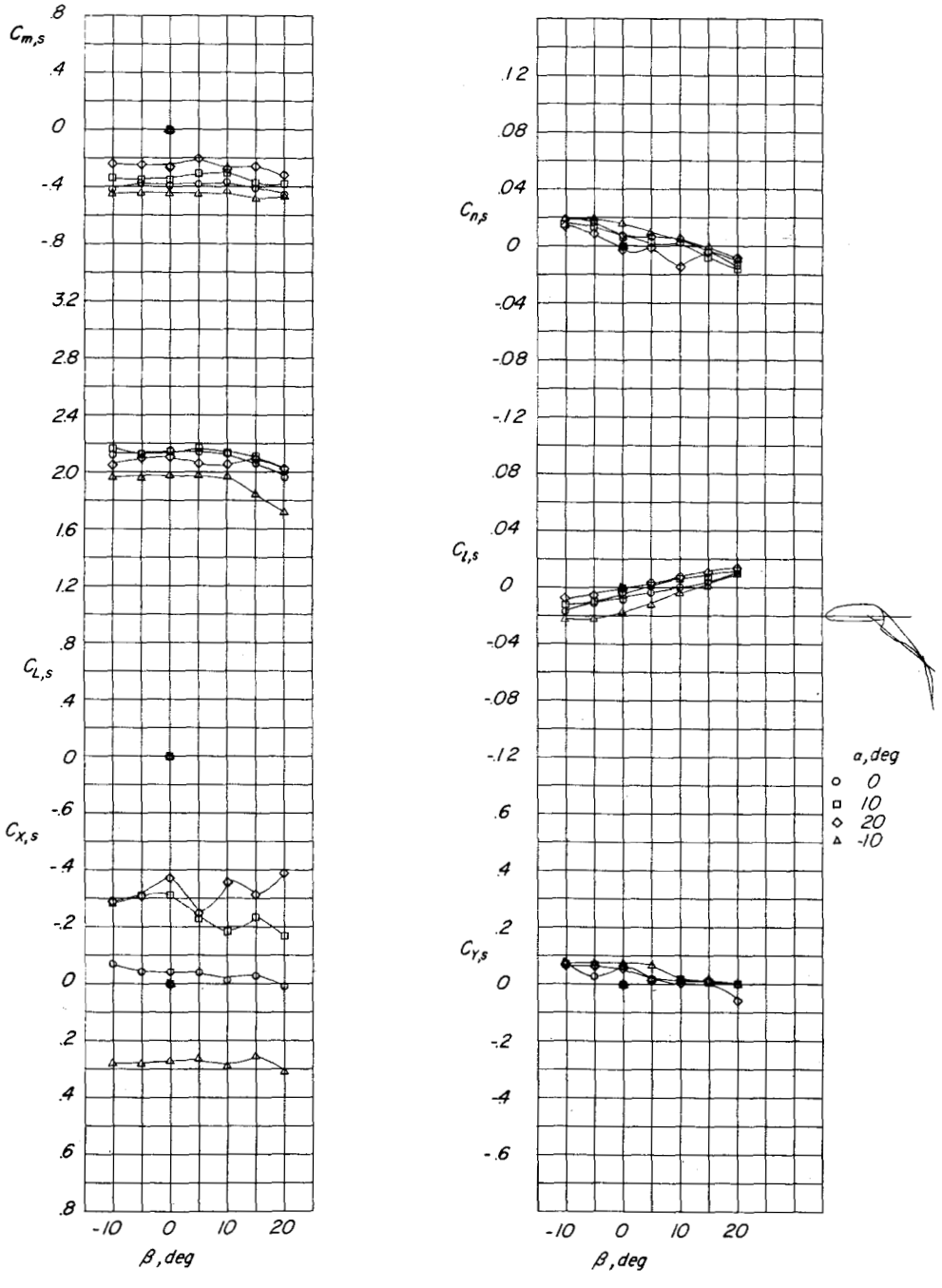

(d) $\delta_{f,S}/\delta_{f,R}$ = 40/40; $C_{T,s}$ = 0.864; i_t = 0°; C_μ = 0.062.

Figure 32.- Continued.

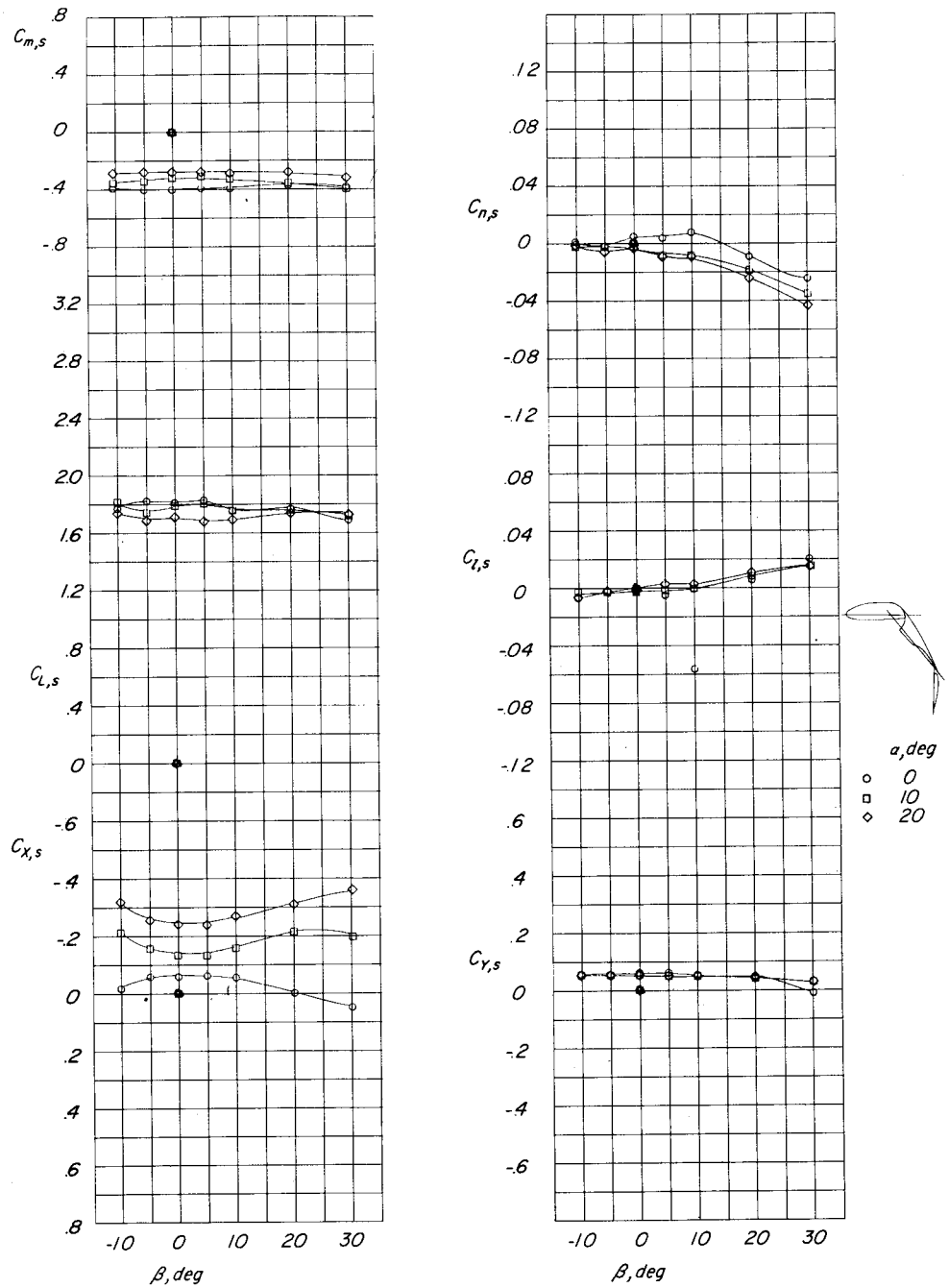

(e) $\delta_{f,S}/\delta_{f,R}$ = 50/40; $C_{T,s}$ = 0.920; i_t = 20°; C_μ = 0.062.

Figure 32.- Continued.

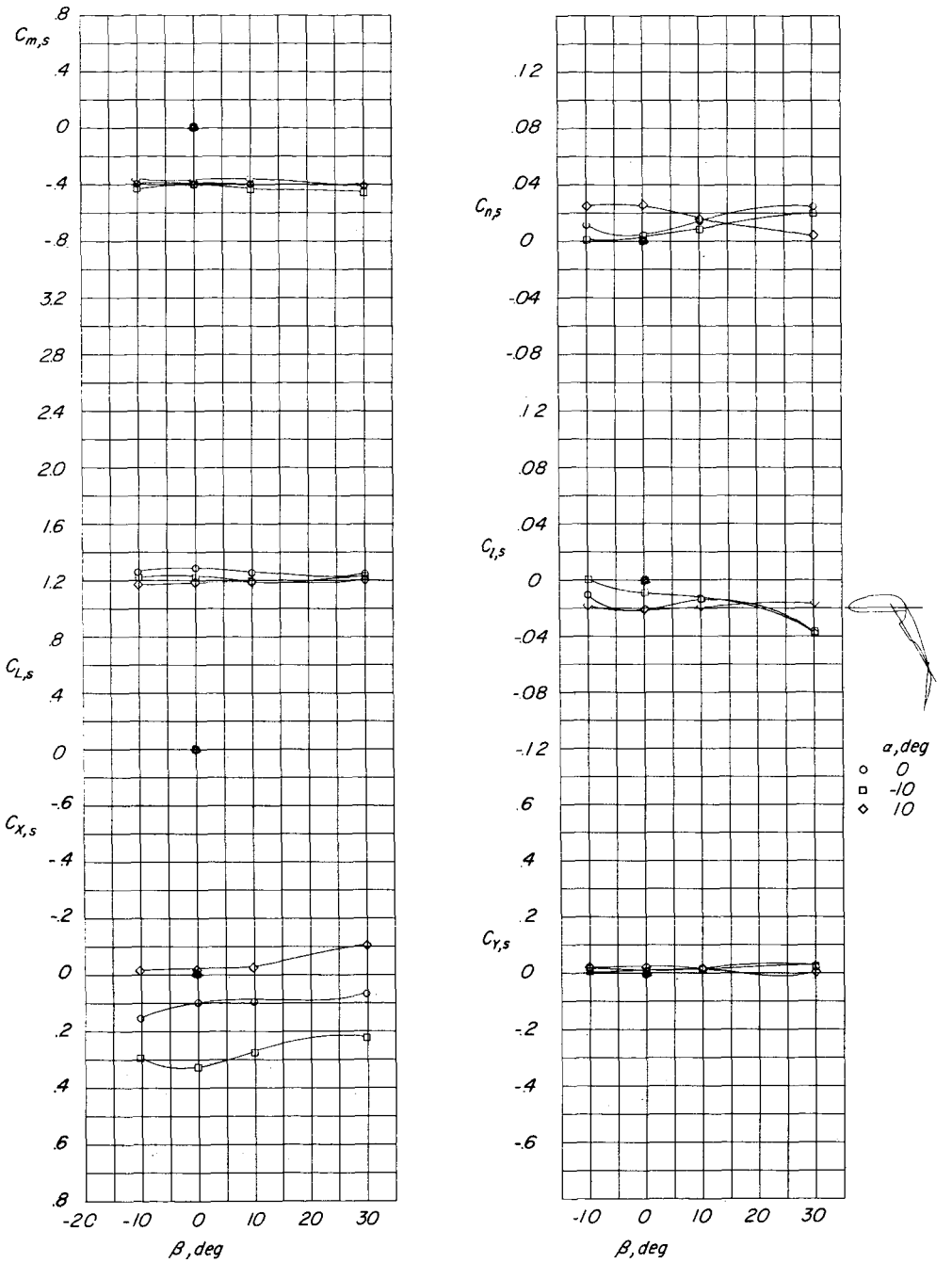

(f) $\delta_{f,S}/\delta_{f,R}$ = 60/40; $C_{T,s}$ = 0.980; i_t = 10°; C_μ = 0.

Figure 32.- Continued.

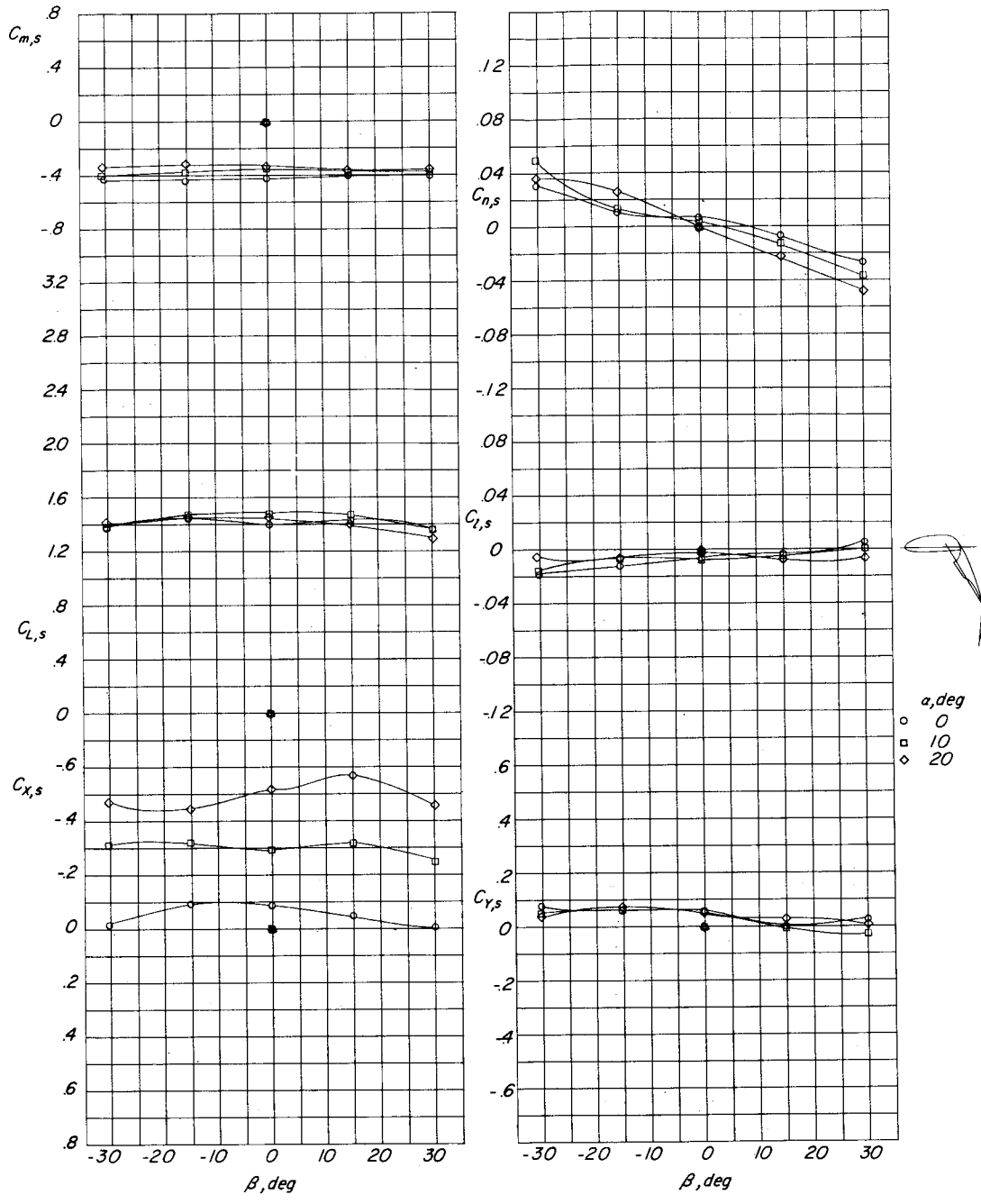

(g) $\delta_{f,S}/\delta_{f,R}$ = 60/40; $C_{T,s}$ = 0.980; i_t = 20°; C_μ = 0.062.

Figure 32.- Continued.

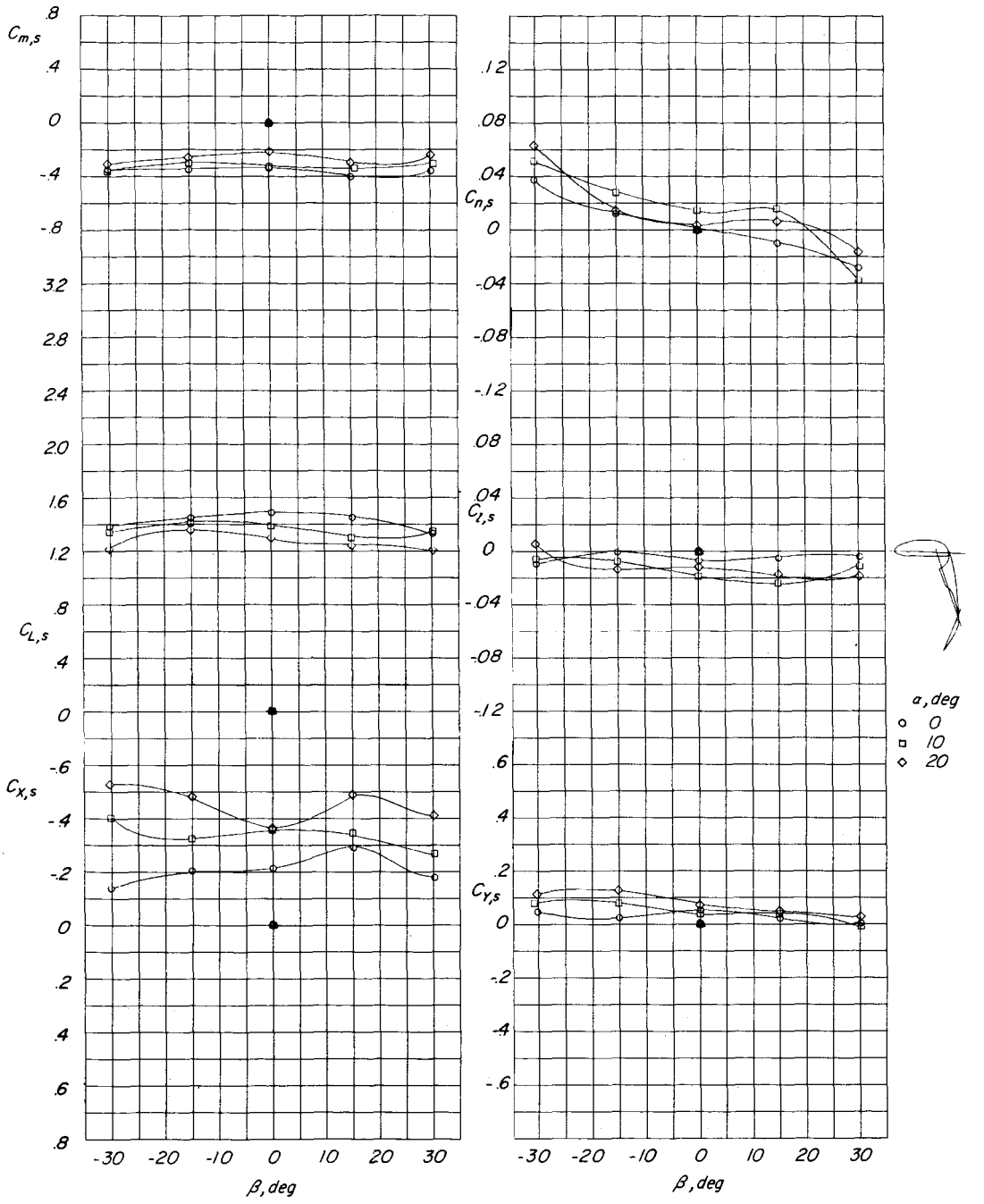

(h) $\delta_{f,S}/\delta_{f,R}$ = 70/40; $C_{T,s}$ = 0.980; i_t = 20°; C_μ = 0.062.

Figure 32.- Concluded.

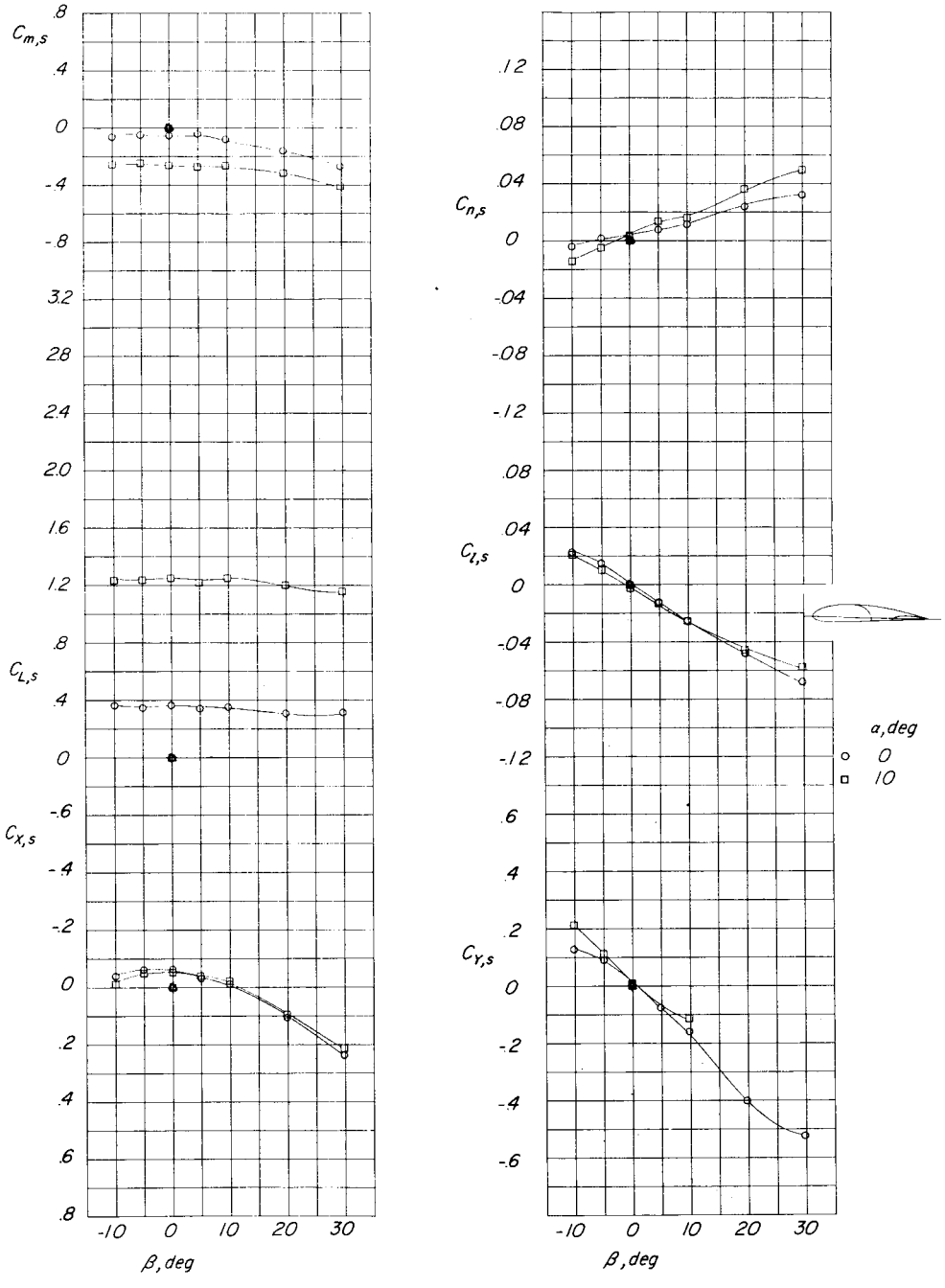

Figure 33.- Effect of retracted flaps and power-off condition on lateral aerodynamic characteristics in the region of ground effect. $\delta_{f,S}/\delta_{f,R} = 0/0$; $i_t = 0^o$; $C_\mu = 0$; $C_{T,s} = 0$.

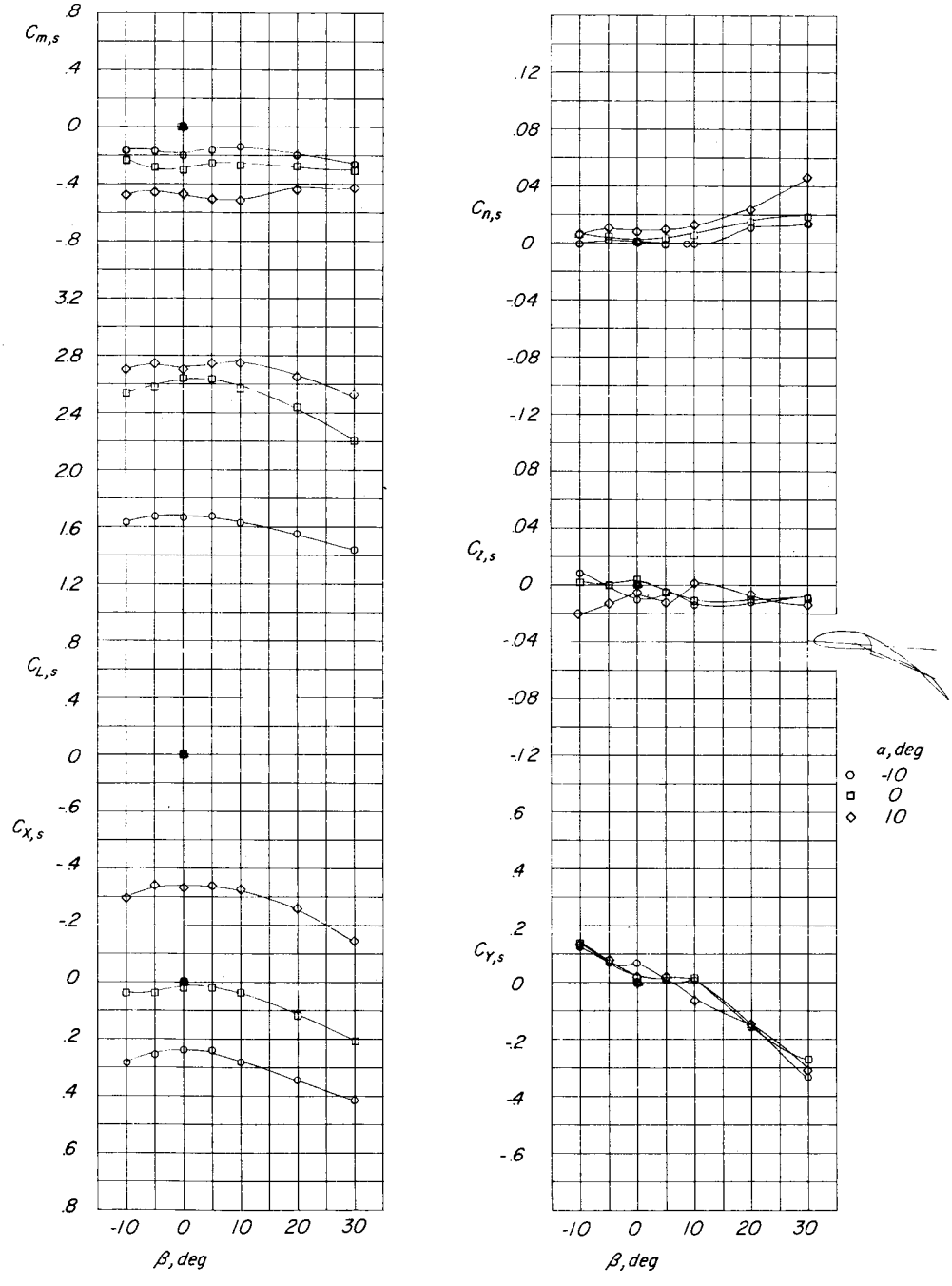

(a) h/D = 1.94; h'/D = 1.87.

Figure 34.- Effect of height above ground. $\delta_{f,S}/\delta_{f,R}$ = 20/20; $C_{T,s}$ = 0.325; i_t = 0°; C_μ = 0.062.

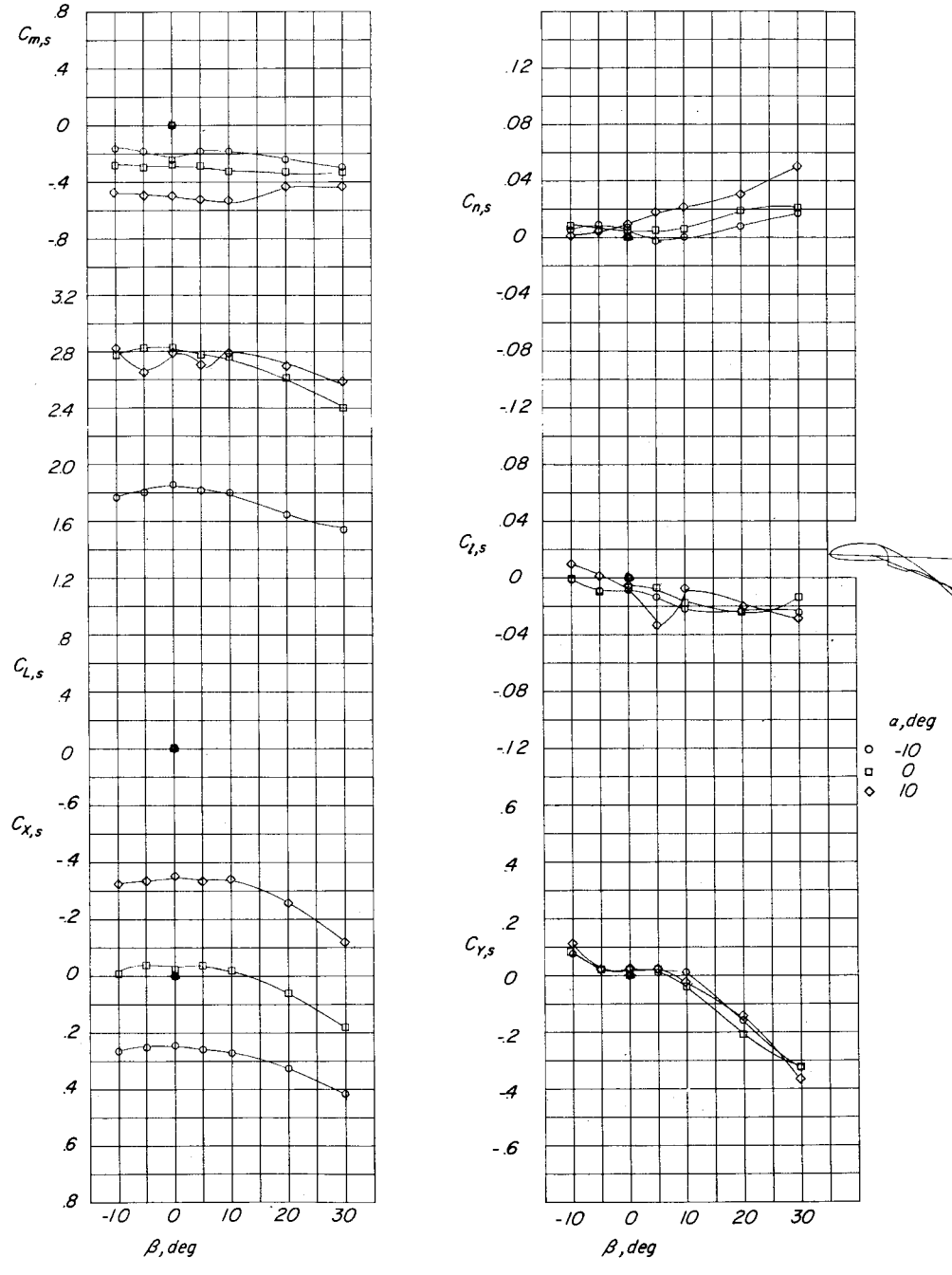

(b) h/D = 1.06; h'/D = 1.48.

Figure 34.- Continued.

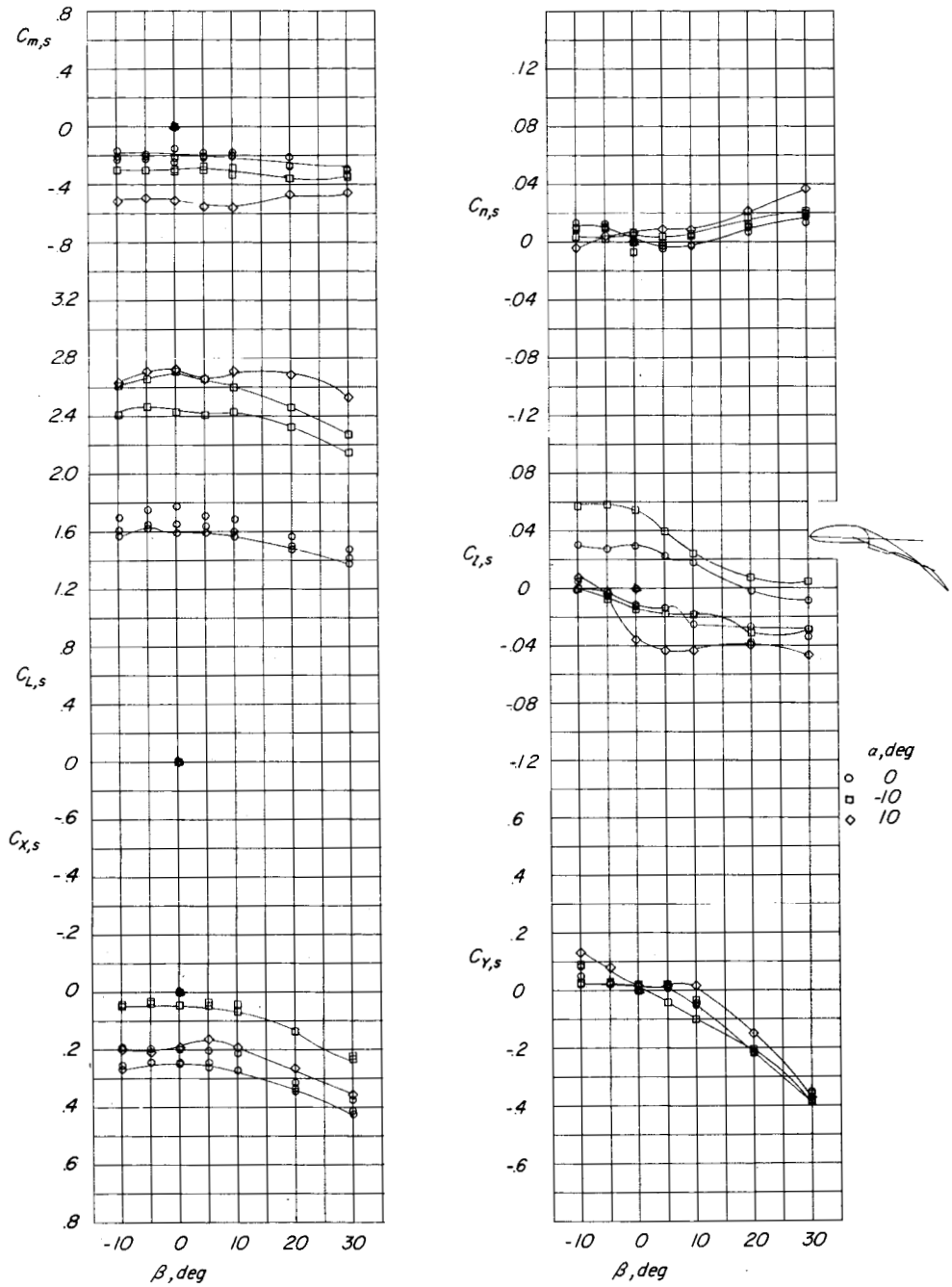

(c) h/D = 0.94; h'/D = 0.87.

Figure 34.- Continued.

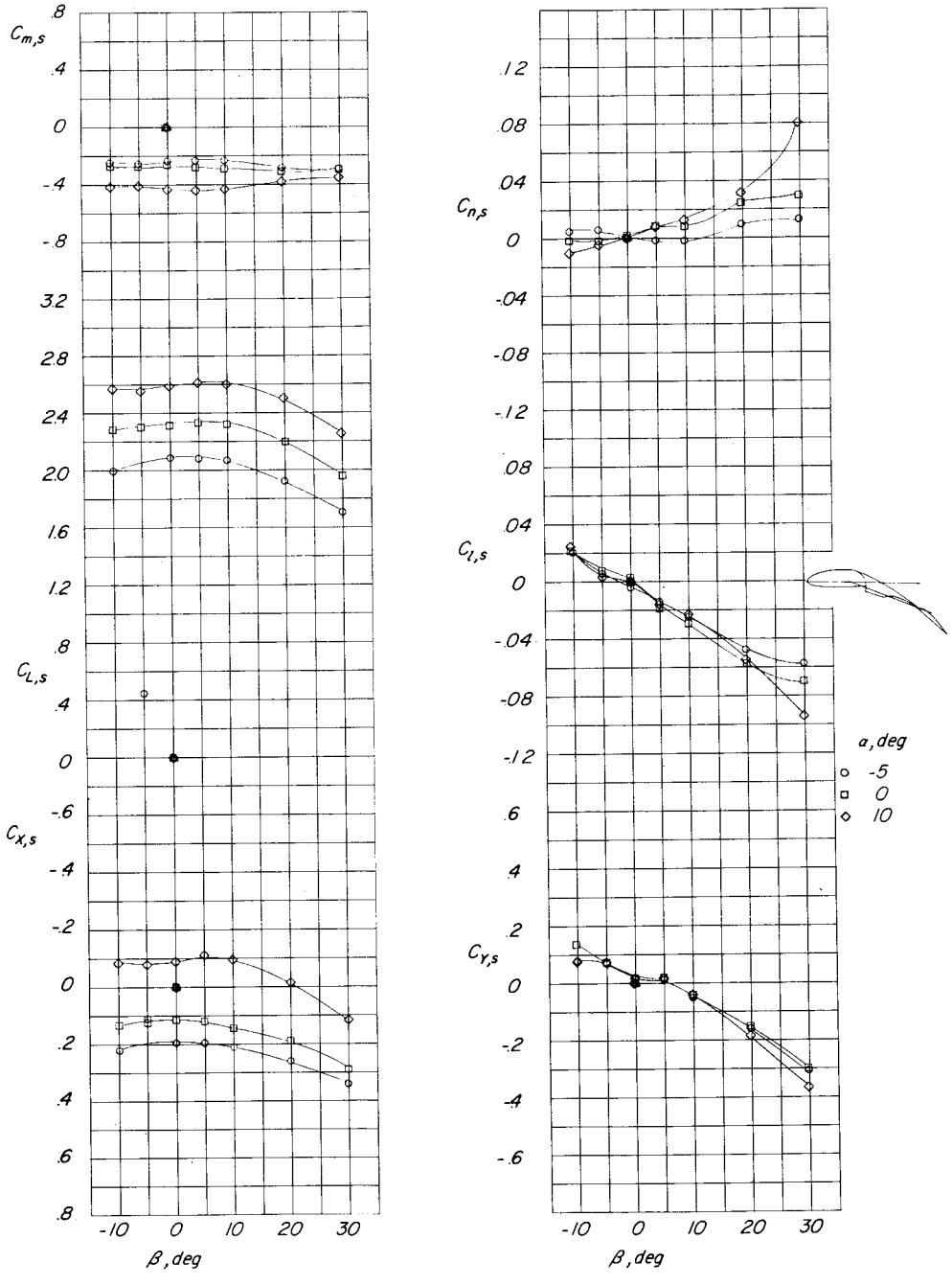

(d) h/D = 0.56; h'/D = 0.48.

Figure 34.- Concluded.

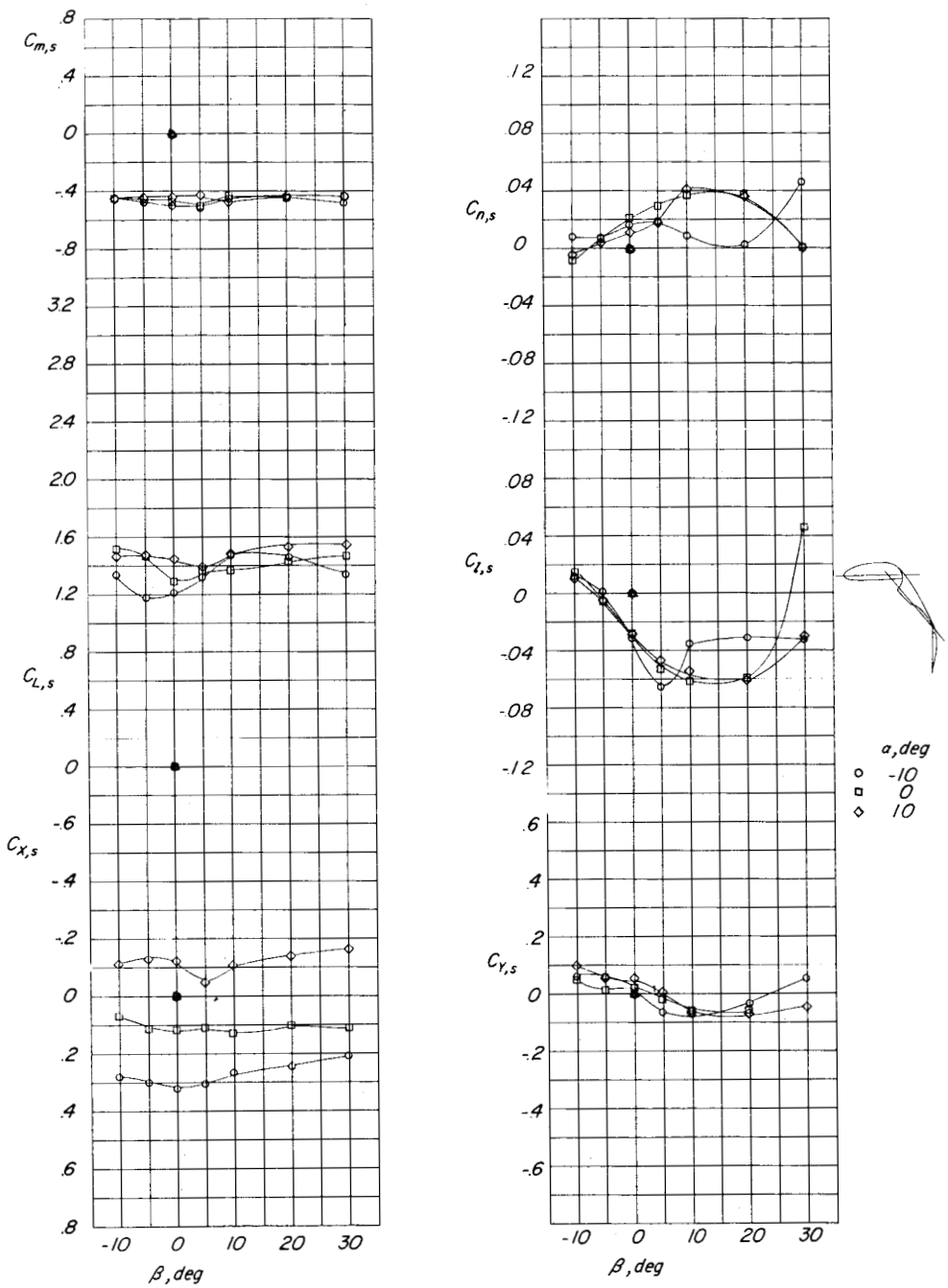

(a) $C_{T,s}$ = 0.921; h/D = 1.94; h'/D = 1.62.

Figure 35.- Effect of height above ground on lateral aerodynamic characteristics. $\delta_{f,S}/\delta_{f,R}$ = 50/40; i_t = 0°; C_μ = 0.062.

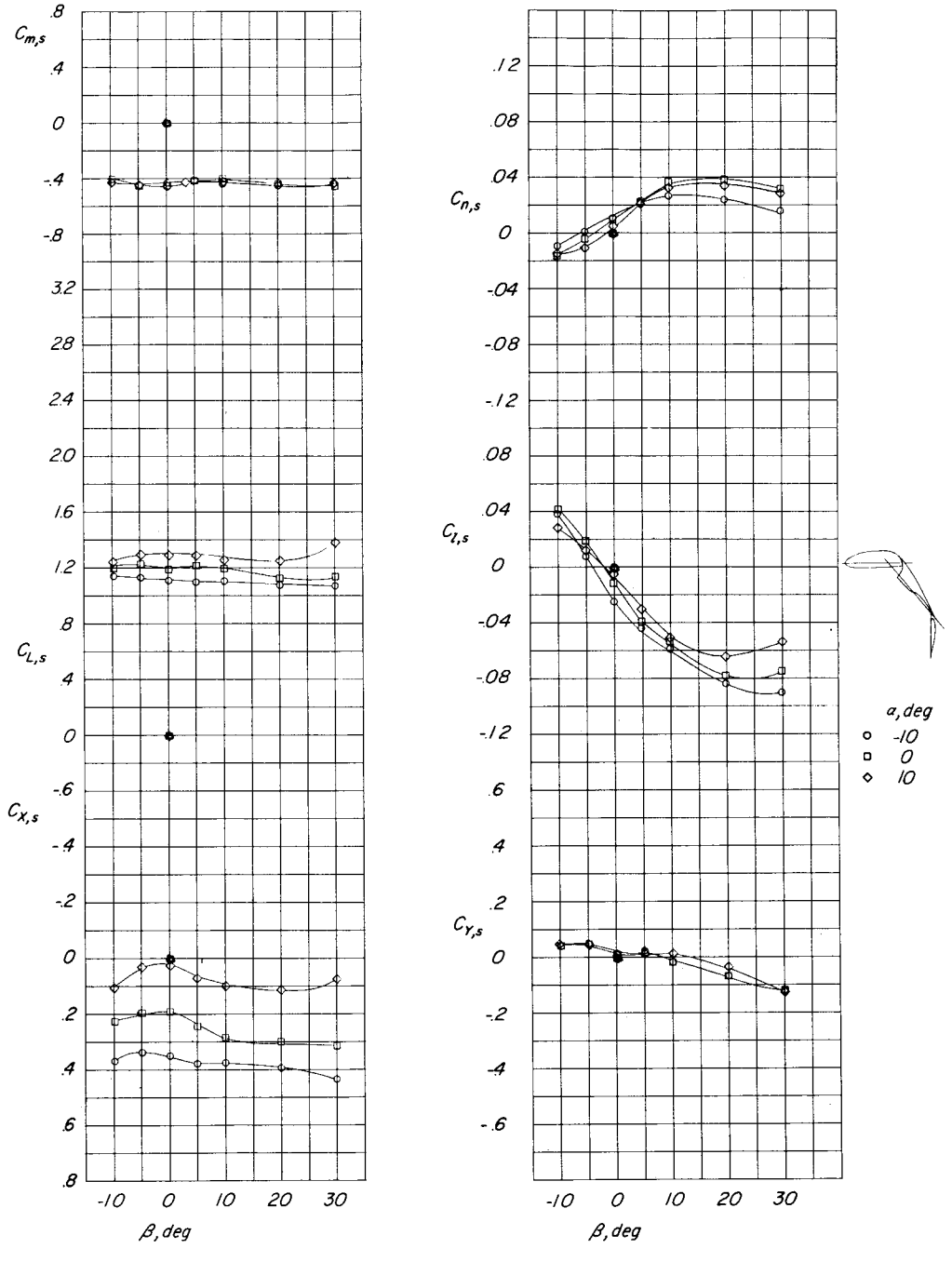

(b) $C_{T,s}$ = 0.920; h/D = 1.56; h'/D = 1.23.

Figure 35.- Continued.

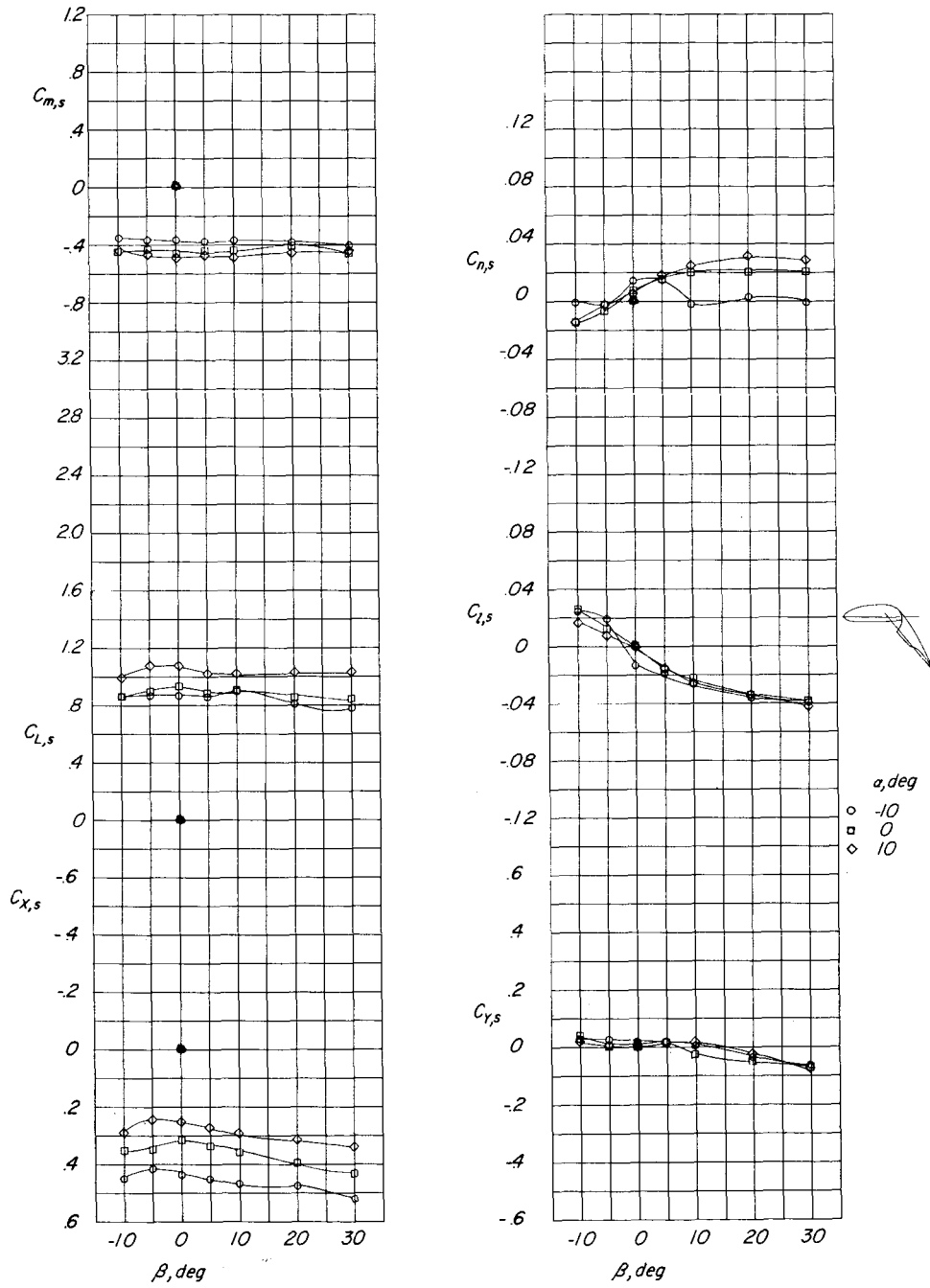

(c) $C_{T,s}$ = 0.920; h/D = 0.94; h'/D = 0.62.

Figure 35.- Continued.

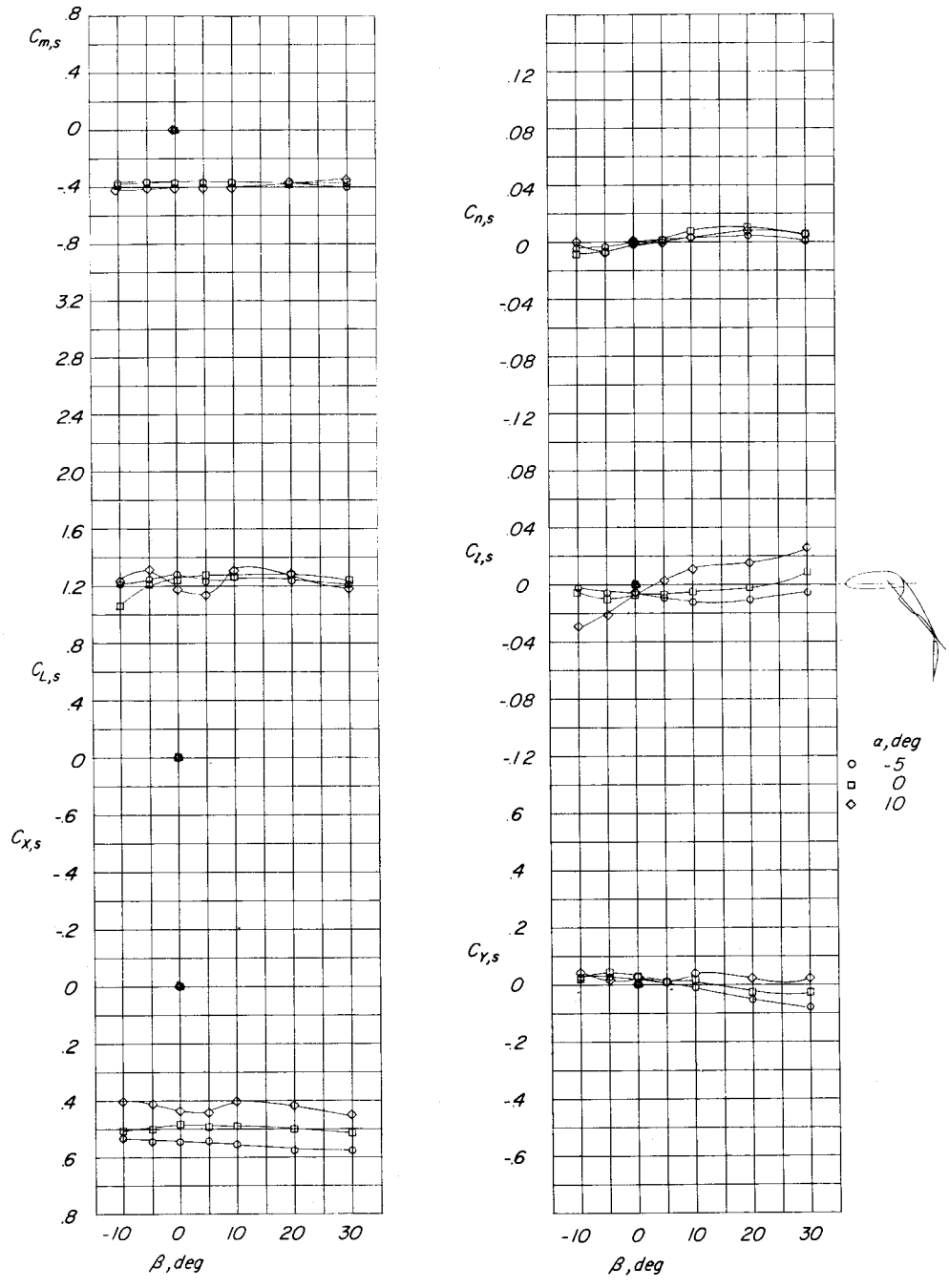

(d) $C_{T,s}$ = 0.920; h/D = 0.56; h'/D = 0.23.

Figure 35.- Concluded.

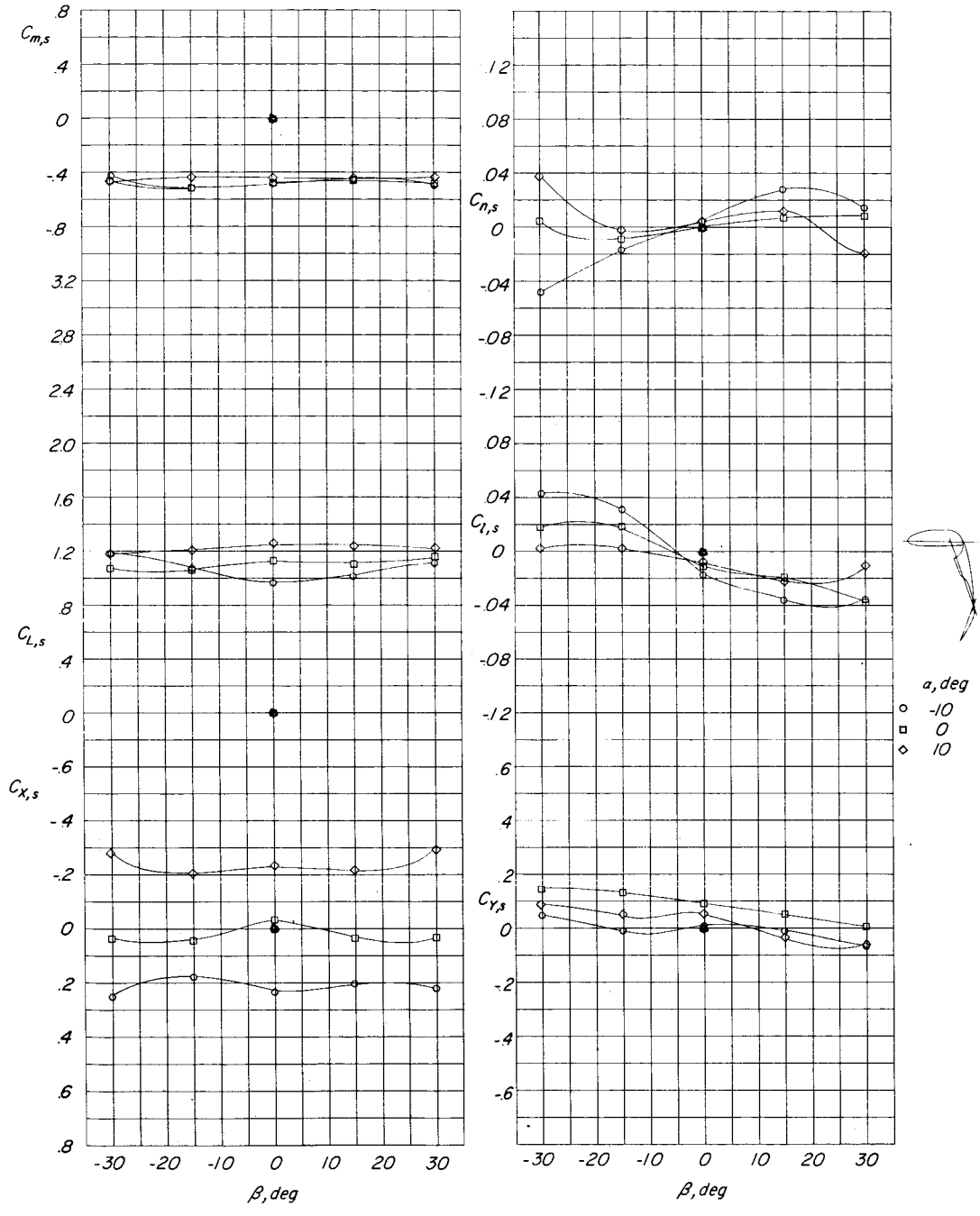

(a) $C_{T,s}$ = 0.980; h/D = 1.94; h'/D = 1.56.

Figure 36.- Effect of height above ground on lateral aerodynamic characteristics. $\delta_{f,S}/\delta_{f,R}$ = 70/40; i_t = 20°; C_μ = 0.062.

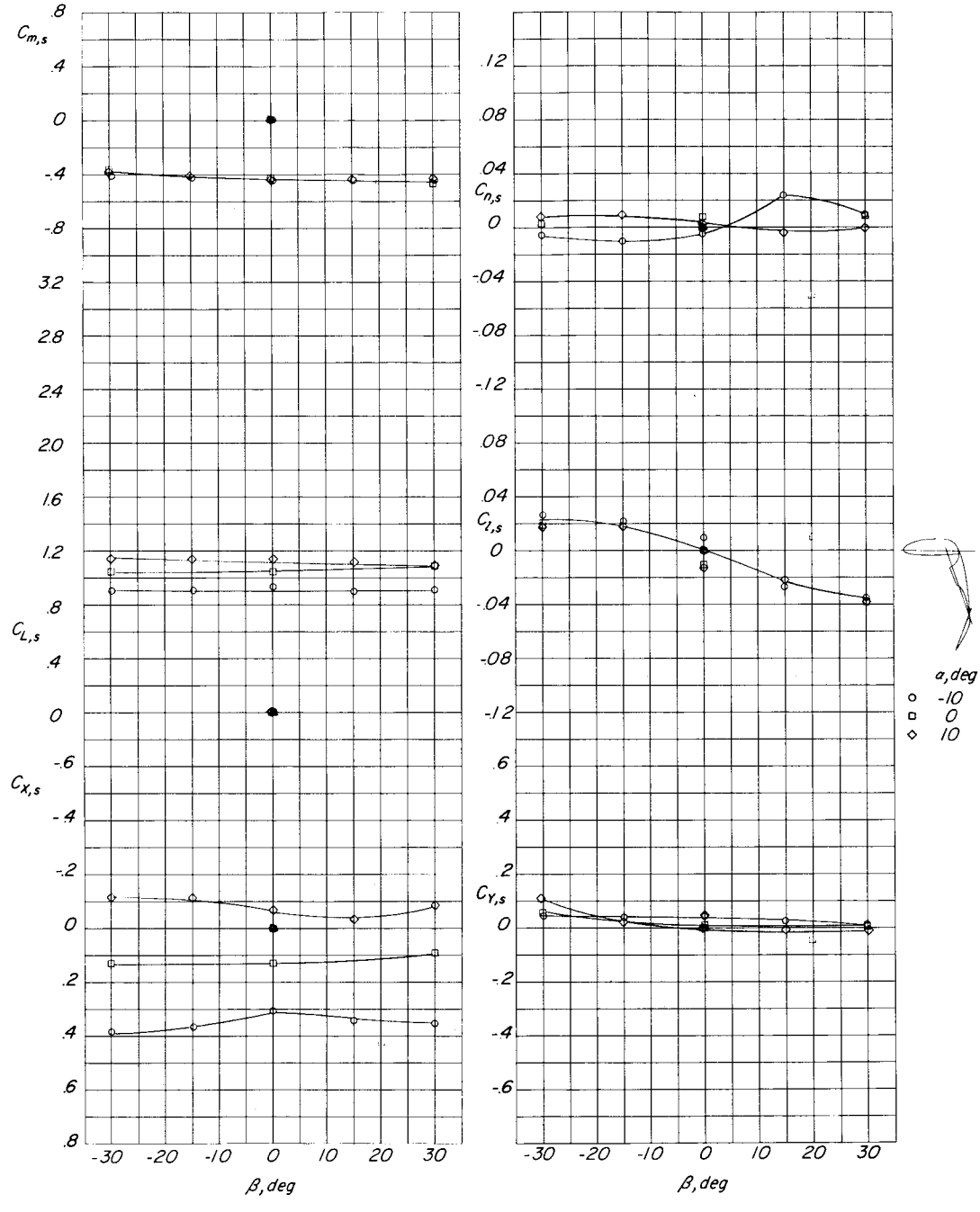

(b) $C_{T,s}$ = 0.980; h/D = 1.56; h'/D = 1.17.

Figure 36.- Continued.

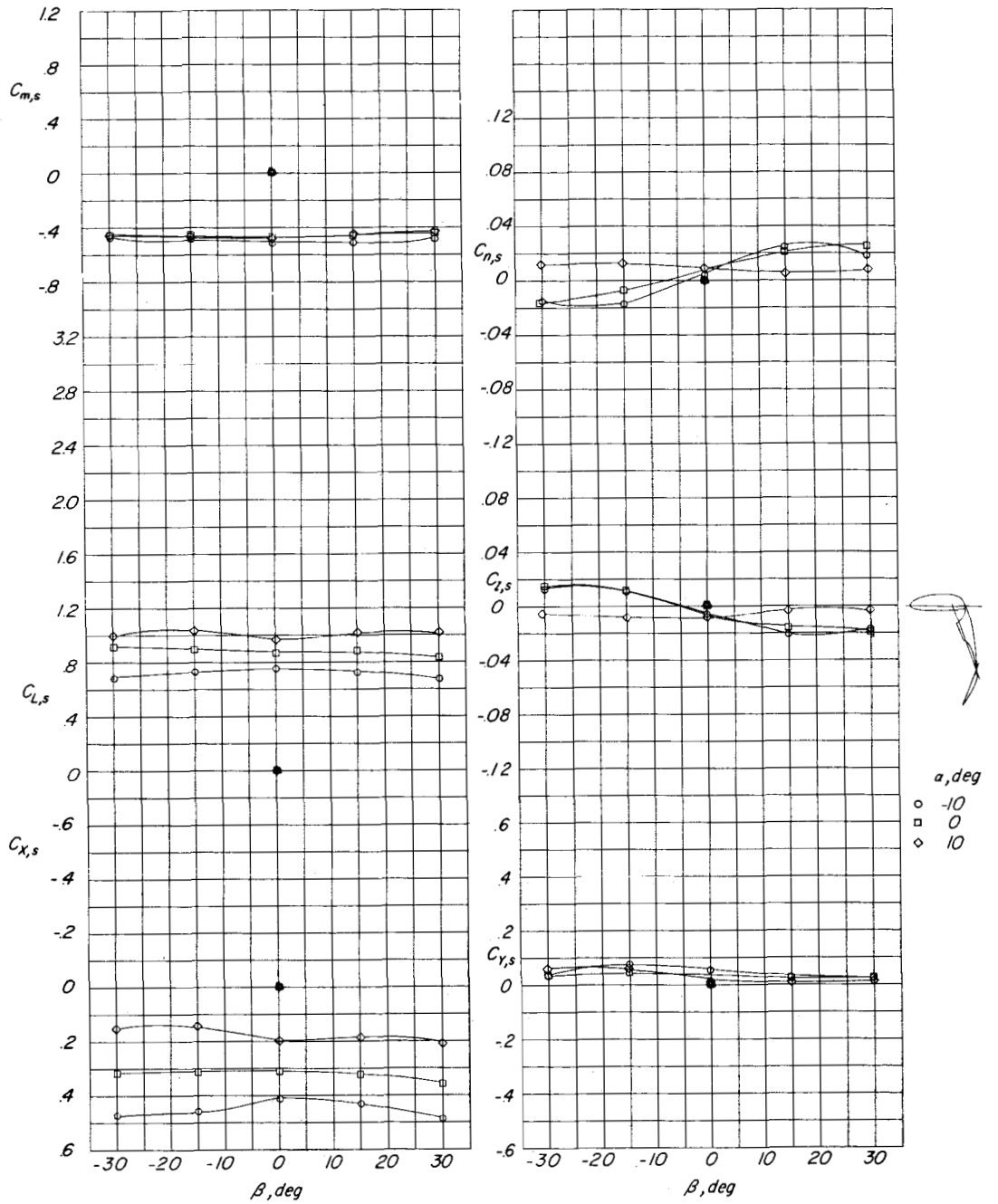

(c) $C_{T,s}$ = 0.980; h/D = 0.94; h'/D = 0.56.

Figure 36.- Continued.

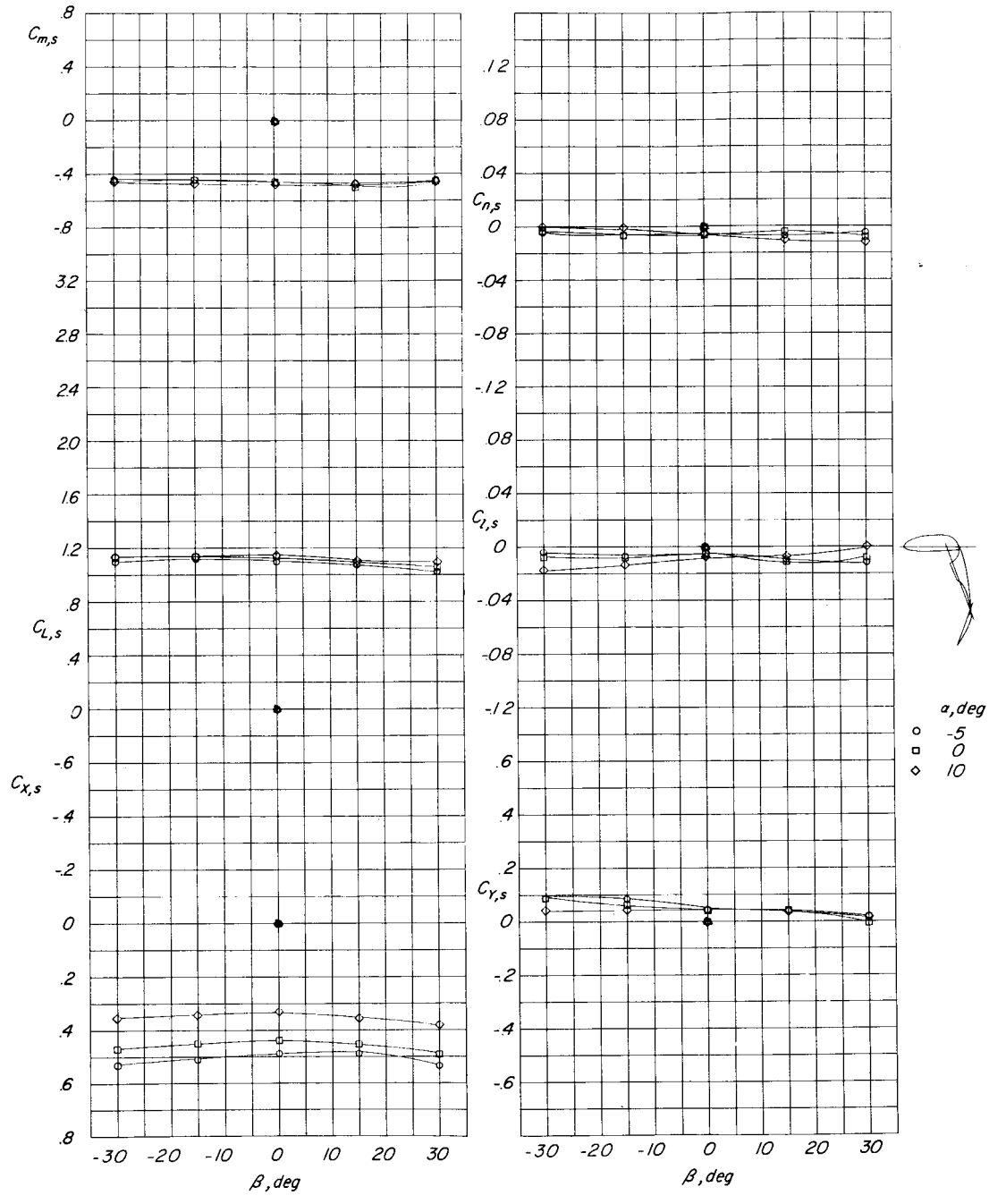

(d) $C_{T,s}$ = 0.960; h/D = 0.56; h'/D = 0.44.

Figure 36.- Concluded.

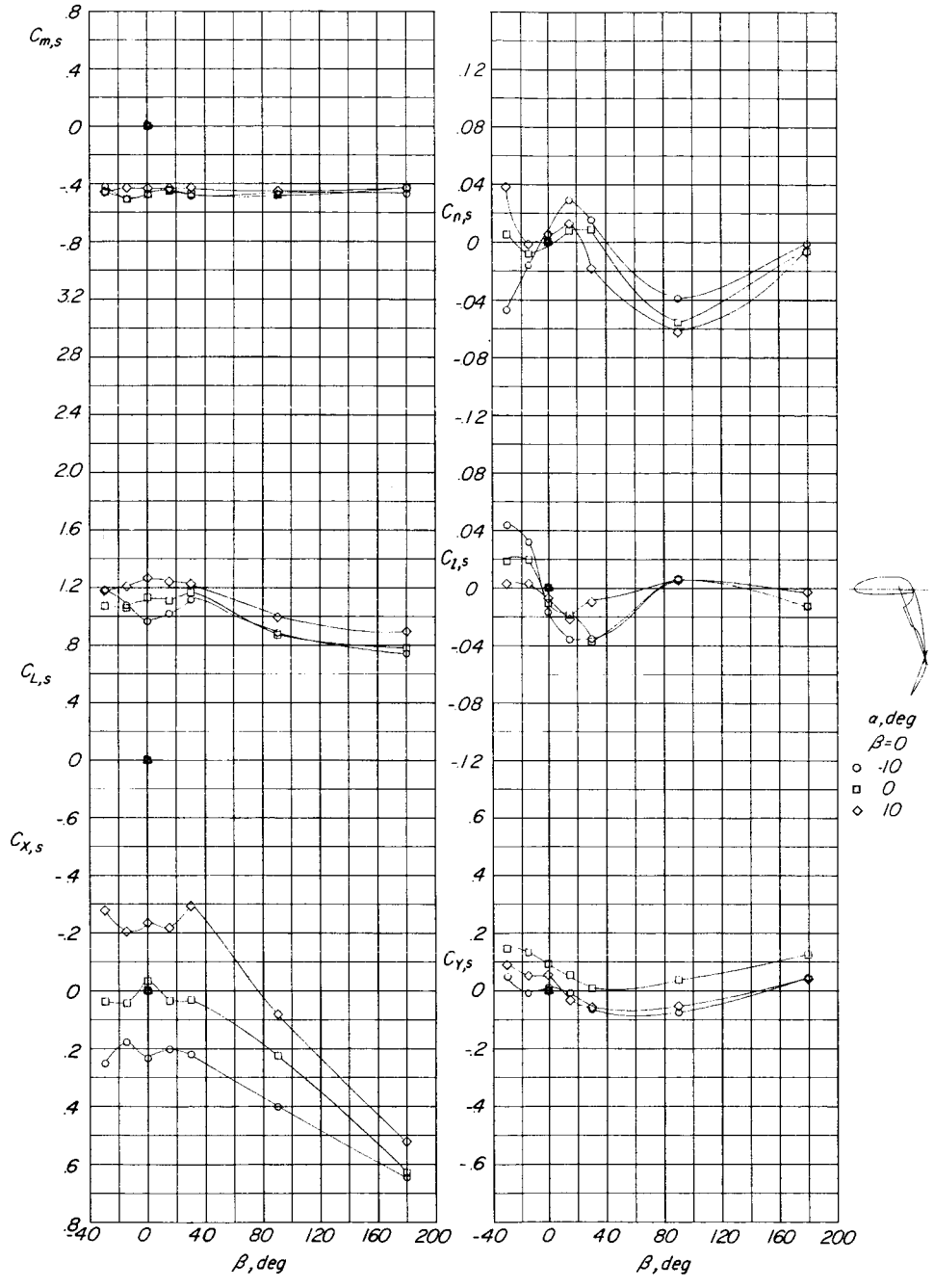

(a) $C_{T,s}$ = 0.980; h/D = 1.94; h'/D = 1.56.

Figure 37.- Effect of rotation of model through a sideslip-angle range of 180°. $\delta_{f,S}/\delta_{f,R}$ = 70/40; i_t = 20°; C_μ = 0.062.

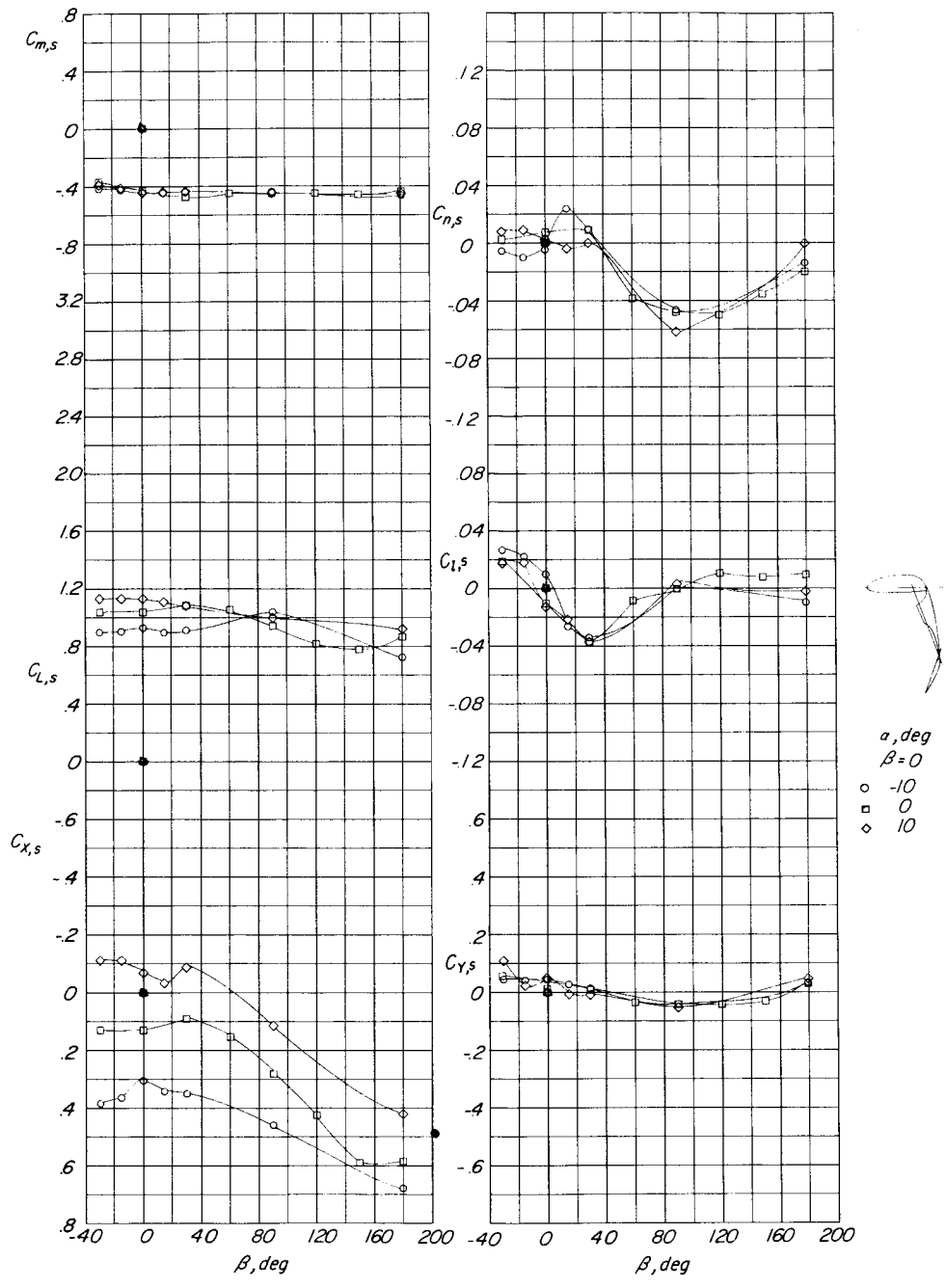

(b) $C_{T,s}$ = 0.980; h/D = 1.56; h'/D = 1.17.

Figure 37.- Continued.

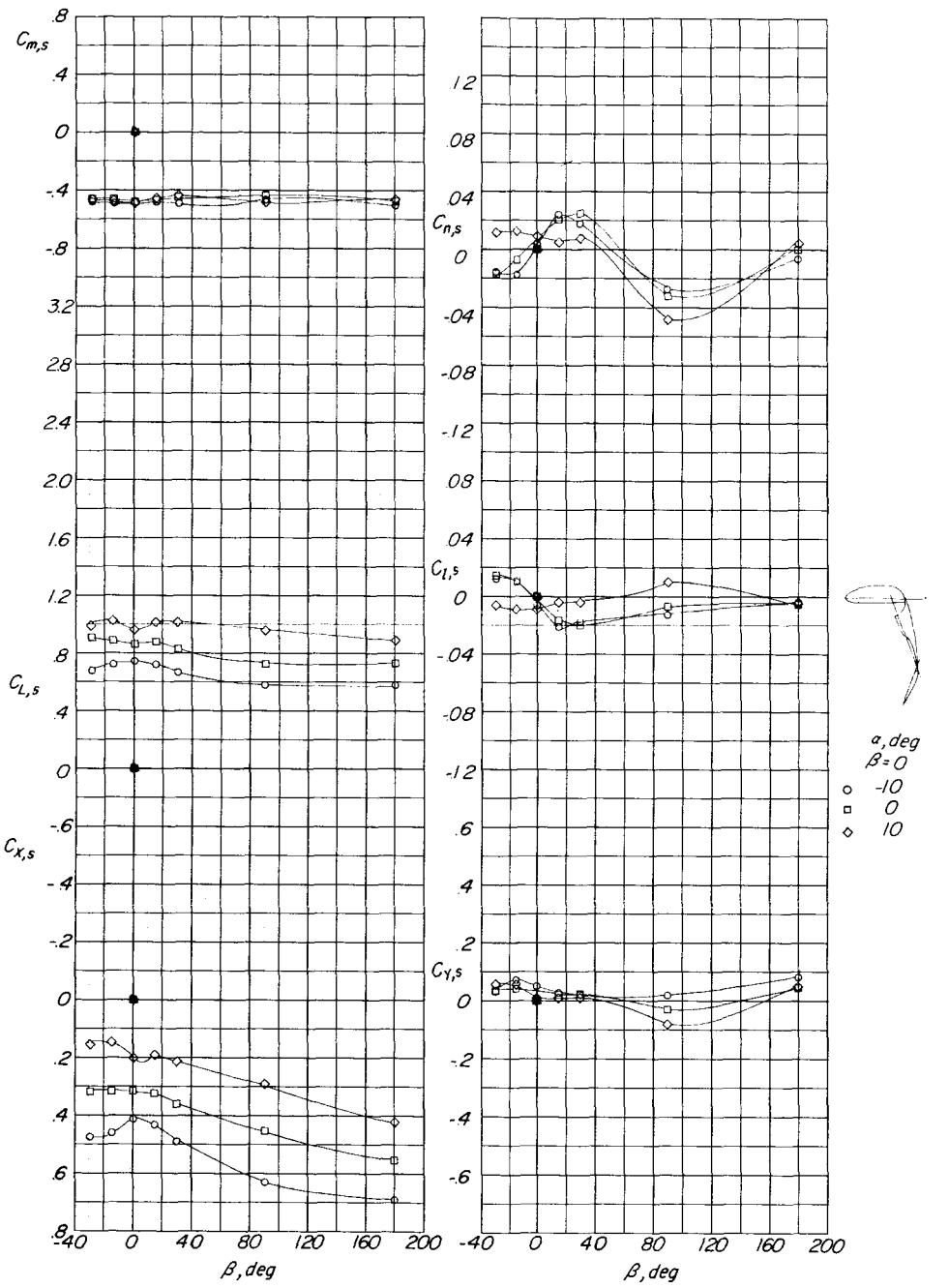

(c) $C_{T,s}$ = 0.980; h/D = 0.94; h'/D = 0.56.

Figure 37.- Continued.

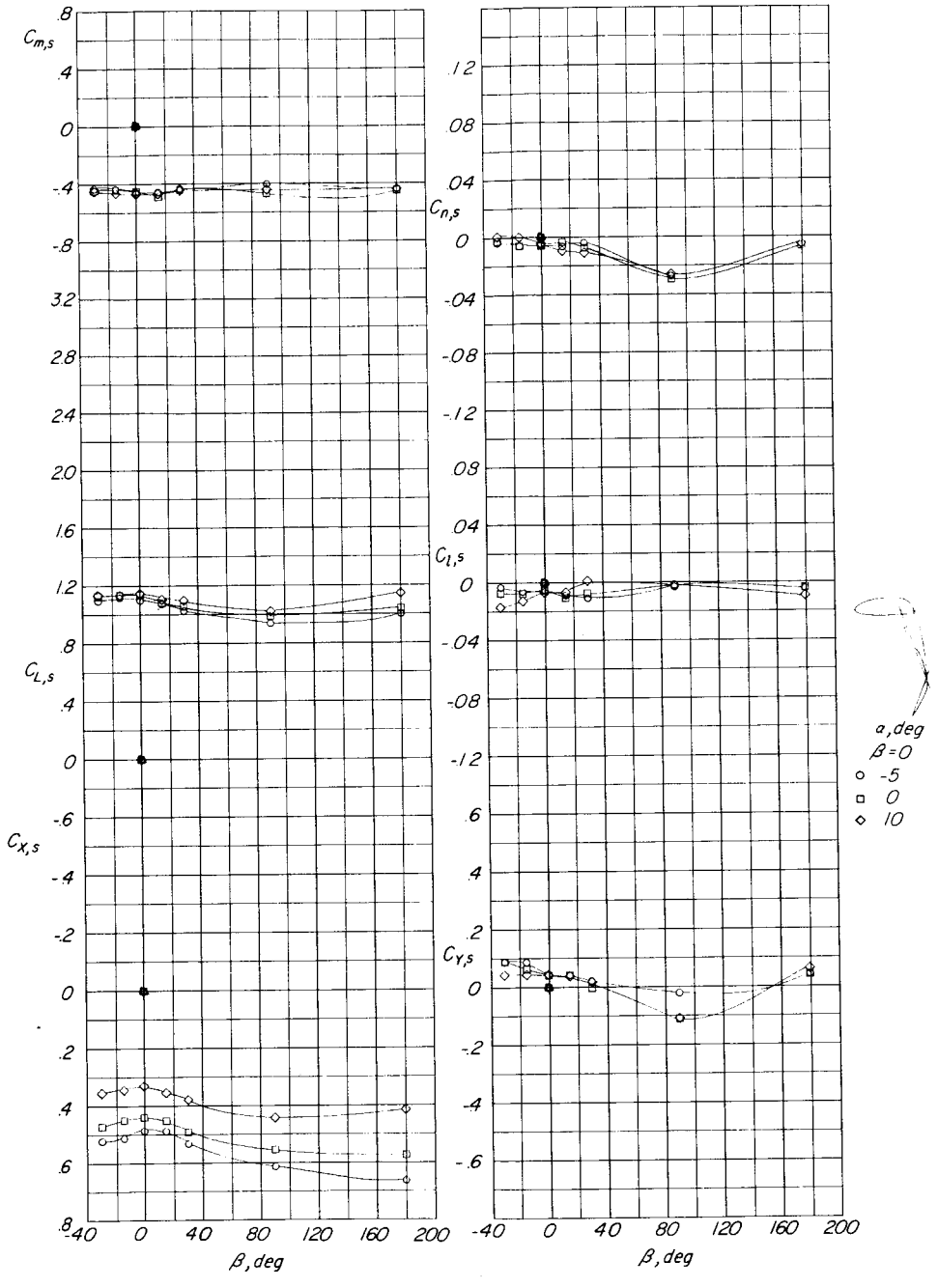

(d) $C_{T,s}$ = 0.960; h/D = 0.56; h'/D = 0.17.

Figure 37.- Concluded.

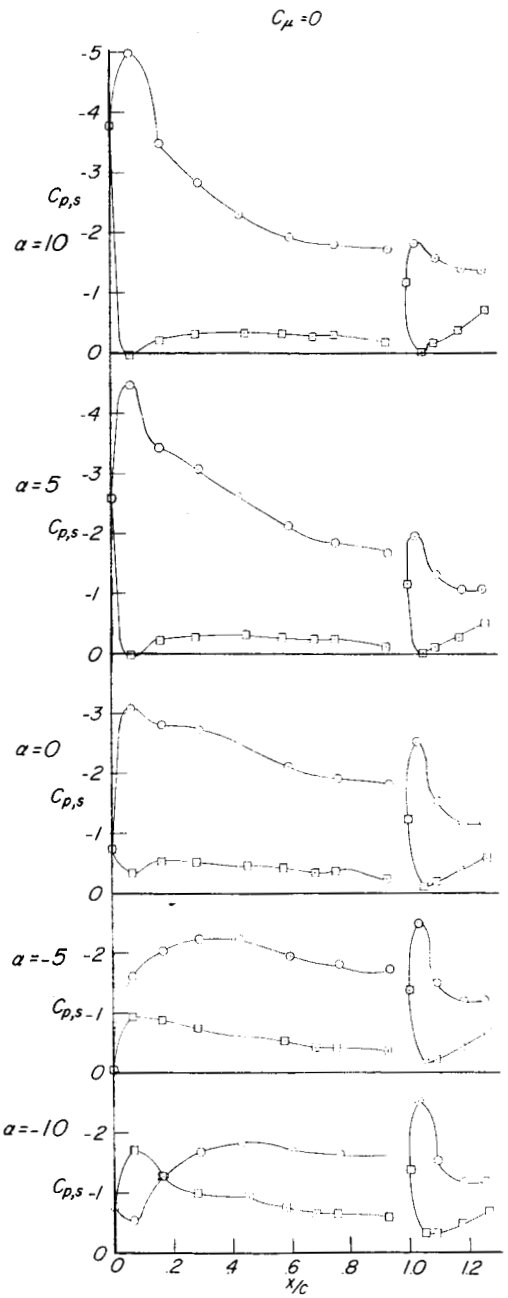

(a) $\delta_{f,S}/\delta_{f,R} = 0/40$; $C_{T,s} = 0$ (propellers off).

Figure 38.- Chordwise wing pressure coefficients taken at a spanwise station on the wing 19.5 inches from fuselage center line.

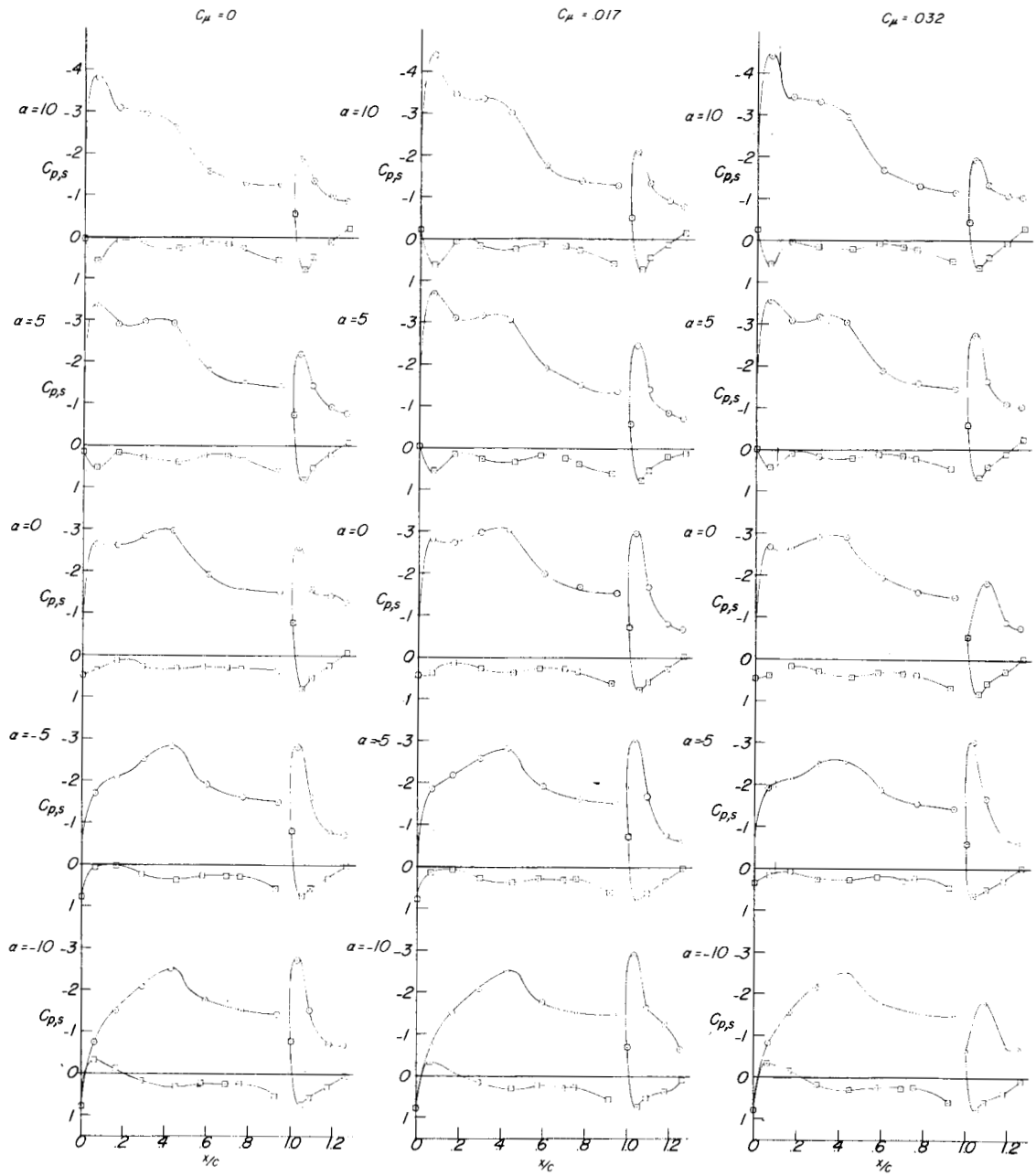

(b) $\delta_{f,S}/\delta_{f,R}$ = 20/40; $C_{T,s}$ = 0.510.

Figure 38.- Continued.

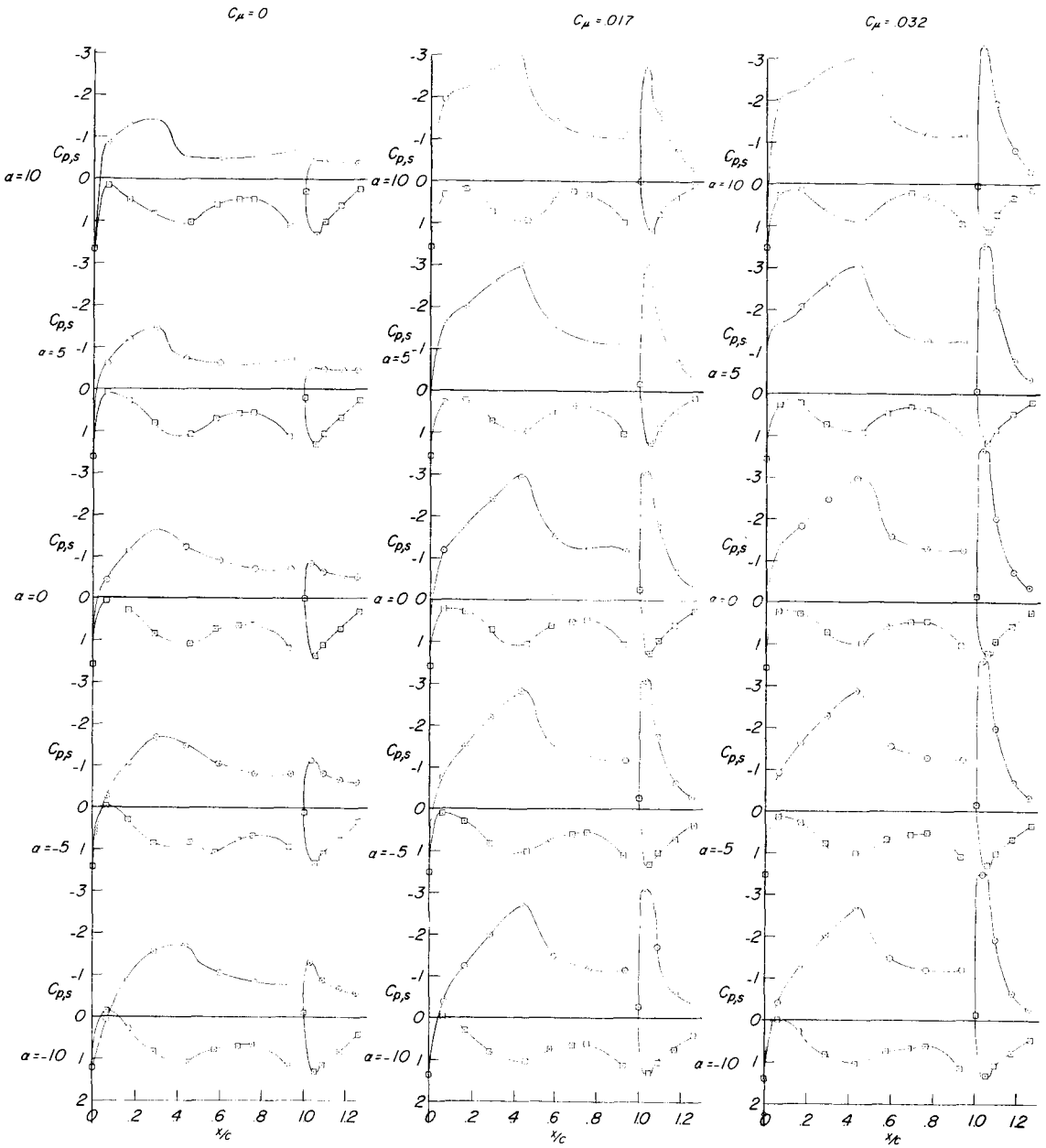

(c) $\delta_{f,S}/\delta_{f,R}$ = 40/40; $C_{T,s}$ = 0.845.

Figure 38.- Continued.

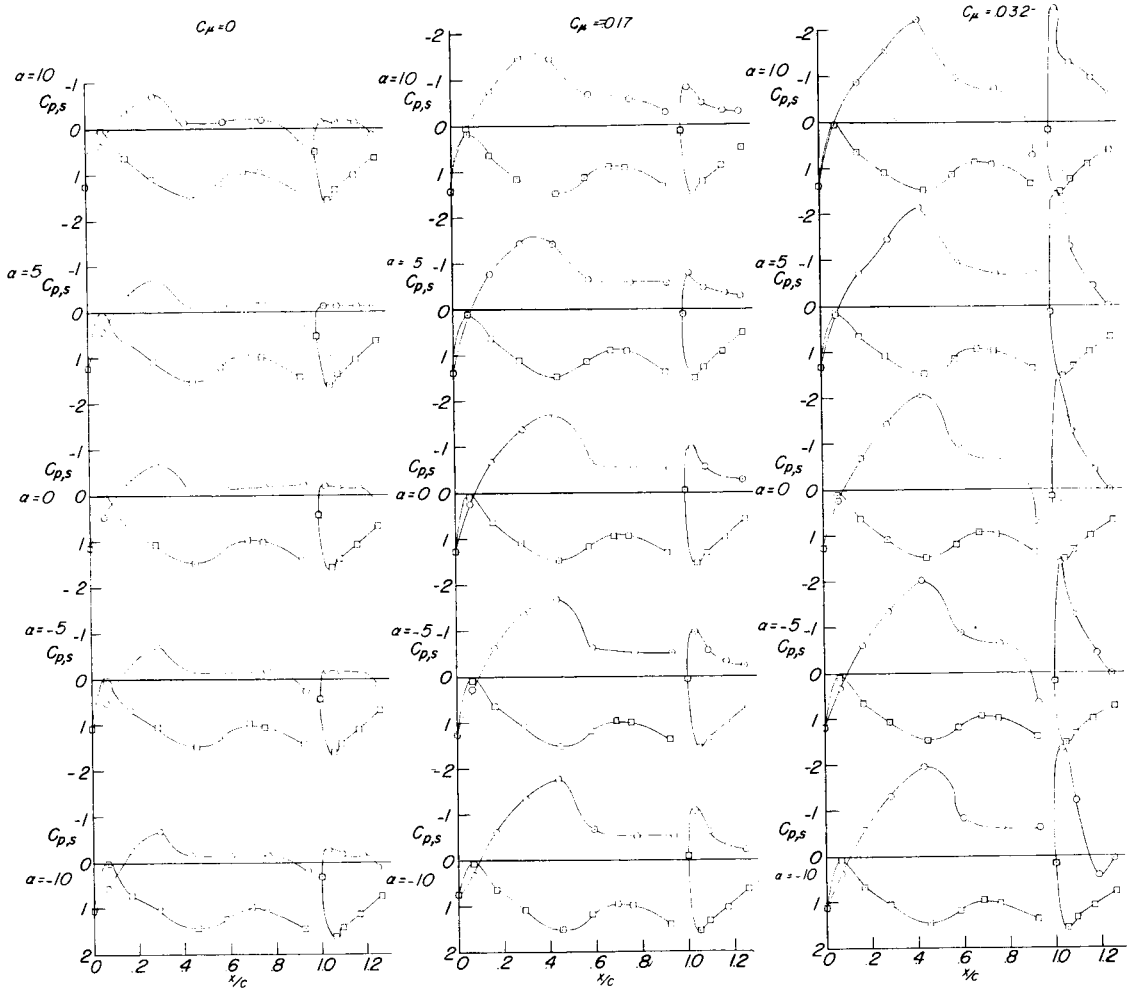

(d) $\delta_{f,S}/\delta_{f,R} = 60/40$; $C_{T,s} = 0.980$.

Figure 38.- Concluded.